


MOLECULAR GEOMETRY, HOMO-LUMO ANALYSIS AND MULLIKEN CHARGE DISTRIBUTION OF 2,6-DICHLORO-4-FLUORO PHENOL USING DFT AND HF METHOD[†]

Surbhi^a, Deeya Shalya^a,  Sarvendra Kumar^{b*}

^aAmity Institute of Applied Sciences, Amity University, Noida, U.P., India

^bSRM Institute of Science and Technology

NCR Campus, Delhi-NCR Campus, Delhi-Meerut Road, Modinagar, Ghaziabad, U.P., India 201204

*Correspondence Author e-mail: sarvendraricky@gmail.com, smalik1@amity.edu

Received September 25, 2022; revised December 25, 2022; accepted January 5, 2023

Phenolic compounds are used in human diet, commonly present in plants. Foremost polyphenolic compounds found in plants are flavanols, flavonoids, flavonones, iso-flavones, phenolic acids, flavonoids, chalcones, lignans etc. These compounds possess antimicrobial, antiviral and anti-inflammatory properties along with high antioxidative activity. The antioxidative activity of phenolic compounds depends on their structure. The polyphenols are very useful for the treatment of inflammation, cancer, anti-ageing purposes in cosmetic formulations, and nutraceutical applications. This article focused on substituted phenol, taking into concern their potential health benefits. The recent rise in machine-learning methods has engendered many advances in the molecular sciences. Using desired level of electronic structure theory from density functional theory, we can calculate the properties (electronic structure, force field, energy) of atomistic systems. The full electron density carries with it a considerable computational cost. While the DFT calculation loses accuracy when the molecule is either extended or compressed, Δ -DFT corrects these errors. Here, molecular point group symmetries are used to obtain chemical accuracy. The optimal 2,6-dichloro-4-fluoro phenol molecular geometry was derived using the 6-311+G (d, p) basis set and DFT/B3LYP (density functional theory) and Hartree-Fock (HF) techniques. A detailed interpretation of Homo-Lumo analysis of 2,6-dichloro-4-fluoro phenol is also listed. Using the 6-311+G (d, p) basis set and the Hartree-Fock (HF) method, the Mulliken charge distribution of this molecule has also been computed.

Keywords: *Homo-Lumo; Mulliken charge; 2,6-dichloro-4-fluoro phenol*

PACS: 31.15.-p, 33.20.Lg, 33.20.Wr, 33.20.Tp, 33.20.Vq, 33.20.Wr, 78.30.-j

INTRODUCTION

An essential method for analyzing the structure of organic molecules is vibrational spectroscopic analysis. The halogen derivatives of phenol find interesting application in agriculture and pharmaceutical field [1-6]. Studying their molecular characteristics and the nature of the reaction mechanism is crucial for understanding specific biochemical mechanisms and in the compound assessment [7,8]. The complete interpretation of spectroscopic studies pointed out that in aromatic compounds, phenol is one of the most important organic molecules in all aspects. Phenol and derivatives of phenol have broadly used as a solvent and synthetic intermediate in computational chemistry. The vibrational spectra of alkyl, halogen substituted phenols have undergone extensive research by numerous researchers [8-12]. To explore the effect of chlorine, bromine, fluorine and methyl substituents in phenol, a detailed vibrational and spectroscopic study seems attractive. So, this study includes the vibrational spectra, Homo-Lumo and Mulliken charge analysis of 2,6-dichloro-4-fluoro phenol.

EXPERIMENTAL DETAILS & COMPUTATIONAL DETAILS

In the present study we adopted density functional theory (DFT) to theoretically predict molecular geometry Homo-Lumo and Mulliken charge distribution. DFT studies have been accepted as a popular approach for molecular computation. All the calculations have been done using the Gaussian 09 program package [13]. First, a semi-empirical approach was used to derive the optimal geometry, and then by applying DFT Becke–Lee–Young–Parr composite of exchange correlation (B3LYP) functional using the 6-311+G (d, p) basis set. Finally, the geometry optimizations were carried out at the same level by using DFT-B3LYP hybrid functional and HF using 6-311+G (d, p) basis set [14, 15]. The vibrational problem was set-up in terms of symmetry and internal coordinates. The calculations have been done using the completely optimized geometry by assuming C₁ point group symmetry. Using the GAUSSVIEW molecular visualization program [16], the values were made with a great degree of confidence along with available related molecules.

RESULT AND DISCUSSION

Molecular Geometry

Fig. 1 depicts the 2,6-dichloro-4-fluoro phenol's optimized molecular structure. The idealized molecular geometry depicts an isolated molecular entity with a point of equilibrium at the potential energy levels; the closure was confirmed by excluding imaginary vibrational wave numbers.

[†] Cite as: Surbhi, D. Shalya, and S. Kumar, East Eur. J. Phys. 1, 205 (2023), <https://doi.org/10.26565/2312-4334-2023-1-27>
© Surbhi, D. Shalya, S. Kumar, 2023

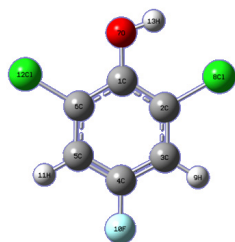


Figure 1 Molecular geometry of 2,6-dichloro-4-fluoro phenol.

The predicted bond lengths and angles, in addition to the geometrical characteristic for the 2,6-dichloro-4-fluoro phenol molecular unit in the solid phase, and the B3LY/6-311+G (d, p) optimized molecular unit are reported in Table 1. The 2,6-dichloro-4-fluoro phenol enhanced structural parameters computed by DFT using the B3LY/6-311+G (d, p) boundary condition are comparable with the atomic number scheme shown in Fig. 1.

There are two C-Cl bond lengths, six C-C bond lengths, one C-F bond length, one O-H bond length, two C-H bond lengths, and one C-O bond length in the title molecule. Table 1 displays the computed values of all bond lengths using Gaussian program in the current assignment.

Based on the estimation, the bond length order is (C3-C4<C4-C5<C2-C3<C5-C6<C1-C2<C1-C6) from the bond length order, it is clear that the benzene ring's hexagonal structure is slightly skewed. The bond angles C2-C1-C6 and C3-C4-C5 deviate from the standard hexagonal angle of 120° by 117.074° and 122.0141°, respectively. This is due to the substitution of Cl, F, and oxygen, group attached to C2, C6, C4, and C1 of the ring. The geometrical parameters evaluated serve as the foundation for the calculation of many other characteristics, including vibratory frequencies as well as other spectroscopic features of the molecule.

Table 1. Optimized geometrical parameters of 2,6-dichloro-4-fluoro phenol by DFT-B3LYP and HF method with 6-311++G(d,p) basis set.

S.No.	Bond length	Value (Å ⁰)		Bond angle	Value(°)	
		DFT	HF		DFT	HF
1	C1-C2	1.401	1.3867	C2-C1-C6	117.074	117.2542
2	C1-C6	1.403	1.392	C2-C1-O7	123.6347	123.8141
3	C1-O7	1.3487	1.3351	C6-C1-O7	119.2913	118.9317
4	C2-C3	1.3887	1.3821	C1-C2-C3	122.6242	122.322
5	C2-Cl8	1.7602	1.7442	C1-C2-Cl8	117.8555	118.8152
6	C3-C4	1.384	1.3706	C3-C2-Cl8	119.5202	118.8628
7	C3-H9	1.0809	1.0721	C2-C3-C4	117.8876	118.2229
8	C4-C5	1.3857	1.3762	C2-C3-H9	121.3628	121.0386
9	C4-F10	1.3489	1.3241	C4-C3-H9	120.7496	120.7386
10	C5-C6	1.3889	1.3782	C3-C4-C5	122.0141	121.7399
11	C5-H11	1.0811	1.0722	C3-C4-F10	119.0016	119.2263
12	C6-Cl12	1.7455	1.7324	C5-C4-F10	118.9843	119.0339
13	O7-H13	0.9666	0.9421	C4-C5-C6	118.826	118.9212
14				C4-C5-H11	120.339	120.3072
15				C6-C5-H11	120.8349	120.7717
16				C1-C6-C5	121.574	121.5399
17				C1-C6-Cl12	118.857	119.2769
18				C5-C6-Cl12	119.5689	119.1832
19				C1-C7-H13	108.8655	111.1338

For numbering of atom refer Fig. 1

Homo-Lumo Energy

The ability to provide electrons is characterized by the HOMO (Highest Occupied Molecular Orbital) energy, the competence to receive electrons is characterized by the LUMO (Least Unoccupied Molecular Orbital), and the gap between HOMO and LUMO specifies the chemical stability of molecules. Because it is a measurement of electron conductivity, the difference in energy between the HOMOs and LUMOs is an important criterion in understanding about features of molecular electric propagation. The energy values of LUMO and HOMO and their energy gap govern a molecule's kinetic stability, chemical responses, spontaneous polarizability, and chemical hardness-softness. [17-19].

The high values of the energy gap indicate the ruggedness, whereas the small value displays the tenderness of the molecular structure. Since they require a significant amount of energy to excite, in comparison to soft molecules, hard molecules are not significantly polarizable [18-20]. A molecule is chemically reactive if it has a minimal or nonexistent HOMO-LUMO gap. The HOMO-LUMO gap illustrates the molecular fragility of the compound [20-21]. Additional quantity that is estimated is the electrophilicity index, which quantifies the energy loss experienced by a ligand as a result of the maximum electron flow between the donor and acceptor [17-18].

The energies of HOMO, LUMO, HOMO-1 (Second Highest Occupied Molecular Orbital), and LUMO-1 (Second Least Unoccupied Molecular Orbital) employ the TD-DFT approach for estimation. by employing the identical boundary conditions, as well as the related energy gap for 2,6-dichloro-4-fluoro phenol are shown in Table 2.

The equations are used to calculate some important properties are as follows (as given in Table 3):

$$\text{Ionization Potential (I)} = -E_{\text{HOMO}}$$

$$\text{Electron Affinity (A)} = -E_{\text{LUMO}}$$

$$\text{Chemical Potential } (\mu) = (E_{\text{LUMO}} + E_{\text{HOMO}})/2$$

$$\text{Global Hardness } (\eta) = (E_{\text{LUMO}} - E_{\text{HOMO}})/2$$

Global Softness (S) = $1/\eta$

Electronegativity (σ) = $-\mu$

Electrophilicity Index (ω) = $\mu^2/2\eta$

These values will be same since the values of E_{HOMO} and E_{LUMO} are same for each basis set as shown in Table 3. Atomic orbital HOMO and LUMO compositions of the frontier molecular orbital for 2,6-dichloro-4-fluoro phenol are shown in Fig. 2 and Fig. 3 respectively.

Table 2. Energy values (eV) of 2,6-dichloro-4-fluoro phenol calculated by using TD-DFT/ B3LYP/6-311+G(d,p)

	HF/6-311+G(d,p)	DFT/6-311+G(d,p)
E_{HOMO}	-0.37157	-0.26498
E_{LUMO}	-0.08646	-0.04094
$E_{\text{HOMO-1}}$	-0.37321	-0.27095
$E_{\text{LUMO-1}}$	-0.11511	-0.02031
ΔE	0.28511	0.22404
∂E	0.2581	0.19064
$\Delta E = E_{\text{LUMO}} - E_{\text{HOMO}}$, $\partial E = E_{\text{LUMO+1}} - E_{\text{HOMO-1}}$		

Table 3. Calculated Ionization potential (I), Chemical potential (μ), Electron affinity (A), Global hardness (η), Global softness (S) in eV^{-1} , Electronegativity (σ) and Electrophilicity index (ω) using DFT and HF with 6-311+G(d,p) basis sets.

Parameters	B3LYP/6-311+G(d,p) Values in (eV)	HF/6-311+G(d,p) Values in (eV)
E_{HOMO}	-0.26498	-0.37157
E_{LUMO}	-0.04094	-0.08646
Ionization Potential (I)	0.26498	0.37157
Electron Affinity (A)	0.04094	0.08646
Chemical Potential (μ)	-0.15296	-0.229015
Global Hardness (η)	0.11202	0.142555
Global Softness (S)	8.92697733	7.01483638
Electronegativity (σ)	0.15296	-0.229015
Electrophilicity Index (ω)	0.10443118	0.183956614



Figure 2. Atomic orbital HOMO compositions for 2,6-dichloro-4-fluoro phenol using (a) DFT/6-311+G(d,p) and (b) HF/ 6-311+G(d,p)



Figure 3. Atomic orbital LUMO compositions for 2,6-dichloro-4-fluoro phenol using (a) DFT/6-311+G(d,p) and (b) HF/ 6-311+G(d,p)

Mulliken Charges

By applying the basis sets HF/6-311+G (d, p) and B3LYP/6-311+G (d, p) in a Mulliken population analysis, Mulliken charges have been approximated [20-30]. Fig. 4 depicts the 2,6-dichloro-4-fluoro phenol mulliken charges. The 2,6-dichloro-4-fluoro phenol atoms' Figure 4 illustrates the positive and negative charge distribution of this article.

Table 5. Mulliken charges of 2,6-dichloro-4-fluoro phenol computed by HF/6-311+G(d,p) and B3LYP/6-311+G(d,p) basis sets

S.No.	Atom	HF/6-311+ G(d,p)	DFT/6-311+ G(d,p)
1	C	0.422709	0.322090
2	C	-0.396267	-0.346824
3	C	-0.212681	-0.177132

S.No.	Atom	HF/6-311+ G(d,p)	DFT/6-311+ G(d,p)
4	C	0.402539	0.311973
5	C	-0.212681	-0.177132
6	C	-0.396267	-0.346824
7	O	-0.669420	-0.559410
8	Cl	0.216720	0.201306
9	H	0.309530	0.242573
10	F	-0.397307	-0.286088
11	H	0.309530	0.242573
12	Cl	0.216720	0.201306
13	H	0.406873	0.371590

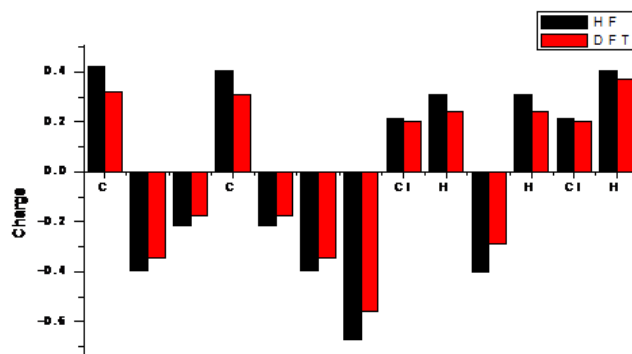


Figure 4. Mulliken charges distribution of 2,6-dichloro-4-fluoro phenol calculated by HF/6-311+G(d,p) and B3LYP/6-31+G(d,p) basis sets.

CONCLUSIONS

The 2,6-dichloro-4-fluoro phenol atom's improved molecular geometry was predicted at the B3LYP level using the 6-311+G (d, p) basis set. As a result, only admissible variations from the research observations were included in the task, which was presented at a higher level with a larger boundary condition. Transmission of charge occurs inside the molecular structure, as evidenced by the computed HOMO and LUMO energies. In order to understand the compound, the 2,6-dichloro-4-fluoro phenol's Mulliken Charge has additionally been measured.

ORCID IDs

 Sarvendra Kumar, <https://orcid.org/0000-0003-2766-3499>

REFERENCES

- [1] R.A. Yadav, P. Rani, M. Kumar, R. Singh, P. Singh, and N.P. Singh, "Experimental IR and Raman spectra & quantum chemical studies of molecular structures, conformers & vibrational characteristics of L-ascorbic acid", *Spectrochimica Acta A*, **84**(1), 6 (2011). <https://doi.org/10.1016/j.saa.2011.07.043>
- [1] V. Krishnakumar et al., "Vibrational and normal coordinate analysis of xanthine and hypoxanthine", *Indian J. of Physics*, **42**(06), 411-418 (2004). <http://nopr.niscares.in/handle/123456789/26125>
- [2] V.K. Rastogi, V. Jain, M.A. Palafox, D.N. Singh, and R.A. Yadav, "The variation of enthalpy function and heat capacity of 2,6,4 DCFP", *Spectrochimica Acta*, **57**(A), 209 (2001). [https://doi.org/10.1016/S1386-1425\(00\)00327-9](https://doi.org/10.1016/S1386-1425(00)00327-9)
- [3] V. Krishnakumar, and V. Balachandran, "FTIR, FT-Raman spectral analysis and normal coordinate calculations of 2-hydroxy-3-methoxy-benzyldehyde-thio-semicarbozone", *Indian J. of Pure and Appl. Physics*, **42**, 313-318 (2004). <http://nopr.niscares.in/bitstream/123456789/9583/1/IJPAP%2042%285%29%20313-318.pdf>
- [4] S. Gunasekaran, and P. Abitha, *Indian J. of Pure and Appl. Physics*, **43**, 329-334 (2005). <http://nopr.niscares.in/bitstream/123456789/8791/1/IJPAP%2043%285%29%20329-334.pdf>
- [5] S. Chaudhary, Ph. D. Thesis, "Spectral investigation and thermodynamic functions of some aromatic molecules", C.C.S Univ. 2001.
- [6] V. Krishnakumar, and R.J. Xavier, "FT-Raman and FT-IR spectral studies of 3-mercapto-1,2,4 triazole", *Indian J. of Pure and Appl. Phys.* **41**, 95-112 (2003). <http://nopr.niscares.in/bitstream/123456789/25035/1/IJPAP%2041%282%29%2095-99.pdf>
- [7] Fu. Aiping, Du. Dongmei, and Z. Zhengyu, "Study of formamide-meyhonal dimer with ab initio and density function theory methods", *Journal of Quantum Chemistry*, **97**, 865-875 (2004). <https://doi.org/10.1002/qua.10796>
- [8] A. Altum, K. Gölcük, and M. Kumru, *Journal of Molecular Structure*, **637**, 155 (2003). [https://doi.org/10.1016/S0166-1280\(03\)00531-1](https://doi.org/10.1016/S0166-1280(03)00531-1)
- [9] V. Krishnakumar, and R. Ramasamy, "Spectral and normal coordinate analysis of 6-methoxy purine", *Indian J. of Pure and App. Physics*, **40**, 252-255 (2002). https://www.researchgate.net/publication/279895257_Spectral_and_normal_coordinate_analysis_of_6-methoxy_purine
- [10] B.S. Yadav et al., "FT-IR spectroscopic studies of 2-hydroxy-4-methyl pyrimidine hydrochloride" *Asian journal of chemistry*, **20**(1), 273-276 (2008). https://asianjournalofchemistry.co.in/user/journal/viewarticle.aspx?ArticleID=20_1_43
- [11] V. Krishnakumar et al., "Normal coordinate analysis of vibrational spectra of 2- methyl iodine and 5-hydroxyinoline", *Indian J. of Pure and Appl. Physics*, **41**, 85-99 (2003). <https://www.semanticscholar.org/paper/Normal-coordinate-analysis-of-vibrational-spectra-Krishnakumar-Xavier/bb1c9858cca12a0d182404e34ec3db17af178eb8>

- [12] R.L. Frost, Y. Xi, S.J. Palmer, G.J. Millar, K. Tan, and R.E. Pogson, "Vibrational spectroscopy of synthetic stecorite $\text{H}(\text{NH}_4)\text{Na}(\text{PO}_4) \cdot 4\text{H}_2\text{O}$ ", *Spectrochimica Acta A*, **84**(1), 269-274 (2011). <https://doi.org/10.1016/j.saa.2011.09.040>
- [13] M. Karabacak, M. Cinar, Z. Unal, and M. Kurt, "Spectroscopic and computational studies on 3-methyl aniline", *Mol. Struct.* **982**, 22-27 (2010). <https://doi.org/10.1016/j.molstruc.2010.07.033>
- [14] V.P. Gupta, and P. Tandon, "Conformational and vibrational studies of isomeric hydrogen cyanide tetramers by quantum chemical methods", *Spectrochimica Acta Part A: Molecular and Biomolecular Spectroscopy*, **89**, 55-66 (2012). <https://doi.org/10.1016/j.saa.2011.12.030>
- [15] M.J. Frisch et al., Gaussian 09 Revision A.02, Gaussian, Inc., Wallingford CT, 2009.
- [16] A. Abhas et al., *Spectrochimica Acta Part A*, **21**, 376-383 (2015). <https://doi.org/10.1016/j.saa.2014.11.024>
- [17] Samuel Tetteh et al, *Electronic Spectra of ortho-Substituted Phenols: An Experimental and DFT Study*", *Hindawi Journal of Spectroscopy*, **1**, 1-10 (2018). <https://doi.org/10.1155/2018/4193657>
- [18] F.A. Pasha, H.K. Srivastava, Y. Beg, and P.P. Singh, "DFT Based Electrophilicity Index and QSAR study of Phenols as Anti Leukaemia Agent", *American Journal of Immunology*, **2**(1), 23-28 (2006). <https://thescpub.com/pdf/ajisp.2006.23.28.pdf>
- [19] M. Bogojeski, L. Vogt-Maranto, M.E. Tuckerman, K.-R. Müller, and K. Burke, "Quantum chemical accuracy from density functional approximations via machine learning", *Nature Communication*, **11**, 5223 (2020). <https://doi.org/10.1038/s41467-020-19093-1>
- [20] J. Teotia et al., "Ultraviolet Absorption Spectra, Solvent Effect and Non-Linear Optical Properties of 2-Amino-4,6 dimethylpyridine by Hartee-Fock and Density Functional Theory", *Asian Journal of Chemistry*, **28**(10), 2204-2210 (2016). <https://doi.org/10.14233/ajchem.2016.19928>
- [21] S. Kumar, R. Kumar, J. Teotia, and M.K. Yadav, "Experimental & theoretical (ab initio & DFT) analysis of UV-Vis spectra, thermodynamic functions & nonlinear optical properties of 2-chloro-3,4-dimethylbenzyl dehyde", *Journal of Advances in Physics*, **8**(2), 2122-2134 (2015). https://rajpub.com/index.php/jap/article/view/1519/pdf_158
- [22] S. Kumar, Surbhi, and M.K. Yadav, "Optimized Molecular Geometries, Internal Coordinates, Vibrational Analysis, Thermodynamic properties, First Hyper Polarizability and Homo-Lumo Analysis of Duroquinone using Density Functional Theory and Hartree-Fock Method.", *Russian Journal of Physical Chemistry B*, **15**, S22-S31 (2021). <https://doi.org/10.1134/S1990793121090116>
- [23] H. Kumar, N. Choudhary, Varsha, N. Kumar, Suman, and R. Seth, "Phenolic compounds and their health benefits: A review", *Journal of Food Research and Technology* April-June, **2**(2), 46-59 (2014). https://www.researchgate.net/profile/Harish-Kumar-96/publication/350966390_Phenolic_compounds_and_their_health_benefits_A_review/links/607d535b8ea909241e0cf38c/Phenolic-compounds-and-their-health-benefits-A-review.pdf
- [24] X. Xiang, Z.-X. Zhao, and H.-X. Zhang, "A theoretical study based on DFT calculations on the different influence of functional groups on the C-H activation process via Pd-catalysed β -X elimination", *Royal Society of Chemistry*, **12**, 26116-26122 (2022). <https://doi.org/10.1039/D2RA03506E>
- [25] S. Bhandari, R. Khatun, T.S. Khan, D. Khurana, M.K. Poddar, A. Shukla, V.V.D.N. Prasada, and R. Bal, "Preparation of a nanostructured iron chromite spinel in the pure form and its catalytic activity for the selective oxidation of benzene to phenol: experimental and DFT studies", *Journal of Green Chemistry*, **24**, 9303-9314 (2022). <https://doi.org/10.1039/D2GC02335K>
- [26] F. Maldonado, L. Villamagua, and R. Rivera "DFT Analysis of the Adsorption of Phenol on the Nonpolar (10 $\bar{1}$ 0) ZnO Surface", *J. Phys. Chem. C*, **123**(19), 12296-12304 (2019). <https://doi.org/10.1021/acs.jpcc.9b01906>
- [27] Sarvendra et al., "Vibrational spectroscopic investigation, first hyper polarizability & Homo Lumo analysis of tetrahydroxy-1,4 quinone hydrate using DFT and HF methods", *Russian J. of Physical Chemistry B*, **12**(3), 383-393 (2018).
- [28] Seema et al., "Ultraviolet absorption spectra, solvent effect and Non-linear Optical properties of 1,2,4,5-tetrachloro-3-nitrobenzene by hartee-fock density functional theory" *International journal of research and analytical reviews*, **6**(2), 2241-2248 (2019). http://ijrar.org/viewfull.php?&p_id=IJRAR19K3768
- [29] S. Kumar, Surbhi, and M.K. Yadav, S. Kumar, Surbhi, and M.K. Yadav, "Ultraviolet Absorption spectra, solvent effect and non-linear optical properties of tetrahydroxy-1-4 quinone hydrate by HF and DFT theory", *Asian Journal of Chemistry*, **29**(10), 2241-2248 (2017). <https://doi.org/10.14233/ajchem.2017.20741>

МОЛЕКУЛЯРНА ГЕОМЕТРІЯ, НОМО-ЛУМО АНАЛІЗ ТА РОЗПОДІЛ ЗАРЯДУ МАЛЛІКЕНА 2,6-ДИХЛОР-4-ФТОРФЕНОЛА ЗА ДОПОМОГОЮ DFT ТА HF МЕТОДІВ

Сурбхі^а, Дія Шаля^а, Сарвендра Кумар^б

^аІнститут прикладних наук Аміті, Університет Аміті, Нойда, штат Уттар-Прадеш, Індія

^бІнститут науки і технологій SRM,

Кампус NCR, Кампус Делі-NCR, Делі-Меєрут-роуд, Модінагар, Газіабад, Уттар-Прадеш, Індія 201204

Фенольні сполуки використовуються в раціоні людини, зазвичай присутні в рослинах. Основними поліфенольними сполуками, які містяться в рослинах, є флаванолі, флавоноїди, флавонони, ізофлавонони, фенольні кислоти, флавоноїди, халкони, лігнани тощо. Ці сполуки мають антимікробні, протівірусні та протизапальні властивості разом із високою антиоксидантною активністю. Антиоксидантна активність фенольних сполук залежить від їх структури. Поліфеноли дуже корисні для лікування запалень, раку, для запобігання старінню в косметичних рецептах і нутрицевтиках. Ця стаття присвячена заміненню фенолам, враховуючи їх потенційну користь для здоров'я. Недавній розвиток методів машинного навчання породив багато досягнень у молекулярних науках. Використовуючи бажаний рівень теорії електронної структури з теорії функціоналу густини, ми можемо розрахувати властивості (електронну структуру, силове поле, енергію) атомістичних систем. Повна електронна густина несе з собою значні обчислювальні витрати. Хоча розрахунок DFT втрачає точність, коли молекула розтягується або стискається, Δ -DFT виправляє ці помилки. Симетрії груп молекулярних точок використовуються для отримання хімічної точності. Оптимальну молекулярну геометрію 2,6-дихлор-4-фторфенолу було отримано за допомогою базового набору 6-311+G (d, p) і методів DFT/B3LYP (теорія функціоналу густини) і Хартрі-Фока (HF). Також наведено детальну інтерпретацію аналізу Номо-Лумо 2,6-дихлор-4-фторфенолу. За допомогою базисного набору 6-311+G (d, p) і методу Хартрі-Фока (HF) було також обчислено розподіл заряду Маллікена цієї молекули.

Ключові слова: гомо-лумо; заряд Маллікена; 2,6-дихлор-4-фторфенол

SEMI-EMPIRICAL INVESTIGATION OF ELECTRONIC, VIBRATIONAL AND THERMODYNAMIC PROPERTIES OF PERYLENE MOLECULE (C₂₀H₁₂)[†]

Abdul Hakim Sh. Mohammed^a, Issa Z Hassan^a, Hassan A. Kadhem^b,
Rosure Borhanalden Abdulrahman^{c*}

^aDepartment of Physics, college of Education for pure sciences, University of Kirkuk, Kirkuk, Iraq

^bMinistry of Education, Open Educational College, Kirkuk Center, Iraq

^cDepartment of Physics, College of Science, University of Kirkuk, Kirkuk, Iraq

*Corresponding Author: rabdulrahman@uokirkuk.edu.iq

Received December 20, 2022; revised January 29, 2023; accepted January 30, 2023

This work investigates computationally the spectroscopic and thermodynamics properties of the perylene molecule (C₂₀H₁₂) in the gas phase by utilizing a semi-empirical method [Hyper Chem8.0 and WinMopac7.0] programs, via (MNDO-PM3). This method is providing more simplicity and quick performance. The electronic properties such as total energy, dissociation energy, molecular orbital, ionization potentials, electronic affinity, and energy gap were calculated. However, vibration analysis and UV-visible spectra have been calculated. Moreover, the thermodynamic properties at the standard temperature such as heat of formation, entropy, enthalpy, heat capacity, and Gibbs free energy were calculated.

Keywords: Perylene; C₂₀H₁₂; Energy of molecule; UV-visible; IR; MNDO-PM3; Thermodynamic

PACS: 33.15.Ry, 33.15.-e, 31.10.+z, 65.40.gd, 65.40.Ba, 05.70.Ce, 05.70.Ce, 33.15.Dj, 33.20.Kf

INTRODUCTION

In the last few years, there has been an important effort in the preparation of new organic semiconductors for their application in electronics and optoelectronic devices. Specifically, the development of novel organic semiconductors with effective charge transport capability is an attractive topic in the field of organic electronics for many applications such as organic thin-film transistors (OTFT) and organic light-emitting diodes (OLED) [1–4]. Current and future applications of organic semiconductors range from commercially available OLED displays [5], and infrared applications [6–7], over potentially printable organic [8] and hybrid organic/inorganic solar cells [9], to printable electronic circuits based on organic field-effect transistors (OFET) [10]. While OLED displays outperform their inorganic counterparts in terms of energy efficiency [11]. Compared to inorganic materials, the use of organic semiconductors are attractive because these materials offer many advantages, for example, low cost and the ability to form thin films, which enable the fabrication of large-area and flexible devices. Organic semiconductors include both small molecules and polymers, small molecules have advantages such as easier synthetic procedures, purification methods, and characterization in view of their small size and well-defined structure [12]. In addition, their optical and electronic properties can be easily tuned by means of molecular design. Nature has conserved an infinite variety of organic chemicals, and these materials have much better ranges for ease of making, shaping, and adjusting the properties of materials compared to inorganic chemicals [13]. π - π stacking of organic chemicals reveals good conductivity of charge carriers [13–14]. Regarding the optical performance, the nano/sub-micron organic structures showed a quantum yield close to that of photoluminescence [15]. Subsequently, organic single crystals with excellent optical and electrical properties are critical for the development of organic optoelectronics [16].

Perylene is a brown solid that is a multi-cyclic aromatic hydrocarbon with the chemical formula C₂₀H₁₂. It exhibits blue fluorescence and is utilized as a pure or substituted blue-emitting dopant material in OLEDs. Perylene is also utilized as an organic photoconductor and has been used as technical dyes for many years attributed to its high temperature, photo, and chemical constancy [17]. Besides that, in the last years, such compounds gained large widespread because of their use in optical devices [18–19]. These π conjugated dyes show high photosensitivity and high electron mobility [20–21]. As well as photo physical properties, particularly the sensitivity of their fluorescence lifetime to the PH, render them very useful as probes for live-cell fluorescence lifetime imaging [22]. Perylene dyes are a representative framework of electron transport (n-type) organic semiconductors. The energy of their electron transport level is the electron affinity (EA), which is an important parameter in selecting the electron transport materials for device application and the material's electron-accepting ability [23].

The research employed semi-empirical programs that had fast computational cycles. One of these semi-empirical methods is the MNDO-PM3 approach, which calculates the experimentally measured practical values. This program has adopted one of the molecular modeling methods (HyperChem8.0), and by means of the molecules are drawn in a preliminary way, while fixing the nature of the bonds between two atoms of the molecule. Additionally, the spatial geometry of the molecule is calculated to the nearest energy –stable geometric shape by conducting the process of

[†] Cite as: A.H.Sh. Mohammed, I.Z. Hassan, H.A. Kadhem, and R.B. Abdulrahman, East Eur. J. Phys. 1, 210 (2023), <https://doi.org/10.26565/2312-4334-2023-1-28>

© A.H.S. Mohammed, I.Z. Hassan, H.A. Kadhem, R.B. Abdulrahman, 2023

reducing energy to the optimum limit (Geometry optimization). The potential energy curve is drawn by changing the length of the bond between the two atoms and keeping the total energy at each change as low as possible. Quasi-experimental methodologies are based on the electronic Schrödinger equation gained after detach the nuclear and electronic motion, (Born-Oppenheimer approximation)

$$\hat{H}(r, R) \Psi(r, R) = E(r, R) \Psi(r, R). \quad (1)$$

Here r and R indicate the coordinates of the electrons and the nucleus respectively [24].

This study's aim is to investigate Perylene's ($C_{20}H_{12}$) vibration spectrum and electronic structure in the IR region and electronic transition in the UV-visible region, using semi-empirical calculations (MNDO-PM3). It has a planar structure with D_{2h} point symmetry. The research purpose to calculate the lower energy of the stabilized state of the molecule way potential energy curves. One important characteristics that have been studied are for the thermodynamic principles which is concerned with the energy transformation of the substance in the empty space that the substance occupies (system) and the subsequent shift in its energy level the internal energy is a type of potential energy in the system which plays a role in many concepts, including heat capacity its unit $\text{cal.mol}^{-1}.\text{deg}^{-1}$ [25], All materials have an enthalpy that depends on pressure, temperature, and internal energy, with the exception of gases, which behave ideally or almost ideally [26]. The distinctive characteristic that relates to the stability of the compound is either the heat of formation or the enthalpy of formation; if it is positive, the compound is unstable, and if it is negative the compound is stable. Entropy (S), which it is a measure of the resulting randomness of a compound due to the change in temperature degrees, is another function [27]. Additionally, free Gibbs energies were calculated using the [HyperChem8.0 and WinMopac7.0] software.

COMPUTATION METHODS

Semi-empirical calculation investigations were carried out using MNDO-PM3 in order to understand the geometrical optimization and electron structures of perylene in the neutral and singlet states. Computation the electronic properties like the ionization energy of electronic states, and energy gap (E_g), geometric optimization of Perylene in the gas phase by the semi-empirical way, and calculated the highest occupied molecular orbital in electron (HOMO) and lowest unoccupied molecular orbital in electron (LUMO). In addition, computation of the IR spectrum in the ground state, ionization potential (IP) and electronic affinity (EA) by using the following equations [28],

$$IP = |E_{\text{HOMO}}| \quad ; \quad EA = |E_{\text{LUMO}}| \quad (2)$$

Also, the electronegativity (χ) has been computed by using the equation [29],

$$\chi = (IP + EA) / 2 \quad (3)$$

While the hardness (η) is defined [29],

$$\eta = (IP - EA) / 2 \quad (4)$$

Whereas the softness (S) and electrophilic (W) is defined by equations [30],

$$S = 1 / 2 \eta \quad (5)$$

$$W = \chi^2 / 2\eta \quad (6)$$

Several thermodynamic properties of the perylene molecule have been investigated using computer programs (WinMopac 7.0). These properties determine the most important conditions for conducting reactions as well as the effect of temperatures on a molecule within the three phases and for a variety of temperatures that include melting, boiling, and standard degrees, as well as comparing the results with experimental values taken from the literature.

RESULTS AND DISCUSSION

Molecular Structure

The geometric shape of the perylene molecule ($C_{20}H_{12}$) was drawn through a program HyperChem8.0 that relies on calculating the internal coordinate (r, θ, ϕ) and on the geometric form at the equilibrium case of the perylene as in Figure 1.

After getting the matrix and inserting it into the program WinMopac 7.0, some important properties of the perylene molecule were determined, such as the final heat of formation, the total energy at the stability posture, the binding energy, the electronic energy, the core-core interaction, the zero-point energy, the ionization potential, and the electronic affinity, as shown in Table 1.

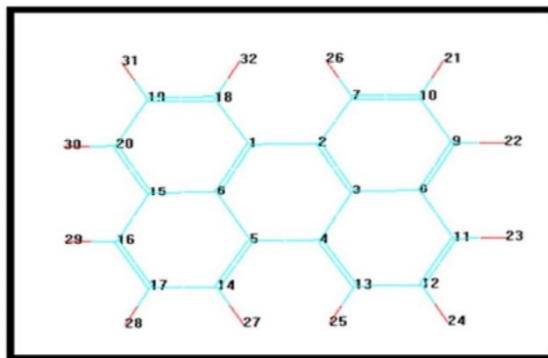


Figure 1. shows the molecular structure of the perylene molecule that was drawn in the program HyperChe8.0.

Table 1. show the result of some important properties of the perylene molecule was calculated, by using (HyperChem8.0 and WinMopac7.0)

Quantum	Magnitude Cal. [HyperChem8.0]	Magnitude Cal. [WinMopac 7.0]	Unit
Total Energy	-58880.6822330	-58879.1031898	/mol kcal
Total Energy	- 93.832328265		a.u.
Binding Energy	- 3961.4641970		kcal/mol
Isolated atomic energy	- 54919.2180360		kcal/mol
Electronic Energy	- 429071.4512403	-429045.60781474	kcal / mol
Core-Core Interaction	370190.7690073	370166.5046249	kcal / mol
Heat of Formation	81.5598030	82.019799	kcal/mol
Gradient	0.1844568	1.65705	mol/ang kcal/
Molecular point group	D _{2h}		
Zero point energy of vibration	160.43560	160.886	kcal/mol
Ionization Potential	7.984057	7.98706	eV
Electronic Affinity	7.984		eV

The Un-Harmonic Potential Energy Calculation (Perylene)

Studying the potential curve, which represents the correlation between the total energy of the molecule and the interatomic distance of the active bonds in the perylene molecule, permitted to determine the lowest energy value of the curve, which represents the equilibrium point (the bottom of the curve). At the distance of ($r_e=1.1\text{Å}$), it has a value of (-3961.55) kcal/mol for (C10-H21) and (-3962.5510) kcal/mol for (C17-H28).

The potential curve depicted the force between the atoms (C10-H21) and (C17-H28) for perylene, and these forces illustrate the total of the forces of repulsion and attraction. When the distance between the atoms is reduced, the force of attraction from the other nucleus begins to effect each electron. At the same time, electrons and nuclei begin to repel each other [31]. When the atoms are separated from each other by increasing the distance, the gravitational force will present that the total energy decreases due to the decrease in the potential energy and the electronic-nucleus attraction, thus; increasing the energy reduction until it reaches the lowest total energy value. The dissociation energy of the molecule is calculated from the difference between its lowest energy value and its value when r is infinity. Furthermore, when the distance between two atoms is infinite, the potential energy becomes zero [31], and the value of dissociation energy is as follows: (C10-H21) ($D_e = 182.44$ kcal/mol.) as shown in Figure 2, and (C17-H28) ($D_e = 209.08$ kcal/mol.) illustrated in Figure 3.

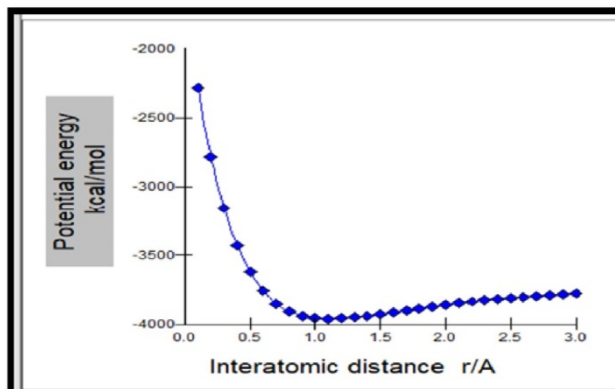


Figure 2. Potential energy change with interatomic distance (C10-H21) of perylene molecule.

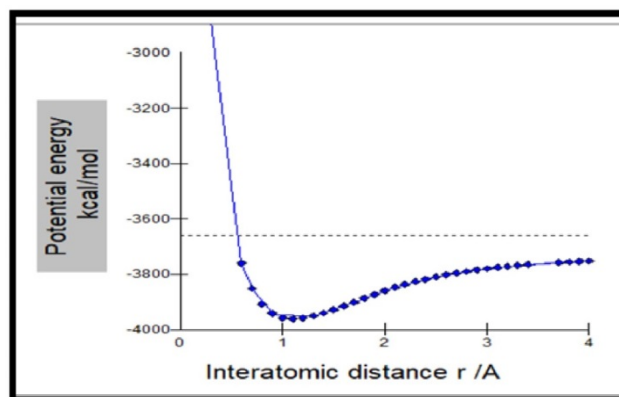


Figure 3. potential energy change with interatomic distance (C17-H28) of perylene molecule.

Calculation the Vibrational Frequencies of the Perylene Molecule

After drawing the potential energy curve of the molecule at the equilibrium position, the modes of vibration frequencies of the molecule were calculated from this point, which was 90 modes according to $(3N-9)$ and by using (HyperChem 8.0 and WinMopac 7.0) expressed in wavenumber and unit cm^{-1} . The results showed that the calculated values were close to practical and theoretical values in the literature, as shown in Table 2.

Table 2. vibrational frequencies of perylene calculated by using (HyperChem8.0 and WinMopac7.0) programs and Comparison with practical values and other works.

Vibe. modes	Symmetry	Intensity	Wave number 1/cm Cal. [HyperChem]	Wavenumber 1/cm Cal. [WinMopac]	Cal. cm^{-1}	Exp. Cm^{-1}	Cal. cm^{-1}
					[32]	[33]	
1	1 AU	0.00006	49.04	49.425			
2	1 B3U	0.23811	90.03	91.21			87
3	1 B2G	0	150.68	151.32			126
4	2 B3U	2.54259	166.98	167.51			172
5	1 B1G	0	181.7	182.2			188
6	2 AU	0	230.8	231.36			255
7	2 B2G	0	286.72	287.01			
8	1 B2U	0.01594	287.56	287.76			294
9	1 B3G	0	368.67	368.71			368
10	1 AG	0	381.64	381.67			
11	2 B1G	0	385.77	386.22			403
12	3 B3U	0.09547	428.46	428.76			
13	3 B2G	0.00001	436.79	436.98			441
14	2 AG	0	462.17	462.47			445
15	3 AU	0.00001	480.37	480.56			482
16	1 B1U	0.13799	486.95	487.11			
17	4 B3U	4.4721	538.12	538.4			534
18	2 B2U	0.16382	545.65	545.67			546
19	3 B1G	0	559.21	559.48			
20	2 B3G	0	562.44	562.52			
21	2 B1U	0.39825	592.71	592.84			581
22	4 B2G	0	636.49	636.58			
23	3 AG	0	637.91	637.97			
24	3 B3G	0	651.22	651.26			642
25	4 AU	0.00022	673.88	674.12			685
26	4 B1G	0.0029	777.76	777.8			773
27	5 B3U	55.62972	778.42	778.54			
28	5 B2G	0	796.71	796.87	794	794	793
29	3 B2U	0.11724	797.61	797.72			
30	5 AU	0.00011	798.94	799.08			
31	3 B1U	0.87439	810.99	811.08			815
32	4 AG	0	823.37	823.46			
33	6 B3U	28.1843	849	849.08			853
34	6 B2G	0	894.95	895.13			
35	5 B1G	0	912.18	912.34			910

Vibe. modes	Symmetry	Intensity	Wave number 1/cm Cal. [HyperChem]	Wavenumber 1/cm Cal. [WinMopac]	Cal. cm ⁻¹	Exp. Cm ⁻¹	Cal. cm ⁻¹
					[32]		[33]
36	7 B3U	0.00045	931.92	932.1			
37	6 AU	0.00011	938.39	938.52			938
38	4 B3G	0	940.27	940.37			940
39	7 B2G	0	960.19	960.36			968
40	4 B1U	0.15287	979.57	979.74			969
41	6 B1G	0	990.69	990.83			983
42	7 AU	0.00011	1001.73	1001.89			
43	8 B3U	3.99791	1006.18	1006.28			
44	8 B2G	0	1015.28	1015.39	1018		1020
45	5 AG	0	1082.89	1083.24			1091
46	5 B3G	0	1117.67	1117.72	1110	1112	
47	4 B2U	0.045	1129.57	1129.97			
48	5 B1U	0.45894	1134.18	1134.36			
49	5 B2U	0.44051	1134.57	1134.66			
50	6 B3G	0	1146.16	1146.71			
51	6 B1U	0.02615	1148.13	1148.54			
52	6 AG	0	1163.26	1163.35	1182	1191	1177
53	7 B3G	0	1196.58	1196.73			1184
54	6 B2U	0.92369	1209.41	1209.6			
55	7 B1U	0.06871	1213.37	1213.6	1204	1217	1218
56	7 AG	0	1261.18	1261.34			1241
57	8 B3G	2.01679	1265.9	1265.74	1279	1284	1264
58	7 B2U	0.02091	1318.88	1318.24	1320	1313	1315
59	8 B2U	0.00078	1324.37	1324.55			
60	8 AG	0	1346.39	1346.56	1369	1374	1355
61	8 B1U	13.78876	1430.71	1430.95			
62	9 B3G	0	1442.99	1442.72			1435
63	9 AG	0	1460.48	1460.73			
64	9 B2U	8.0757	1469.06	1469.07			1471
65	9 B1U	4.89914	1499.86	1500.13			1521
66	10 AG	0.00004	1569.98	1570.41	1542	1532	
67	10 B1U	0.74697	1575.75	1576.11			
68	10 B3G	0	1594.93	1595.11			1583
69	11 AG	0	1598.91	1599.06			1586
70	10 B2U	0.96029	1635.18	1635.35			1628
71	11 B3G	0	1694.65	1694.91			
72	11 B2U	0.09353	1720.86	1721.07			
73	11 B1U	0.51825	1784.28	1784.43			
74	12 AG	0.00012	1784.78	1784.93			
75	13 AG	0	1791.74	1791.87			
76	12 B1U	2.03035	1797.88	1798.02			
77	12 B2U	0.14084	1813.14	1813.29			
78	12 B3G	0	1827.36	1827.52			
79	25.09984	25.09984	3002.33	3002.33			
80	14 AG	0.00008	3002.23	3002.44			
81	13 B1U	1.26978	3018.79	3019.05			
82	13 B3G	0.00001	3018.9	3019.13			3031
83	15 AG	0.03805	3052.61	3053.16			3040
84	14 B1U	19.16395	3052.61	3053.17			3041
85	14 B3G	0.00305	3053.8	3054.35			
86	14 B2U	9.8558	3053.82	3054.37			3061
87	15 B1U	37.8511	3070.76	3071.35			3063
88	16 AG	0.00049	3070.95	3071.52			3065
89	15 B2U	29.08017	3071.15	3071.75			
90	15 B3G	0.00002	3071.22	3071.81			

We conclude from the above table that the vibration between the atoms (C-H) at the wavenumber (796.71 cm⁻¹) [32] is close to the results of the measured literature, both experimentally and theoretically, and is equal to 794 cm⁻¹, which is also consistent with previous studies (793 cm⁻¹) [33]. To describe the vibration modes of the perylene molecule HyperChem8.0 a program was used, as the molecule is drawn and the special main axes are determined for being a non-linear molecule. According to the rule (3N-6), we get 90 basic vibrational frequencies, and these modes were described

through the program by clarifying the directions of vibration of the atoms with arrows with an indication of the intensity, and the symmetry of each mode, as shown in Figure 4.

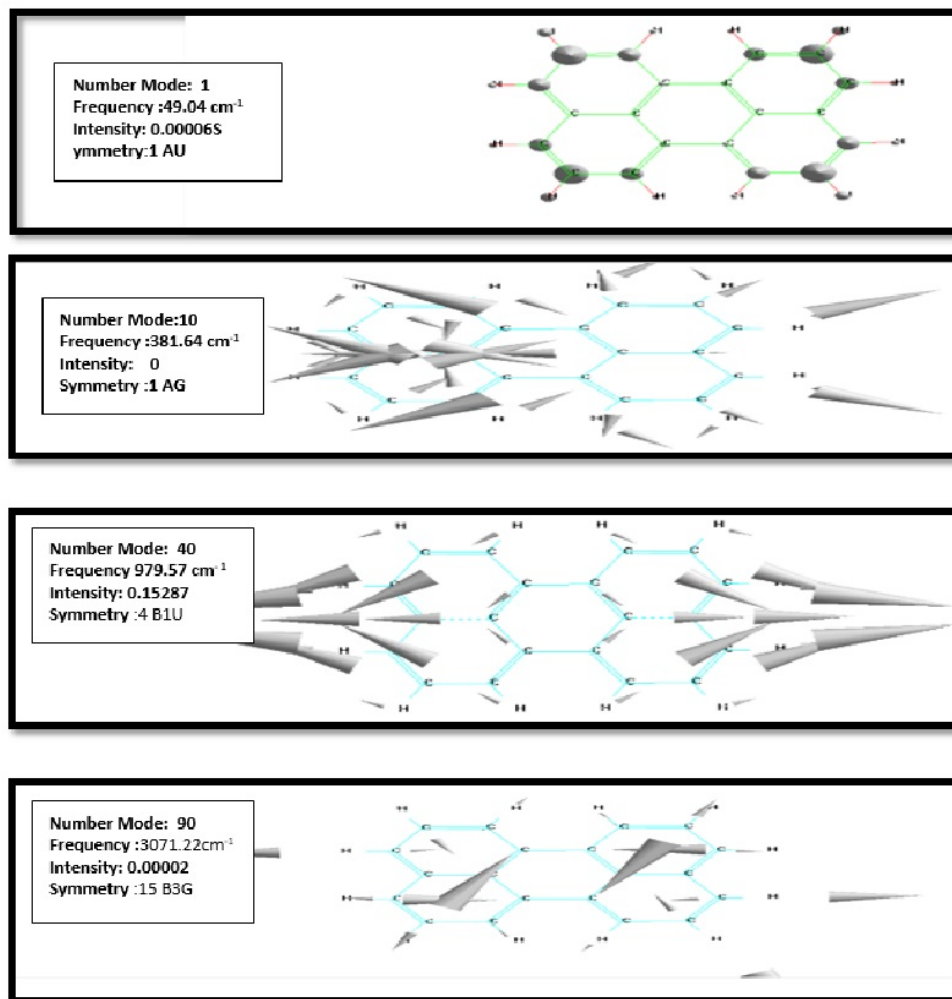


Figure 4. the basic vibrational modes of the perylene molecule were drawn using the HyperChem8.0 program, explaining the intensity, frequency and symmetry.

The Eigenvalues of the Orbitals of the Perylene Molecule

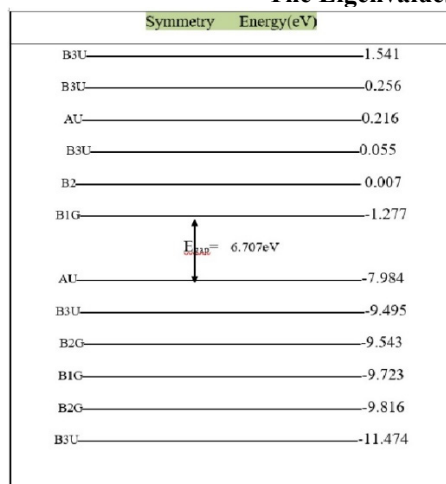


Figure 5. shows the values of the energy levels of the perylene molecule, showing the highest occupied molecular orbital (EHOMO) and the lowest unoccupied orbital (ELUMO), and the symmetry of each orbital calculated through the program HyperChem8.0

The energy levels of the perylene molecule were plotted using HyperChem8.0 software after the stable shape of the molecule was obtained, and the energy values for the highest occupied molecular orbital were equal to $\text{EHOMO} = -1.277 \text{ eV}$ and the lowest unoccupied molecular orbital, $\text{ELUMO} = -7.984 \text{ eV}$, and the symmetry of each orbit is shown in Figure 5. 46 was the number of orbitals occupied by the electrons, and 46 orbitals were unoccupied by the electrons. through which the energy gap between the two levels can be calculated ($E_g = \text{ELUMO} - \text{EHOMO}$) and is equal to 6.707 eV.

Electronic Properties of Perylene

After calculated the values of HOMO and LUMO for perylene molecules ($\text{C}_{20}\text{H}_{12}$), also calculated electronic properties (EA, IP) and calculated the global chemical indices such as (S, W, χ , η) by used semi-empirical way (MNDO-PM3) and was ($\text{IP} = 7.984 \text{ eV}$), ($\text{EA} = 1.277 \text{ eV}$), ($\chi = 4.6309 \text{ eV}$), ($\eta = 3.3535 \text{ eV}$), ($S = 1.6767 \text{ eV}$) and ($W = 3.197 \text{ eV}$). By using equations 2, 3, 4, and 5 respectively. Additional to previous study we can also calculate the parameter for total charge density and electrostatic potential, illustrated in (2D contours) as shown in Figure 6.

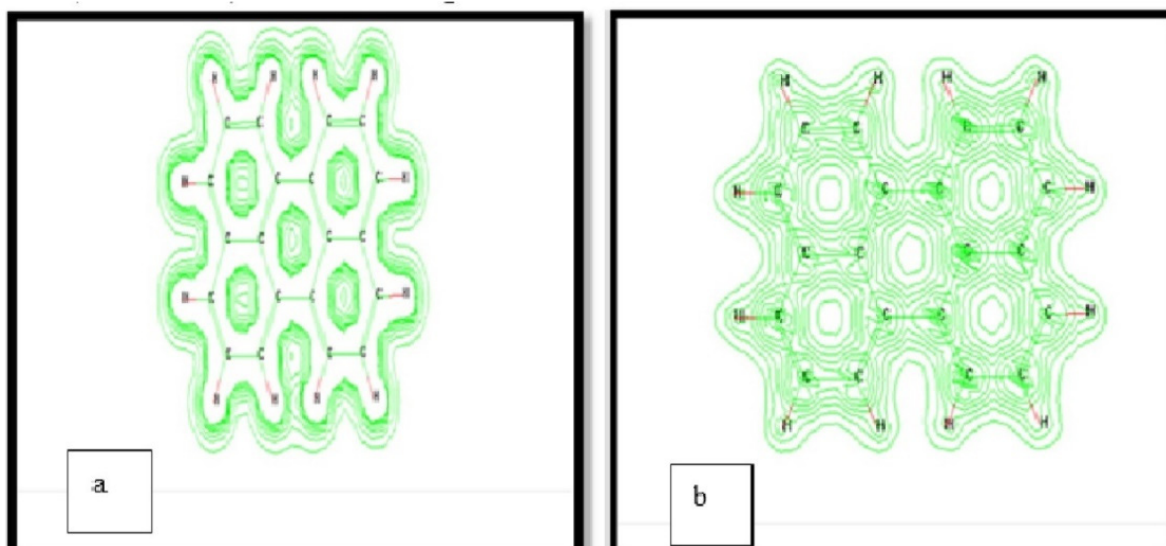


Figure 6. illustrated a- Electrostatic potential, b- Total charge density for perylene.

As we noticed from Figure 6b, the electronic charge density was centralized around the carbon atoms in the perylene molecule, in which the carbon atom is more negativity than the hydrogen atom. Figure 6a illustrates the electrostatic potential, which shows the plot of a contour map in 2D.

UV-Vis Spectroscopy of Perylene

The electronic transition was computed using the semi-empirical electronic spectrum from the configuration interaction (CI) method using the HyperChem8.0 program after obtaining the best balanced and stable geometric shape of the perylene molecule. Figure 7 depicts the absorption spectra, which exhibit two different bands (Q-band and B-band). The Q-band was found to be 412.3 nm, which is due to the π - π^* transition from the highest occupied molecular orbital (HOMO) to the lowest unoccupied molecular orbital (LUMO); this value agreed with previous studies, which found the Q-band to be 435 nm [34]. The B-band was identified to be 239.6 nm due to the transition from π levels to LUMO. Table 3 shows the absorbance range calculated between 180 and 650 nm.

Table 3. show the electron transition of perylene

Wavelength(nm)	Oscillator strength abs.
621.2	0
421.3	0.6192
346.8	0
343.9	0
334	0
332.4	0
323.8	0.0135
318.1	0
315.6	0
311.5	0
267.8	0
239.6	2.1082
235.5	1.5731
228.8	0
185.9	0
185.9	0
185.8	0.0006
185.8	0

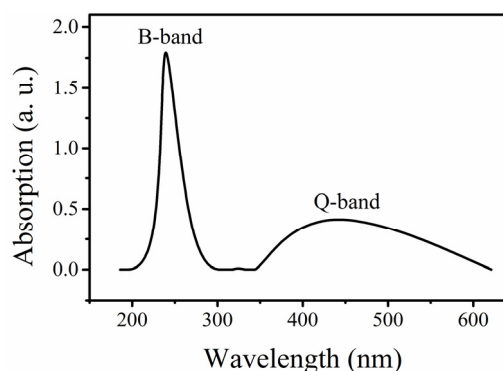


Figure 7. Absorption spectra of Perylene calculated by HyuperChem8.0 program

Thermodynamic Properties of Perylene Molecule

One of the important properties that have been studied is the thermal properties of the perylene molecule, which determine the most important conditions on the basis of which chemical reactions take place. After getting the energetically stationary shape of the molecule and obtaining the final matrix containing the charges of the atoms that make up the molecule through the WinMopac7.0 program, The MNDO-PM3 method has been used to obtain thermal functions during the three phases of the molecule, and for a number of temperatures that involve melting, boiling, and standard degrees, the dimensions between these atoms (r), the best position of these atoms (Opt.), the values of the angles (θ°) and the angles of the diagonal (α) are shown in Table 4.

Table 4. The final matrix of the perylene molecule is obtained from the WinMopac7.0, showing the interior coordinates (r , θ° , φ°) in the balance condition.

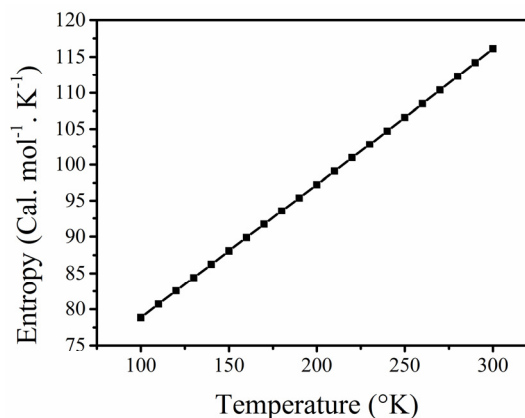
Atom	Distance	Opt.	Angle(θ°)	Opt.	Dihedral(φ°)	Opt.	A	B	C	Charge
C	.0000000	0	.000000	0	.000000	0	0	0	0	-.0148
C	1.4614239	1	.000000	0	.000000	0	0	0	0	-.0148
C	1.4269000	1	119.281700	1	.000000	0	2	1	0	-.0084
C	1.4268761	1	121.436500	1	.000000	1	3	2	1	-.0148
C	1.4614000	1	119.281700	1	.001296	1	4	3	2	-.0148
C	1.4269239	1	119.281700	1	.000000	1	1	2	3	-.0084
C	1.3796000	1	121.199400	1	179.999900	1	2	1	5	-.0997
C	1.4112239	1	119.281700	1	179.999900	1	3	2	1	-.0366
C	1.4201239	1	119.634900	1	.000000	1	8	3	2	-.0869
C	1.3692000	1	120.224400	1	-.001398	1	9	8	3	-.0970
C	1.4201000	1	119.633530	1	179.999900	1	8	3	2	-.0869
C	1.3692001	1	120.223029	1	.000000	1	11	8	3	-.0970
C	1.3796000	1	119.518777	1	.000000	1	4	3	8	-.0997
C	1.3796000	1	121.199400	1	.000000	1	5	4	3	-.0997
C	1.4112239	1	119.281700	1	179.999095	1	6	1	2	-.0366
C	1.4201239	1	119.634900	1	179.999900	1	15	6	1	-.0870
C	1.3692000	1	120.224500	1	-179.998899	1	16	15	6	-.0970
C	1.3796000	1	121.199400	1	.001170	1	1	2	7	-.0997
C	1.4091761	1	120.944600	1	.000000	1	18	1	6	-.0970
C	1.3692239	1	120.395300	1	.000000	1	19	18	1	-.0869
H	1.0949000	1	120.579301	1	179.999900	1	10	9	8	.1038
H	1.0957001	1	118.928407	1	179.999900	1	9	8	3	.1059
H	1.0957001	1	118.928408	1	179.999900	1	11	8	3	.1059
H	1.0949000	1	120.579197	1	179.999900	1	12	11	8	.1038
H	1.1011000	1	119.346230	1	179.999900	1	13	4	3	.1113
H	1.1011000	1	119.346330	1	179.999900	1	7	2	3	.1113
H	1.1011000	1	119.346230	1	179.999900	1	14	5	6	.1113
H	1.0949000	1	120.577930	1	179.999900	1	17	16	15	.1038
H	1.0957001	1	118.928403	1	179.999900	1	16	15	6	.1059
H	1.0957000	1	120.846999	1	179.999900	1	20	19	18	.1059
H	1.0949000	1	119.025200	1	179.999900	1	19	18	1	.1038
H	1.1011000	1	119.347700	1	179.999900	1	18	1	6	.1113

Heat of Formation

The heat of formation was computed for the perylene molecule in its energy-stable form and for various temperatures ranging from 100 to 300 °K (Table 5), as it included both the boiling and melting points as well as the standard temperature. Figure 8 shows that the heat of formation is temperature dependent and increases as temperature increases. The heat of formation at the standard temperature of 298 °K is 82 kcal.mol⁻¹, which is close to the result measured in the literature, which was 72.17 kcal.mol⁻¹ [35].

Table 5. The values of the heat of formation for the perylene molecule and their corresponding temperature

Temperature (K)	H. O. F. (kcal/mol)
100	74.641
110	74.839
120	75.052
130	75.282
140	75.53
150	75.794
160	76.077
170	76.379
180	76.7
190	77.04
200	77.4
210	77.781
220	78.181
230	78.603
240	79.044
250	79.507
260	79.991
270	80.495
280	81.021
290	81.568
300	82.135

**Figure 9.** The relationship between the entropy of the Perylene molecule and temperature

Entropy

Among the thermal properties that were calculated is the entropy for different temperatures to describe the randomness of the compound during the three phases, and the entropy value at the standard degree was 298K by (116) $\text{Cal}\cdot\text{mol}^{-1}\cdot\text{K}^{-1}$, which is close to the measured value from previous studies (112.14) $\text{Cal}\cdot\text{mol}^{-1}\cdot\text{K}^{-1}$ [35]. The randomness of the molecule begins to increase with increasing temperature as shown in Figure 9 and Table 6.

Table 6. the values of the entropy for the perylene molecule and their corresponding temperature

Temperature (K)	Entropy ($\text{Cal}\cdot\text{K}^{-1}\cdot\text{mol}^{-1}$)
100	78.8275
110	80.7091
120	82.5651
130	84.4049
140	86.2354
150	88.0617
160	89.8877
170	91.7162
180	93.5495
190	95.3889
200	97.2356
210	99.0904
220	100.9535
230	102.8253
240	104.7056
250	106.5943
260	108.4909
270	110.3951
280	112.3062
290	114.2237
300	116.1468

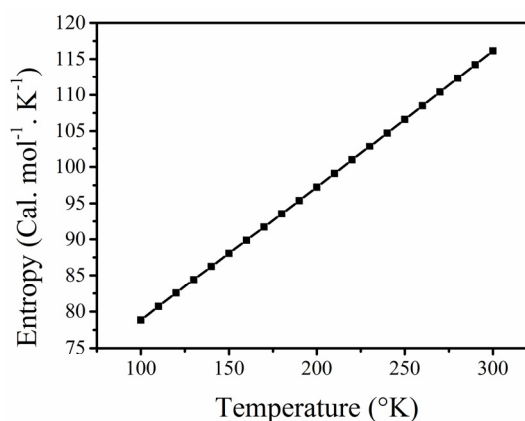


Figure 9. The relationship between the entropy of the Perylene molecule and temperature

Heat Capacity

The heat capacity of the perylene is a function of temperature and is directly proportional to it, as the increase in temperature increases the number of particles in the upper vibration energy level, and the heat capacity increases with constant pressure. At a temperature of 298 K and a pressure of 1 atmosphere, the heat capacity was 57.2 $\text{Cal}\cdot\text{mol}^{-1}\cdot\text{K}^{-1}$, which is close to the practical value of 49.13 $\text{Cal}\cdot\text{mol}^{-1}\cdot\text{K}^{-1}$ [35]. The heat capacity was also calculated for different values of temperature (100–300 °K) as shown in Figure 10 and Table 7.

Table 7. Shows the values between the heat capacity and temperature of perylene molecule

Temperature (K)	H. Capacity ($\text{Cal}\cdot\text{mol}^{-1}\cdot\text{K}^{-1}$)
100	18.9841
110	20.5394
120	22.1614
130	23.8464
140	25.5897
150	27.3865
160	29.2322
170	31.1223
180	33.0524
190	35.0182
200	37.0154
210	39.0396
220	41.0866
230	43.1519
240	45.2312
250	47.3203
260	49.415
270	51.5115
280	53.6057
290	55.6942
300	57.7737

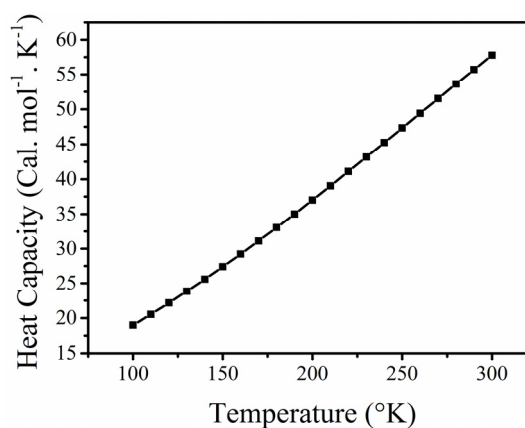


Figure 10. The relationship between heat capacity of perylene molecule and temperature

Enthalpy

The enthalpy function was determined for a variety of temperatures (Table 8) and represents the sum of the system's internal and external energy. and its value at standard temperature was $8740 \text{ Cal}\cdot\text{mol}^{-1}$, which is near to the sources determined by other methods, which were equal to $9080 \text{ Cal}\cdot\text{mol}^{-1}$, as shown in Figure 11. We observe that the enthalpy increases with rising temperature, demonstrating that the enthalpy is temperature dependent.

Table 8. Shows the values between the enthalpy and temperature of perylene molecule

Temperature (K)	Enthalpy (Cal.mol ⁻¹)
100	1248.9206
110	1446.4812
120	1659.9307
130	1889.919
140	2137.0529
150	2401.8915
160	2684.9465
170	2986.6841
180	3307.5262
190	3647.8512
200	4007.9947
210	4388.2489
220	4788.8627
230	5210.0414
240	5651.9468
250	6114.6978
260	6598.3715
270	7103.0042
280	7628.5934
290	8175.0994
300	8742.4478

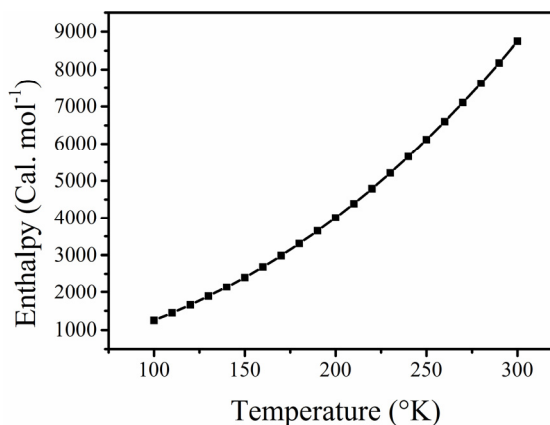


Figure 11. The relationship between the enthalpy and Perylene temperature

Gibbs Free Energy

After the change in entropy and enthalpy was calculated for the temperature range of 100–300 °K (Table 9) of the perylene molecule, the free energy of Gibbs was calculated in order to determine whether the reaction occurs spontaneously or not, using the equation ($\Delta G = \Delta E - T\Delta S$) and for the same temperatures. and it was at the standard temperature of $-2600.7 \text{ Cal}\cdot\text{mol}^{-1}$, and the relation between Gibbs's energy and temperature was drawn as in Figure 12. And the relationship was inverse between the two values; as the temperature increased, the free energy of Gibbs gradually decreased.

Table 9. the Gibbs free energy values of perylene molecule and the corresponding temperature

Temperature (K)	Gibbs=H-TS (Cal.mol)
100	-6633.8291
110	-7431.189
120	-8247.8813
130	-9082.718
140	-9935.90371
150	-10807.3635
160	-11697.0855
170	-12605.099
180	-13531.3838
190	-14476.3098
200	-15439.2053
210	-16420.7351
220	-17420.9073
230	-18439.7776
240	-19477.3972
250	-20533.8772
260	-21609.2625
270	-22703.6728
280	-23817.1426
290	-24949.7736
300	-26101.5922

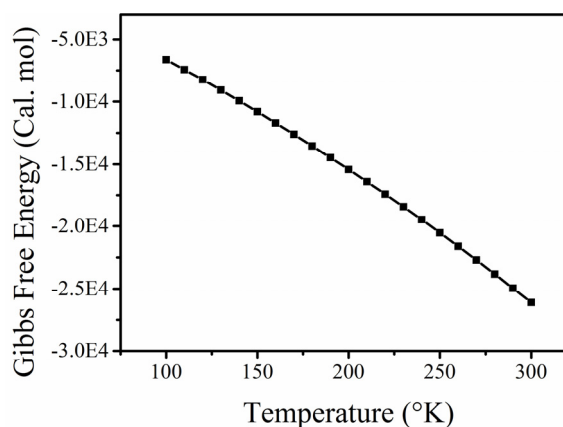


Figure 12. Show the relation between the Gibbs free energy and temperature of perylene molecule

CONCLUSIONS

The present study, show the results, that the (C-H) bond is the active bond in the molecule and the lowest energy of the perylene molecule to keep the molecule in a stable state was (-3961.45 eV). The equilibrium distance of the molecule was equal (1.1Å), and the dissociation energy of the molecule (C10-H21) was found to be (De = 182.44 kcal/mol.) and (C17-H28) (De = 209.08 kcal/mol. We conclude that the molecule begins to dissociate when the length of the bond breaks down and the energy at this point called the dissociation energy. With regard to the thermal properties, we note the direct proportionality of (ΔH_f , CP, H, S) with temperature and the interpretation of this according to quantum mechanics, as the thermal energies arising from both the transitional movement and the rotational and vibrational motion of the molecule are quantum energies and all of them are directly proportional to the temperature. As for high temperatures, electronic movement plays an important role, as high energies cause electronic transitions. Also, the increase in the values of Entropy with an increase in temperature is due to the increase in the energy diffusion related to the rotational and vibration energies. And as for the heat of formation, the positive values indicate that the compound is endothermic. The energy gap control of organic semiconductors is important for many applications, for example, light-emitting diode and organic photovoltaic devices.

ORCID IDs

✉ Rosure Borhanalden Abdulrahman, <https://orcid.org/0000-0003-3439-5672>

REFERENCES

- [1] M. Zhu, and C. Yang, Chem. Soc. Rev. **42**, 4963–4976 (2013). <https://doi.org/10.1039/C3CS35440G>
- [2] L. Dou, Y. Liu, Z. Hong, G. Li, and Y. Yang, Chemical Reviews, **115**, 12633–12665 (2015). <https://doi.org/10.1021/acs.chemrev.5b00165>
- [3] Y. Yao, H. Dong, and W. Hu, Advanced Materials, **28**, 4513–4523 (2016). <https://doi.org/https://doi.org/10.1002/adma.201503007>
- [4] H. Bronstein, C.B. Nielsen, B.C. Schroeder, and I. McCulloch, Nature Reviews Chemistry, **4**, 66–77 (2020). <https://doi.org/10.1038/s41570-019-0152-9>
- [5] M. Fröbel, F. Fries, T. Schwab, S. Lenk, K. Leo, M.C. Gather, and S. Reineke, Scientific Reports, **8**, 9684 (2018). <https://doi.org/10.1038/s41598-018-27976-z>
- [6] D.-H. Kim, A. D'Aléo, X.-K. Chen, A. D. S. Sandanayaka, D. Yao, L. Zhao, T. Komino, E. Zaborova, G. Canard, Y. Tsuchiya, E. Choi, J. W. Wu, F. Fages, J.-L. Brédas, J.-C. Ribierre, and C. Adachi, Nature Photonics, **12**, 98–104 (2018). <https://doi.org/10.1038/s41566-017-0087-y>
- [7] K. Tuong Ly, R.-W. Chen-Cheng, H.-W. Lin, Y.-J. Shiau, S.-H. Liu, P.-T. Chou, C.-S. Tsao, Y.-C. Huang, and Y. Chi, Nature Photonics, **11**, 63–68 (2017). <https://doi.org/10.1038/nphoton.2016.230>
- [8] D. Baran, N. Gasparini, A. Wadsworth, C. H. Tan, N. Wehbe, X. Song, Z. Hamid, W. Zhang, M. Neophytou, T. Kirchartz, C.J. Brabec, J.R. Durrant, and I. McCulloch, Nature Communications, **9**, 2059 (2018). <https://doi.org/10.1038/s41467-018-04502-3>
- [9] M. Ameri, M. Ghaffarkani, R. T. Ghahrizjani, N. Safari, and E. Mohajerani, Solar Energy Materials and Solar Cells, **205**, 110251 (2020). <https://doi.org/https://doi.org/10.1016/j.solmat.2019.110251>
- [10] W. Tang, Y. Huang, L. Han, R. Liu, Y. Su, X. Guo, and F. Yan, Journal of Materials Chemistry C, **7**, 790–808 (2019). <https://doi.org/10.1039/C8TC05485A>
- [11] Y. Huang, E.-L. Hsiang, M.-Y. Deng, and S.-T. Wu, Light: Science and Applications, **9**, 105 (2020). <https://doi.org/10.1038/s41377-020-0341-9>
- [12] T. Okamoto, C. P. Yu, C. Mitsui, M. Yamagishi, H. Ishii, and J. Takeya, Journal of the American Chemical Society, **142**, 9083–9096 (2020). <https://doi.org/https://doi.org/10.1021/jacs.9b10450>
- [13] J. Sun, Y. Choi, Y. J. Choi, S. Kim, J.-H. Park, S. Lee, and J. H. Cho, Advanced Materials, **31**, 1803831 (2019). <https://doi.org/https://doi.org/10.1002/adma.201803831>
- [14] M. Duan, L. Jiang, B. Shao, C. Feng, H. Yu, H. Guo, H. Chen, and W. Tang, Applied Catalysis B: Environmental, **297**, 120439 (2021). <https://doi.org/10.1016/j.apcatb.2021.120439>
- [15] R. Roccanova, A. Yangui, H. Nhalil, H. Shi, M.-H. Du, and B. Saparov, ACS Applied Electronic Materials, **1**, 269–274 (2019). <https://doi.org/10.1021/acsaem.9b00015>
- [16] J. Tao, D. Liu, J. Jing, H. Dong, L. Liu, B. Xu, and W. Tian, Advanced Materials, **33**, 2105466 (2021). <https://doi.org/10.1002/adma.202105466>
- [17] J. D. Yuen, V. A. Pozdin, A. T. Young, B. L. Turner, I. D. Giles, J. Naciri, S. A. Trammell, P. T. Charles, D. A. Stenger, and M. A. Daniele, Dyes and Pigments, **174**, 108014 (2020). <https://doi.org/10.1016/j.dyepig.2019.108014>
- [18] A. G. Macedo, L. P. Christopholi, A. E. X. Gavim, J. F. de Deus, M. A. M. Teridi, A. R. bin M. Yusoff, and W. J. da Silva, Journal of Materials Science: Materials in Electronics, **30**, 15803–15824 (2019). <https://doi.org/10.1007/s10854-019-02019-z>
- [19] M. Zhang, J. Shi, C. Liao, Q. Tian, C. Wang, S. Chen, and L. Zang, Chemosensors, **9**, 1 (2020). <https://doi.org/10.3390/chemosensors9010001>
- [20] É. Torres, M. N. Berberan-Santos, and M. J. Brites, Dyes and Pigments, **112**, 298–304 (2015). <https://doi.org/10.1016/j.dyepig.2014.07.019>
- [21] M. Zhang, Y. Bai, C. Sun, L. Xue, H. Wang, and Z.-G. Zhang, Science China Chemistry, **65**, 462–485 (2022). <https://doi.org/10.1007/s11426-021-1171-4>
- [22] K. Nie, X. Peng, W. Yan, J. Song, and J. Qu, Journal of Bio-X Research, **3**, 174–182 (2020). <https://doi.org/10.1097/JBR.0000000000000081>
- [23] A. Sugie, W. Han, N. Shioya, T. Hasegawa, and H. Yoshida, The Journal of Physical Chemistry C, **124**, 9765–9773 (2020). <https://doi.org/10.1021/acs.jpcc.0c01743>
- [24] P. Bultinck, T. Kuppens, X. Gironés, and R. Carbó-Dorca, Journal of Chemical Information and Computer Sciences, **43**, 1143–1150 (2003). <https://doi.org/10.1021/ci0340153>
- [25] G. Halder, *Introduction to chemical engineering thermodynamics*, 2nd ed (PHI Learning Pvt. Ltd., 2014).

- [26] B. Schrader, ed., *Infrared and Raman spectroscopy: methods and applications* (John Wiley & Sons, 2008).
- [27] S. Aronson, B. Strumeyer, and R. Goodman, *The Journal of Physical Chemistry*, **76**, 921–925 (1972). <https://doi.org/10.1021/j100650a024>
- [28] J. I. Gersten and F. W. Smith, *The physics and chemistry of materials* (Toronto: Wiley New York, 2001).
- [29] C.-G. Zhan, J. A. Nichols, and D. A. Dixon, *The Journal of Physical Chemistry A*, **107**, 4184–4195 (2003). <https://doi.org/10.1021/jp0225774>
- [30] Siyamak Shahab and Masoome Sheikhi, *Russian Journal of Physical Chemistry B*, **14**, 15–18 (2020). <https://doi.org/https://doi.org/10.1134/S1990793120010145>
- [31] W. D. Callister and D. G. Rethwisch, *Materials science and engineering: an introduction*, 10th ed (New York: Wiley, 2018).
- [32] J. Bouwman, P. Castellanos, M. Bulak, J. Terwisscha van Scheltinga, J. Cami, H. Linnartz, and A. G. G. M. Tielens, *Astronomy and Astrophysics*, **621**, A80 (2019). <https://doi.org/https://doi.org/10.1051/0004-6361/201834130>
- [33] R. M. Kubba, M. U. Al-Dilemy, and M. Shanshal, *National Journal of Chemistry*, **38**, 293–310 (2010).
- [34] J. M. Dixon, M. Taniguchi, and J. S. Lindsey, *Photochemistry and Photobiology*, **81**, 212–213 (2007). <https://doi.org/10.1111/j.1751-1097.2005.tb01544.x>
- [35] G. Blanquart, and H. Pitsch, *The Journal of Physical Chemistry A*, **111**, 6510–6520 (2007). <https://doi.org/10.1021/jp068579w>

**НАПІВЕМПІРИЧНЕ ДОСЛІДЖЕННЯ ЕЛЕКТРОННИХ, КОЛИВАЛЬНИХ ТА ТЕРМОДИНАМІЧНИХ
ВЛАСТИВОСТЕЙ МОЛЕКУЛИ ПЕРИЛЕНУ (C₂₀H₁₂)**

Абдул Хакім Ш. Мохаммед^а, Ісса З. Хассан^а, Хасан А. Кадхем^б, Росуре Борханалден Абдулрахман^с

^а*Факультет фізики, освітній коледж чистих наук, університет Кіркука, Кіркук, Ірак*

^б*Міністерство освіти, відкритий освітній коледж, Кіркук центр, Ірак*

^с*Факультет фізики, науковий коледж, університет Кіркука, Кіркук, Ірак*

В роботі методом обчислювання досліджено спектроскопічні та термодинамічні властивості молекули перилену (C₂₀H₁₂) у газовій фазі за допомогою програм напівемпіричного методу [Nucor Chem8.0 і WinMoras7.0] через (MNDO-PM3). Цей спосіб забезпечує більшу простоту і швидкість роботи. Були розраховані електронні властивості, такі як повна енергія, енергія дисоціації, молекулярна орбіталь, потенціали іонізації, електронна спорідненість та енергетична щільність. Також були розрахований УФ-видимий спектр та проведено вібраційний аналіз. Крім того, були розраховані термодинамічні властивості при стандартній температурі, такі як теплота утворення, ентропія, ентальпія, теплоємність і вільна енергія Гіббса.

Ключові слова: *перилен; C₂₀H₁₂; енергія молекули; видимий УФ; ІЧ; MNDO-PM3; термодинаміка*

SEMI-EMPIRICAL PREDICTIONS FOR HARDNESS OF RARE EARTH PYROCHLORES; HIGH-PERMITTIVITY DIELECTRICS AND THERMAL BARRIER COATING MATERIALS[†]

 **Rekha Bhati**^a,  **Dheerendra Singh Yadav**^b,  **Preeti Varshney**^c,
 **Rajesh Chandra Gupta**^d,  **Ajay Singh Verma**^{e,f,*}

^aDepartment of Natural and Applied Sciences, Glocal University, Saharanpur-247232 (India)

^bDepartment of Physics, Ch. Charan Singh P G College Heonra, Etawah 206001 (India)

^cDepartment of Physics, G.G.I.C., Iglas, Aligarh 202124 (India)

^dDepartment of Physics, B. S. A. College, Mathura 281004 (India)

^eDivision of Research & Innovation, Department of Applied and Life Sciences, Uttaranchal University, Dehradun, Uttarakhand (India) 284007

^fUniversity Centre for Research and Development, Department of Physics, Chandigarh University, Mohali, Punjab-140413 (India)

*Corresponding Author e-mail: ajay_phy@rediffmail.com

Received January 16, 2023; accepted February 16, 2023

Herein, we have formulated a simplistic semi-empirical model for Vicker's hardness of rare earth based pyrochlore compounds. We have considered the $A_2^{3+}B_2^{4+}O_7$ structured 97 pyrochlore compounds for Vicker's hardness calculations. The plasmon energy ($\hbar\omega_p$) depends on basic parameters of the material such as N_e -effective number of free electrons per unit volume participating in plasma oscillations, e -electronic charge and m -mass of an electron. The proposed model predicts that the experimental and theoretical values of Vicker's hardness increases as plasmon energy of pyrochlore increases. We have found that the calculated values are in better agreement with available experimental and theoretical data, which supports the validity of the model. This model supports the modeling of emerging functional pyrochlore compounds and helps to understand their mechanical properties for excellent thermal stability, superconductivities, batteries, ferroelectricity, water spitting, high ionic conductivity, good photoluminescence, inherent oxygen vacancies, exotic magnetism, and now-a-days most importantly in nuclear waste encapsulation and aerospace industry.

Keywords: Pyrochlores; Plasmon energy; Vicker's hardness

PACS: 71.20.-b; 31.10.+Z; 81.05.Je; 61.50.-f; 81.70-q.

1. INTRODUCTION

Pyrochlore crystals have been a rapidly growing area of research for scientific community due to their unique technological applications such as exotic magnetism, low thermal conductivity (thermal barrier coatings on diesel engines), anti-erosion of Ag, nuclear waste management, catalysis, sensors, oxide fuel cell, lasers, and in various electronic devices due to unique crystal structure; and the broad range of the study of physical, electronic, mechanical, optical and thermal properties [1-4]. Oxides with Pyrochlore structure having rare earth (A) elements with the common formula ($A_2^{3+}B_2^{4+}O_7$) ($A^{3+} = La^{3+}, Ce^{3+}, Pr^{3+}, Nd^{3+}, Sm^{3+}, Eu^{3+}, Gd^{3+}, Tb^{3+}, Dy^{3+}, Ho^{3+}, Er^{3+}, Tm^{3+}, Yb^{3+}, Lu^{3+}$ and Y^{3+} and $B^{4+} = Sn^{4+}, Ti^{4+}, Zr^{4+}, Hf^{4+}, Ru^{4+}, Ir^{4+}$ etc), possess a different kind of the real-world uses since they have great melting points, large thermal expansion coefficient, high structural stability and low thermal conductivity [5-9]. Their complicated chemical structures make them susceptible to being quickly accommodated faults [10]. Pyrochlores are therefore a very promising candidate for usage as high-permittivity dielectrics [7], thermal barrier coatings (TBCs), solid-state electrolytes [12], nuclear wastage hosts [13] and catalysis [14]. Due to the numerous features of pyrochlores, research is being done to maximize the effectiveness of each attribute while maintaining the chemical and physical durability as well as the thermal consistency of pyrochlores. Liu et al. [13] carefully investigated $La_2R_2O_7$ ($R = Ge, Ti, Sn, Zr, Hf$) pyrochlores and noticed less heat conduction. It is too revealed why the La-O weak bonds affect the thermal and mechanical characteristics of these $La_2R_2O_7$ pyrochlores. Using density functional theory, the electronic structure, thermal and mechanical properties of Th-doped $Gd_2Zr_2O_7$ compounds studied by Zhao et al [15]. Feng et al. [4] predicted the elastic properties of rare earth stannate pyrochlores through density functional theory and ultrasonic resonance method.

Rare earth (Stannate, Titanate, Zirconate, Germanate and Hafnate) pyrochlore solids are of the molecular formula $A_2^{3+}B_2^{4+}O_7$, here A & B are metallic cations these can be either divalent and pentavalent or trivalent and tetravalent, respectively [16]. Rare earth pyrochlores ($A_2^{3+}B_2^{4+}O_7$) display cubic symmetry, space group $Fd-3m$, No. (227) with eight formula units per unit cell, wherein one-eighth of the anions are vacant to ensure charge neutrality and the cations form a face-centered cubic (FCC) array [17]. A-type cations occupy the $16d$ (0.5, 0.5, 0.5) sites and the tetravalent atom B-type of cations occupy the $16c$ (0, 0, 0) sites. Oxygen atom is situated at two locations: $O1$ is located on the $8b$ (0.375, 0.375, 0.375) site and $O2$ on the $48f$ ($x, 0.125, 0.125$) site [18] respectively. Lattice of atoms is completely explained in terms of structure parameter x defining the position of O (48f) atoms and the lattice size a . The x parameter determines the equilibrium position of O (48f) when, $0.3125 \leq x \leq 0.375$, and affects the local coordination around the A^{3+} and

[†] **Cite as:** R. Bhati, D.S. Yadav, P. Varshney, R.C. Gupta, and A.S. Verma, East Eur. J. Phys. 1, 222 (2023), <https://doi.org/10.26565/2312-4334-2023-1-29>

© R. Bhati, D.S. Yadav, P. Varshney, R.C. Gupta, A.S. Verma, 2023

B^{4+} cations [17]. In the ideal pyrochlore structure with $x = 0.3125$ A-atoms and the B-atoms are coordinated at distorted cubes and regular octahedral, respectively. As the value of x approaches 0.375, the polyhedral at B site transform into tetragonal anti-prisms, while polyhedral of the rare earth elements at A-site become ordinary cubes. This arrangement of atoms is stable when, $1.46 \leq r_A/r_B \leq 1.78$ (r_A and r_B denote the radii of A^{3+} and B^{4+} cations, respectively) [19], while $(r_A/r_B) < 1.46$ results in a stable fluorite structure. In configuration, the bigger A^{3+} cation is surrounded by two O (8b) and six O (48f) atoms and the smaller B^{4+} cation is surrounded by six O (48f) atoms in a distorted octahedron. Here, the 48f oxygen atom is coordinated to two A^{3+} and two B^{4+} sites, while the 8b oxygen atom is contained within an A^{3+} cation-formed tetrahedron.

In particular, hardness is one of the most important physical parameters that characterizes the mechanical properties of materials. Vicker's micro-hardness has been shown correlated nicely with the strength and bulk modulus in numerous materials [20,21]. On the basis of chemical bonds and effect of valence d -electrons, the hardness of covalent compounds studied by Guo et al. [22]. Jhi and other workers [23] have developed the correlation between valence electrons concentrations and hardness for semiconducting materials. Recently, Yang et al. [24] have studied the physical parameters of $La_2B_2O_7$ (B = Zr, Sn, Hf, Ge) pyrochlores using First-principles techniques. Feng et al. [25] have reported the electronic structure, mechanical properties and thermal conductivity of $Ln_2Zr_2O_7$ (Ln = La, Pr, Nd, Sm, Eu, Gd) pyrochlores employing the local-density approximation (LDA) of spin polarized scheme +U calculations and next to it verified by experimental results and confirm that studied compounds are promising thermal barrier coating (TBC) materials. However, studies of $Ln_2B_2O_7$ (B = Hf, Ge, Ru, Ir) with pyrochlore structures are still insufficient.

Recently, theoretical studies rely on empirical relationships becomes a crucial component of crystallography study. The empirical relationships have always been evolved as a uncomplicated, ready to use, and to produce improved outcomes for physical parameters. Empirical relationships are most often accepted as the preferred technique for computational solid-state investigations. In earlier researches, author and co-workers have been reported the structural, mechanical and electronic properties of zinc-blende and rock-salt structured binary and ternary tetrahedral chalcopyrite semiconductors using various methods successfully [26-34]. Even though empirical relations frequently don't produce incredibly accurate answers for each unique substance, they can nevertheless be extremely helpful. To the best of my knowledge, mechanical property, particularly Vicker's hardness, has not been studied theoretically using POT of solids in rare earth pyrochlore oxides, till date. Therefore, to bridge this gap, it would be interesting to offer a different rationale for the vicker's hardness of cubic-structured pyrochlore oxides. Herein, a model obtained from POT of solids is being put forward to investigate the mechanical properties of rare earth pyrochlore oxides. It is now widely accepted that a metal's plasmon energy changes [28-35], when it combines chemically to create a compound, conduction electrons in a metal are collectively excited to form plasma of energy $\hbar\omega_p$. This energy depends upon the density of conduction band. Hence the plasmon energy is affected by the density of conduction electrons as well as effective number of valence electrons, both of which change in the formation of compound.

In present work, the relationship between vicker's hardness and plasmon energy for the cubic structured pyrochlore oxides ($A_2^{+3}B_2^{+4}O_7$) (A = La → Lu, Y & B = Sn, Ti, Zr, Hf, Ge, Ru, Ir) has been discussed employing the plasma oscillation theory (POT) of valence electrons in solids. In investigation of hardness, effect of valence d -electrons of the metal has been taken into account and the obtained values of vicker's hardness is in compliance with available experimental data as compared to previous theoretical investigations on the same. This model divulges vicker's hardness unprecedentedly and accurately for many pyrochlores.

2. THEORETICAL FORMALISM OF HARDNESS

The hardness as a characteristic of pyrochlore crystals has been proved a crucial physical parameter, which determines the bond strengths in these crystals. The term hardness refers to stiffness or temper, resistance to scratching, abrasion, or cutting. The elastic and plastic deformation characteristics of solid materials are usually related to hardness. The metal handbook defines the hardness; the resistance of a material to plastic deformation is measured by its hardness. A true scientific definition of hardness has yet to come. This is due to the fact that hardness is influenced by a variety of factors. As a result, a number of different hardness measurement methods have been evolved. Hardness is a mechanical property that delineates not only the state of material under consideration, but also some deeper basic features of the material, such as the chemical bonding character. Many theoretical approaches to determining the hardness of solids have been presented. Among them Vicker's and Knoop hardness scales are most often used to measure this mechanical parameter. However, it is not remarkable that only the resultant force per unit area could play a key role in determining the hardness of the materials. Since, the hardness of the metal and compound is determined by the energy of the quanta in plasma oscillations of the valence electrons and is given as [35-36],

From the classical consideration, we get the frequency of plasmon oscillations as

$$\omega_p = (4\pi N_e e^2 / m)^{0.5}$$

Hence the amount of energy given to plasmon becomes

$$\hbar\omega_p = \hbar (4\pi N_e e^2 / m)^{0.5} \quad (1)$$

Here $\hbar\omega_p$ is the plasmon energy, N_e -effective no. of free electrons per unit volume participating in plasma oscillations; e -electronic charge and m -mass of an electron.

For a compound, the plasmon energy in Eq. (1) may also be defined as [36]

$$\hbar\omega_p = 28.8 (Z\sigma/W)^{0.5} \quad (2)$$

Eq. (2) is valid for free electrons and up to first approximation. It can be employed for insulators and semiconductors. During last four decades, Kumar [37] has explored the relationships for electronic properties of chalcopyrite solids in term of plasmon energy. Gupta et al [34] and Verma et al [38] have established a relationships between the mechanical properties and melting point, inter-atomic distance and ionicity of the compounds.

Verma et al. [38] have developed an empirical relation between micro-hardness and bulk modulus for tetragonal structured chalcopyrite solids as follows

$$H = KB^{K+1} \quad (4)$$

where K is crystal structure dependent constant with values of 0.50 and 0.59 for I – III– VI₂ and II – IV– V₂ chalcopyrites, respectively.

Previously, many researchers have studied the static, dynamical, optical, mechanical and electronic properties of binary and ternary chalcopyrites semiconductors, and rare earth chalcogenides using empirical models based on plasmon oscillation theory of solids [28-34]. As per above study, the mechanical properties of pyrochlores have a fundamental relationship between hardness H and plasmon energy $\hbar\omega_p$.

Physical parameters are obviously important for device development, but no one has demonstrated meaningful results on Vicker's hardness using various approaches. As, this modulus is much valance electrons dependent. Hence, we tried a new empirical approach to come across accurate results close to experimental values using plasmon energy of compound.

The experimental vicker's hardness H_v [GPa] of these pyrochlores shows linearity when plotted a graph with respect to plasmon energy $(\hbar\omega_p)^{3/4}$ and presented in Figure 2.2. It is noteworthy that the method of determining bulk modulus by this mechanism creates a difference from experimental techniques, and this could develop errors.

It is macro and micro changes in the compounds characteristic which leads to mechanical changes; here, it is plasmon energy of valance electrons that defines this macro and micro change in the compound. As a result, a linear regression line is plotted for the vicker's hardness, which results in an expression of vicker's hardness [GPa] as;

$$H_v = P + Q \times (\hbar\omega_p)^{3/4} \quad (5)$$

Here constants P and Q, and regression coefficient R are presented in Table 1. In this table probability parameter S shows the significance of regression as null i.e. there is no correlation.

Table 1. Ternary tetrahedral semiconductors data gives the following linear regression result.

Property	P	Q	R	S
Vicker's Hardness	-84.6281±10.4998	9.6743±1.0566	0.9660	<0.0001

A detailed study of elastic properties such as hardness of complex structured pyrochlores, covalent crystals and binary solids has been given elsewhere [34, 35] and will not be discussed here. The properties of A₂B₂O₇ pyrochlore compounds have been thoroughly studied and some of these materials have been noticed for practical applications [4-10]. The information about elastic properties of pyrochlores such as hardness is rather incomplete and experimental data found only for few pyrochlores. This study suggests the elastic properties in more accurate manner.

3. RESULT AND DISCUSSION

In the present study, it is shown that empirical relationship exists for pyrochlores and this can be successfully employed to investigate the hardness from their plasmon energy as a key parameter.

The investigated values of hardness of these materials have been given in Table 2 and weighed against the available experimental data and other such theoretical investigations reported so far. Vicker's hardness of these crystals exhibits a linear relationship when plotted against their Plasmon energy $\hbar\omega_p$ (in eV), which are calculated using the relation (2) and falls on a straight line. From Fig. 2.1, it is obvious that the hardness follows rising trends in these compounds with their increasing plasma energy.

It can be seen that the values of hardness computed from this proposed empirical relation is in better conformity with experimental data in comparison to the values reported by earlier workers. As an illustration the results obtained for H_v (in GPa) vary from experimental values by the amount as follows: 1.43% for La₂Sn₂O₇, 0.20% for Nd₂Sn₂O₇, 0.86% for Sm₂Sn₂O₇, 1.44% for Gd₂Sn₂O₇, 3.61% for Er₂Sn₂O₇, 4.50% for La₂Zr₂O₇, 1.67% for Pr₂Zr₂O₇, 7.33% for Nd₂Zr₂O₇, 5.77% for Sm₂Zr₂O₇ and 13.67% for Eu₂Zr₂O₇. A few higher deviations of hardness values in these compounds are owing to larger bond lengths. With increasing bond length, plasmon energy decreases, which widen the variance of these results. Another reason for greater deviations of hardness values is unit cells mismatch between substrate and deposited films. Explicitly hardness of ternary compounds is more sensitive with plasmon energy as observed in calculated values.

Table 2: Calculated values of vicker's hardness H_v (in GPa) of pyrochlores.

Vicker's Hardness (Hv)				Vicker's Hardness (Hv)				Vicker's Hardness (Hv)						
$A_2B_2O_7$	H_{v0p} (eV) [Eq. 2]	Cal. [Eq. 5]	Expt. [4,25]	Reported [4, 13, 25]	$A_2B_2O_7$	H_{v0p} (eV) [Eq. 2]	Cal. [Eq. 5]	Expt. [4, 25]	Reported [4, 13, 25]	$A_2B_2O_7$	H_{v0p} (eV) [Eq. 2]	Cal. [Eq. 5]	Expt. [4, 25]	Reported [4, 13, 25]
$La_2Sn_2O_7$	21.051	10.449	10.6±0.2	14, 14.9	$Pr_2Zr_2O_7$	21.088	10.574	10.40	12.10	$Sm_2Ru_2O_7$	22.391	13.09		
$Ce_2Sn_2O_7$	21.091	10.584			$Nd_2Zr_2O_7$	21.135	10.733	10.00	11.70	$Eu_2Ru_2O_7$	22.460	13.22		
$Pr_2Sn_2O_7$	21.202	10.960			$Sm_2Zr_2O_7$	21.402	11.635	11.00	10.70	$Gd_2Ru_2O_7$	22.539	13.38		
$Nd_2Sn_2O_7$	21.280	11.223	11.20±0.4	16.00	$Eu_2Zr_2O_7$	21.491	11.935	10.50	9.60	$Tb_2Ru_2O_7$	22.612	13.52		
$Sm_2Sn_2O_7$	21.571	12.205	12.10±0.6	16.60	$Gd_2Zr_2O_7$	21.583	12.245	10.00	12.30	$Dy_2Ru_2O_7$	22.759	13.82		
$Eu_2Sn_2O_7$	21.660	12.504			$Tb_2Zr_2O_7$	21.743	12.783			$Ho_2Ru_2O_7$	22.793	13.89		
$Gd_2Sn_2O_7$	21.682	12.578	12.40±0.2	16.70	$Dy_2Zr_2O_7$	21.825	13.059			$Er_2Ru_2O_7$	22.908	14.12		
$Tb_2Sn_2O_7$	21.771	12.877			$Ho_2Zr_2O_7$	21.922	13.384			$Tm_2Ru_2O_7$	22.976	14.26		
$Dy_2Sn_2O_7$	21.862	13.183			$Er_2Zr_2O_7$	21.998	13.639			$Yb_2Ru_2O_7$	23.055	14.43		
$Ho_2Sn_2O_7$	21.960	13.511			$Tm_2Zr_2O_7$	22.084	13.927			$Lu_2Ru_2O_7$	23.041	14.40		
$Er_2Sn_2O_7$	22.070	13.880	14.40±0.3	17.90	$Yb_2Zr_2O_7$	22.187	14.271			$Pr_2Ir_2O_7$	21.963	12.27		
$Tm_2Sn_2O_7$	22.132	14.087			$Y_2Zr_2O_7$	21.792	12.948			$Nd_2Ir_2O_7$	22.023	12.38		
$Yb_2Sn_2O_7$	22.240	14.448			$La_2Hf_2O_7$	20.848	9.760		8.90	$Sm_2Ir_2O_7$	22.284	12.88		
$Lu_2Sn_2O_7$	22.301	14.652			$Ce_2Hf_2O_7$	21.210	10.987			$Eu_2Ir_2O_7$	22.297	12.90		
$Y_2Sn_2O_7$	22.320	14.716			$Pr_2Hf_2O_7$	21.246	11.108			$Gd_2Ir_2O_7$	22.414	13.13		
$La_2Ti_2O_7$	21.980	13.578			$Nd_2Hf_2O_7$	21.267	11.179			$Tb_2Ir_2O_7$	22.559	13.42		
$Sm_2Ti_2O_7$	22.051	13.816			$Sm_2Hf_2O_7$	21.469	11.861			$Dy_2Ir_2O_7$	22.612	13.52		
$Eu_2Ti_2O_7$	22.161	14.184			$Eu_2Hf_2O_7$	22.110	14.014			$Ho_2Ir_2O_7$	22.689	13.68		
$Gd_2Ti_2O_7$	22.180	14.248			$Gd_2Hf_2O_7$	21.610	12.336			$Er_2Ir_2O_7$	22.772	13.85		
$Tb_2Ti_2O_7$	22.212	14.355			$Tb_2Hf_2O_7$	21.765	12.857			$Tm_2Ir_2O_7$	22.847	14.00		
$Dy_2Ti_2O_7$	22.293	14.625			$Dy_2Hf_2O_7$	21.891	13.280			$Yb_2Ir_2O_7$	22.918	14.15		
$Ho_2Ti_2O_7$	22.346	14.802			$Ho_2Hf_2O_7$	21.998	13.639			$Lu_2Ir_2O_7$	22.987	14.29		
$Er_2Ti_2O_7$	22.556	15.502			$Er_2Hf_2O_7$	22.094	13.960			$La_2Ge_2O_7$	22.667	13.64		18.3
$Tm_2Ti_2O_7$	22.615	15.699			$Tm_2Hf_2O_7$	22.183	14.258			$Bi_2Pt_2O_7$	22.105	12.54		
$Yb_2Ti_2O_7$	22.568	15.542			$Yb_2Hf_2O_7$	22.254	14.495			$Bi_2Rh_2O_7$	22.644	13.59		
$Lu_2Ti_2O_7$	22.683	15.925			$Lu_2Hf_2O_7$	22.345	14.799			$Bi_2Os_2O_7$	22.173	12.67		
$Y_2Ti_2O_7$	22.791	16.284			$Y_2Hf_2O_7$	22.319	14.712			$Bi_2Ru_2O_7$	22.560	13.42		
$La_2Zr_2O_7$	20.758	9.454	9.90	8.90, 9.80	$Pr_2Ru_2O_7$	22.055	12.44			$Bi_2Ir_2O_7$	22.465	13.23		
$Ce_2Zr_2O_7$	20.964	10.154			$Nd_2Ru_2O_7$	22.616	12.75			$Bi_2Ti_2O_7$	22.121	12.57		

Hence, it is clear from these results that the proposed empirical model is quite reasonable and can give us full insight for investigation and predicting the elastic properties of these materials.

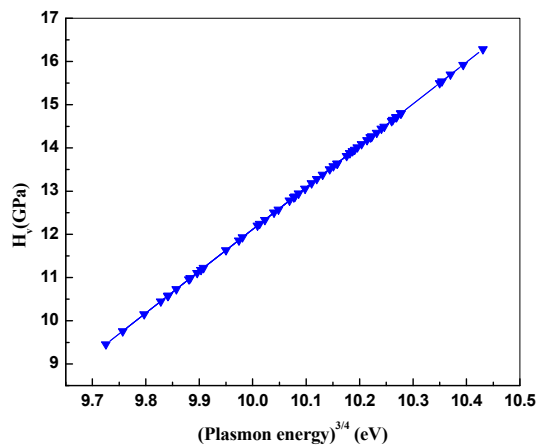


Figure 2.1. Calculated H_v [GPa] versus Plasmon energy for pyrochlore compounds. Vicker's hardness of pyrochlores lies on a straight line and shows increasing trend.

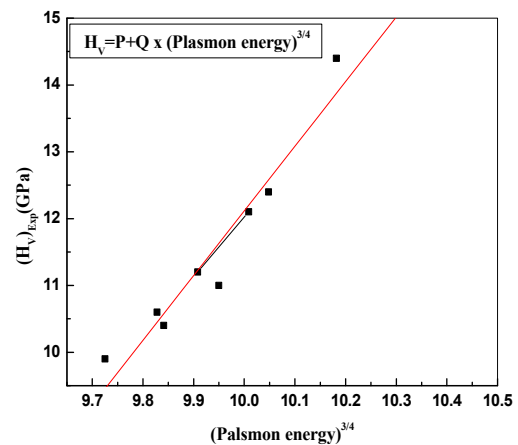


Figure 2.2. Experimental H_v [GPa] versus Plasmon energy for pyrochlore compounds. This straight line exhibits a linear relationship obtained by regression analysis of data. Experimental data are taken from [4, 25].

4. CONCLUSION

According to above results and discussions attained by employing the extended empirical relation, plasma energy of the valence electrons is key parameter for investigating the mechanical/elastic properties of pyrochlore structured solids. In the current investigation, estimates varied somewhat from experimental data by 0.20% to 13.67%. The obtained results express a continuous tendency and are commensurate with the already revealed results reported so far, this confirms the viability of the suggested method. The predicted values of studied compounds are cited in the Table 2. Hence it is clear that such theory can be easily extended to pyrochlore crystals and excellent agreement was found between estimated and the experimental data as compared to other such reported theoretical investigations, previously. In this manner, this model is pioneer in determining the hardness of most of the compounds with the plasmon energy, which assists to determine other crucial properties for technological applications. Furthermore, it is found that in these crystals (investigated), hardness of $A_2B_2O_7$ crystals shows a linear relationship, when plotted against plasma energy of their valence electrons. Hence, it makes sense to state that such empirical model can be easily unfolded to perovskite structured solids to determine their elastic properties; the work on the project is ongoing, and it will be reported in upcoming articles.

CRedit authorship contribution statement:

Rekha Bhati: Investigation, Methodology, Writing- original draft. **Dheerendra Singh Yadav:** Data curation, **Preeti Varshney:** Conceptualization, **Rajesh Chandra Gupta:** Visualization, **Ajay Singh Verma:** Supervision, Writing-review & editing.

ORCID IDs

Rekha Bhati, <https://orcid.org/0000-0001-6046-2192>; Dheerendra Singh Yadav, <https://orcid.org/0000-0001-8315-9743>
Preeti Varshney, <https://orcid.org/0000-0002-6014-7210>; Rajesh Chandra Gupta, <https://orcid.org/0000-0002-0560-7077>
Ajay Singh Verma, <https://orcid.org/0000-0001-8223-7658>

REFERENCES

- [1] S. Singh, A. Bandyopadhyay, "Crystal growth of magnetic pyrochlore oxides and their structure-property correlations", in: *Pyrochlore Ceramics Properties, Processing, and Applications*, edited by A. Chowdhury, 1st edition (Elsevier, 2022). pp. 25.
- [2] A. Raza, A. Afaq, M.S. Kiani, M. Ahmed, A. Bakar, and M. Asif, *J. Mater. Res. Technol.* **18**, 5005 (2022). <https://doi.org/10.1016/j.jmrt.2022.04.111>
- [3] J. Yang, M. Shahid, M. Zhao, J. Feng, C. Wan, and W. Pan, *J. All. Comp.* **663**, 834 (2016). <https://doi.org/10.1016/j.jallcom.2015.12.189>
- [4] J. Feng, B. Xiao, Z.X. Qu, R. Zhou, and W. Pan, *Appl. Phys. Lett.* **99**, 201909 (2011). <https://doi.org/10.1063/1.3659482>
- [5] C. Kaliyaperumal, A. Shankarakumar, J. Palanisamy, and T. Paramasivam, *Mater. Lett.* **228**, 493 (2018). <https://doi.org/10.1016/j.matlet.2018.06.087>
- [6] G.M. Mustafa, S. Atiq, S.K. Abbas, S. Riaz, and S. Naseem, *Ceram. Int.* **44**, 2170 (2018). <https://doi.org/10.1016/j.ceramint.2017.10.172>
- [7] Y. Zhao, N. Li, C. Xu, Y. Li, H. Zhu, P. Zhu, and W. Yang, *Adv. Mater.* **29**, 1701513 (2017). <https://doi.org/10.1002/adma.201701513>
- [8] H. Zhang, K. Haule, and D. Vanderbilt, *Phys. Rev. Lett.* **118**, 026404 (2017). <https://doi.org/10.1103/PhysRevLett.118.026404>
- [9] S. Chen, B. Pan, L. Zeng, S. Luo, X. Wang, and W. Su, *RSC Adv.* **7**, 14186 (2017). <https://doi.org/10.1039/C7RA00765E>
- [10] J.S. Gardner, M.J.P. Gingras, and J. E. Greedan, *Rev. Mod. Phys.* **82**, 53 (2010). <https://doi.org/10.1103/RevModPhys.82.53>
- [11] Y. Jiang, J.R. Smith, and G.R. Odette, et al., *Acta Materialia*, **58**, 1536 (2010). <https://doi.org/10.1016/j.actamat.2009.10.061>
- [12] J. Wu, X. Wei, N.P. Padture, P.G. Klemens, M. Gell, E. Garcia, P. Miranzo, and M.I. Osendi, *Am. Ceram. Soc.* **85**, 3031 (2002). <https://doi.org/10.1111/j.1151-2916.2002.tb00574.x>
- [13] B. Liu, J. Wang, Y. Zhou, T. Liao, and F. Li, *Acta Mater.* **55**, 2949 (2007). <https://doi.org/10.1016/j.actamat.2010.04.031>

- [14] Q. Xu, W. Pan, J. Wang, C. Wan, L. Qi, H. Miao, K. Mori, and T. Torigoe, *J. Am. Ceram. Soc.* **89**, 340 (2006). <https://doi.org/10.1111/j.1551-2916.2005.00667.x>
- [15] F.A. Zhao, H.Y. Xiao, X.M. Bai, Z.J. Liu, and X.T. Zu, *J. Alloys Compounds* **776**, 306 (2019). <https://doi.org/10.1016/j.jallcom.2018.10.240>
- [16] A. Chartier, C. Meis, J.P. Crocombette, L.R. Corrales, and W.J. Weber, *Phys. Rev. B*, **67**, 174102 (2003). <https://doi.org/10.1103/PhysRevB.67.174102>
- [17] C.R. Stanek, R.W. Grimes, and L. Minervini, *Am. Ceram. Soc.* **85**, 2792 (2002). <https://doi.org/10.1111/j.1151-2916.2002.tb00530.x>
- [18] J. Lian, L.M. Wang, S.X. Wang, J. Chen, L.A. Boatner, and R.C. Ewing, *Phys. Rev. Lett.* **87**, 145901 (2001). <https://doi.org/10.1103/PhysRevLett.87.145901>
- [19] M.A. Subramaniam, G. Aravamundan, and G.V.S. Rao, *Oxide Pyrochlores – A Review Progress in Solid State Chem.* **15**, 55 (1983). [https://doi.org/10.1016/0079-6786\(83\)90001-8](https://doi.org/10.1016/0079-6786(83)90001-8)
- [20] X.T. Zu, J. Lian, and R.C. Ewing, *J. Phys. Cond. Matt.* **19**, 346203 (2007). <https://doi.org/10.1088/0953-8984/19/34/346203>
- [21] F. Gao, J. He, E. Wu, S. Liu, D. Yu, D. Li, S. Zhang, and Y. Tian, *Phys. Rev. Lett.* **91**, 015502 (2003). <https://doi.org/10.1103/PhysRevLett.91.015502>
- [22] X. Guo, L. Li, Z. Liu, D. Yu, J. He, R. Liu, B. Xu, et al., *J. Appl. Phys.* **104**, 023503 (2008). <https://doi.org/10.1063/1.2956594>
- [23] S.-H. Jhi, S.G. Louie, M.L. Cohen, and J. Ihm, *Phys. Rev. Lett.* **86**, 3348 (2001). <https://doi.org/10.1103/PhysRevLett.86.3348>
- [24] J. Yang, M. Shahid, M. Zhao, J. Feng, C. Wan, and W. Pan, *J. Alloys Comp.* **663**, 834 (2016). <https://doi.org/10.1016/j.jallcom.2015.12.189>
- [25] J. Feng, B. Xiao, C.L. Wan, Z.X. Qu, Z.C. Huang, J.C. Chen, R. Zhou, and W. Pan, *Acta Mater.* **59**, 1742 (2011). <https://doi.org/10.1016/j.actamat.2010.11.041>
- [26] D.S. Yadav, and S.P. Singh, *Phys. Scr.* **82**, 065705 (2010). <https://doi.org/10.1088/0031-8949/82/06/065705>
- [27] D.S. Yadav, and A.S. Verma, *Int. J. Mod. Phys. B*, **26**, 1250020 (2012). <https://doi.org/10.1142/S0217979212500208>
- [28] D.S. Yadav, *J. Alloys Comp.* **537**, 250 (2012). <https://doi.org/10.1016/j.jallcom.2012.05.016>
- [29] D.S. Yadav, and D.V. Singh, *Phys. Scr.* **85**, 015701 (2012). <https://doi.org/10.1088/0031-8949/85/01/015701>
- [30] D.S. Yadav, *J. Mater. Chem. Phys.* **3**, 6 (2015).
- [31] A.S. Verma, and S.R. Bhardwaj, *Phys. Stat. Sol. (b)* **243**, 2858 (2006). <https://doi.org/10.1002/pssb.200642140>
- [32] R.C. Gupta, A.S. Verma, and K. Singh, *East Eur. J. Phys.* **1**, 80 (2021). <https://doi.org/10.26565/2312-4334-2021-1-10>
- [33] R.C. Gupta, A.S. Verma, and K. Singh, *East Eur. J. Phys.* **1**, 89 (2021). <https://doi.org/10.26565/2312-4334-2021-1-11>
- [34] R.C. Gupta, A.S. Verma, and K. Singh, *J. Taibah Univ. Sci.* **16**, 676 (2022). <https://doi.org/10.1080/16583655.2022.2100687>
- [35] V. Kumar, V. Jha, and A.K. Shrivastava, *Cryst. Res. Technol.* **45**, 920 (2010). <https://doi.org/10.1002/crat.201000268>
- [36] V. Kumar, G.M. Prasad, and D. Chandra, *Phys. Stat. Solidi B*, **170**, 77 (1992). <https://doi.org/10.1002/pssb.2221700108>
- [37] V. Kumar, J.K. Singh, and G.M. Prasad, *Ind. J. Pure Appl. Phys.* **53**, 429 (2015). <http://nopn.niscpr.res.in/handle/123456789/31728>
- [38] A.S. Verma, and S.R. Bhardwaj, *J. Phys. Cond. Mater.* **19**, 026213 (2007). <https://doi.org/10.1088/0953-8984/19/2/026213>

НАПІВЕМПІРИЧНІ ПЕРЕДБАЧЕННЯ ТВЕРДОСТІ РІДКІЗНОЗЕМЕЛЬНИХ ПІРОХЛОРИВ; ДІЕЛЕКТРИКИ З ВИСОКОЮ ПРОНИКНІСТЮ ТА МАТЕРІАЛИ ДЛЯ ТЕРМОЗАХИСНИХ ПОКРИТТІВ

Рекха Бхаті^a, Дірендра Сінгх Ядав^b, Пріті Варшні^c, Раджеш Чандра Гупта^d, Аджай Сінгх Верма^{e,f}

^aДепартамент природничих і прикладних наук, університет Глокал, Сахаранпур-247232 (Індія)

^bФізичний факультет, Чаудхарі Чаран Сінгх коледж післядипломної освіти Хеонра, Етава, 206001 (Індія)

^cФізичний факультет Govt. Girls Inter College, Іглас, Алігарх 202124 (Індія)

^dФізичний факультет, B.S.A. College, Матхура 281004 (Індія)

^eФакультет досліджень та інновацій, Департамент прикладних наук і наук про життя, Університет Уттаранчал, Дехрадун, Уттаракханд (Індія) 284007

^fУніверситетський центр досліджень і розвитку, факультет фізики, Університет Чандігарх, Мохалі, Пенджаб-140413 (Індія)

В роботі сформульована спрощена напівемпірична модель твердості за Віккером рідкоземельних пірохлорних сполук. Ми розглянули $A_2^{3+}B_2^{4+}O_7$ структурованих 97 пірохлорних сполук для розрахунків твердості за Віккером. Енергія плазмону ($\hbar\omega_p$) залежить від основних параметрів матеріалу, таких як N_e -ефективне число вільних електронів на одиницю об'єму, які беруть участь у коливаннях плазми, e -електронний заряд і m -маса електрона. Запропонована модель передбачає, що експериментальні та теоретичні значення твердості за Віккером зростають із збільшенням плазмонної енергії пірохлору. Ми виявили, що розраховані значення краще узгоджуються з наявними експериментальними та теоретичними даними, що підтверджує достовірність моделі. Ця модель підтримує моделювання нових функціональних пірохлорних сполук і допомагає зрозуміти їхні механічні властивості: відмінна термічна стабільність, надпровідність, батареї, сегнетоелектрика, розкидання води, висока іонна провідність, хороша фотолюмінесценція, властиві кисневі вакансії, екзотичний магнетизм і важлива для сьогодення для інкапсуляції ядерних відходів та аерокосмічної промисловості.

Ключові слова: пірохлори; плазмонна енергія; твердість за Віккером

STRUCTURAL, ELECTRICAL AND OPTICAL STUDIES OF $Zn_xCu_{1-x}S$ ($x = 0.8, 0.6, 0.4$ and 0.2) NANOPARTICLES[†]

✉ **Moly M. Rose^{a,*}, R. Sheela Christy^a, T. Asenath Benitta^a, J. Thampi Thanka Kumaran^b**

^aDepartment of Physics and Research Centre (Reg.No.18123112132030), Nesamony Memorial Christian College, Marthandam, Affiliated to Manonmaniam Sundaranar University, Abishekapatti, Tirunelveli, TamilNadu India, 629165

^bDepartment of Physics and Research Centre, Malankara Catholic College, Mariagiri Kaliyakkavilai, Tamilnadu, India 629163

*Corresponding Author e-mail: molyrengith@gmail.com

Received February 3, 2023; accepted February 16, 2023

$Zn_xCu_{1-x}S$ ($x = 0.8, 0.6, 0.4$ and 0.2) nanoparticles were synthesized by microwave assisted chemical precipitation method. The as-synthesized nanoparticles were characterized by X ray diffraction, SEM and TEM analysis to study the crystal structure, size and surface morphology. The energy dispersed x-ray analysis confirms the presence of Zinc, Copper and Sulphur in proper ratio. The D.C. electrical resistance was measured in the temperature range 300K-500K. All the samples show phase transition above a particular temperature. UV, PL and Raman spectra of all the samples were compared and studied.

Keywords: chemical precipitation; structural; electrical; phase transition

PACS: 81.07.-b, 05.70.-a, 81.20.Fw, 61.05.C-, 78.20.-e, 68.37.-d, 81.07.-b, 88.40.H-, 87.64.Ee

1. Introduction

Zinc Sulphide is an important semiconductor material which has been extensively studied because of its physical and chemical properties. ZnS is a wide bandgap semiconductor with a band gap energy of 3.68eV [1,2]. Due to wide band gap, it is useful in optoelectronics [3] and sensors [4]. Zinc Sulphide nanoparticles have potential for various applications in the field of solar cells [5], displays [6], lasers [7] and light emitting diodes, [8] ZnS exist in two phases, i.e's cubic phase and hexagonal phase [9]. Zinc Sulphide nanoparticles have been successfully synthesized by different Methods such as sol-gel [10], sonochemical [11], microwave irradiation [12], microemulsion [13] solvothermal [14] and, hydrothermal [15].

CuS is typical p-type semiconductor that has a direct band gap of 2.5 eV [16-17]. CuS is a potential candidate that could be used in the areas of solar cell elements conversion, gas sensors, IR detectors, electrochemical cells, and photo catalysts [18-22]. The synthesis of copper sulphide has been achieved using different approaches such as microwave irradiation [23], hydrothermal [24], sol-gel [25], microemulsion [26], sonochemical [27], microwave assisted heating [28].

Phase transition in Zinc Sulphide nanoparticles were already studied by varying annealing temperature and pressure, from resistance measurements [29-33]. Phase transition in Copper Sulphide nanoparticles have been studied by previous works [34-35]. $Zn_xCu_{1-x}S$ ($x = 0.8, 0.6, 0.4$ and 0.2) nanoparticles have the application of both Zinc Sulphide nanoparticles and Copper Sulphide nanoparticles. W.Q Peng and G.W Cong investigated the room temperature photoluminescence of (ZnS: Cu) nanoparticles [36]. Jagadeep Kaur and Manoj Sharma studied the structural and optical studies of undoped and copper doped Zinc Sulphide nanoparticles for photocatalytic application [37]. Chanchal Mondal performed ZnS nanoflower promoted evolution of CuS/ZnS p-n heterojunction for exceptional visible light driven photocatalytic activity [38]. S. Harish and J. Archana investigated ultrafast visible light active ZnS/CuS nanostructured photocatalyst [39]. Vijayan et al studied High luminescence efficiency of Copper doped Zinc Sulfide (Cu: ZnS) nanoparticles towards LED applications [40].

In the present study we synthesized $Zn_xCu_{1-x}S$ ($x = 0.8, 0.6, 0.4$ and 0.2) nanoparticles by microwave assisted chemical precipitation method and studied their phase transition through D.C. electrical resistance measurements at various temperatures.

2. Experimental techniques

2.1. Synthesis of $Zn_xCu_{1-x}S$ ($x=0.8, 0.6, 0.4$ and 0.2) nanoparticles by microwave assisted chemical precipitation method

Zinc acetate, Copper acetate and Sodium Sulphide were used for the synthesis of $Zn_xCu_{1-x}S$ ($x = 0.8, 0.6, 0.4$ and 0.2) nanoparticles. Zinc acetate and Copper acetate were taken together in the required composition (1:2 molar ratio) and dissolved in 40 ml distilled water separately and mixed together. The amount of precursor materials taken to dissolve in 80 ml distilled water are given in Table 1. The sodium sulphide solution obtained by dissolving 6.14 gm in 40 ml of distilled water was added in drops to the above solution under effective stirring for 3 hours and kept undisturbed for one day. After performing precipitation, the precipitates were purified out several times, cleaned thoroughly with deionized water several times, and kept in a microwave oven. The solution was then subjected to microwave irradiation of 800 W for 20 minutes. The nanoparticles thus obtained were then brought to room temperature.

[†] Cite as: M.M. Rose, R.S. Christy, T.A. Benitta, and J.T.T. Kumaran, East Eur. J. Phys. 1, 228 (2023), <https://doi.org/10.26565/2312-4334-2023-1-30>
© M.M. Rose, R.S. Christy, T.A. Benitta, J.T.T. Kumaran, 2023

The nanoparticles thus obtained were then cooled to room temperature. Finally, the $Zn_xCu_{1-x}S$ ($x = 0.8, 0.6, 0.4$ and 0.2) nanoparticles were annealed at 100°C for 3 hours to get the phase pure $Zn_xCu_{1-x}S$ ($x = 0.8, 0.6, 0.4$ and 0.2) nanoparticles. The collected nanoparticles were used for different characterization.

Table 1. The amount of precursor materials taken to dissolve in 80 ml distilled water.

Sl no	Expected composition	Zinc acetate	Copper acetate
1	$Zn_{0.8}Cu_{0.2}S$	7.024 gm	1.59 gm
2	$Zn_{0.6}Cu_{0.4}S$	5.26 gm	3.19 gm
3	$Zn_{0.4}Cu_{0.6}S$	3.512 gm	4.79 gm
4	$Zn_{0.2}Cu_{0.8}S$	1.75 gm	6.38 gm

2.2. Instrumentation

X-ray diffraction (XRD) patterns of $Zn_xCu_{1-x}S$ ($x = 0.8, 0.6, 0.4$ and 0.2) nanoparticles were recorded on a powder X-ray diffractometer with Cu $K\alpha$ radiation ($\lambda = 1.54 \text{ \AA}$) with 2θ ranging from angles $10^\circ - 80^\circ$. Surface Morphology of the samples has been studied using TESCAN VEGA3 SBH Scanning Electron Microscope. The elements compositions were confirmed using an energy dispersive X-ray analysis (EDAX) set up attached with scanning electron microscope. A compressed collection of nanoparticles (pellet) was obtained by applying a high pressure of 10 tons/cm^2 . Resistance of the pellet form of the samples were measured using four probe technique. Optical absorption spectra of the synthesized nanoparticles were recorded on UV-visible-spectrometer in the wave length range $200-900 \text{ nm}$. Photoluminescence measurements were performed on Varian Cary Eclipse Photoluminescence spectrophotometer in the range $300-650 \text{ nm}$. Raman spectrum of the $Zn_xCu_{1-x}S$ ($x = 0.8, 0.6, 0.4$ and 0.2) nanoparticles were recorded using peak Seeker Raman spectrometer.

3. Results and discussion

3.1. Structural studies

The indexed XRD patterns of as synthesized $Zn_xCu_{1-x}S$ ($x = 0.8, 0.6, 0.4$ and 0.2) nanoparticles prepared by microwave assisted chemical precipitation method are shown in Fig.1a, 1b, 1c, and 1d respectively. TEM images of all the samples are given in Fig. 2a, 2b, 2c and 2d respectively and it confirms the nanostructures. The respective EDAX images are depicted in Fig. 3a, 3b, 3c and 3d confirms the presence of Zinc, Copper and Sulphur in proper ratio. Samples, structure at room temperature, lattice parameters and particle size of the synthesized samples are given in the Table 2. As the content of Cu increases, the particle size also increases. The XRD patterns of the mixtures show that the mixtures may have the structure of any one of their components (ZnS or CuS).

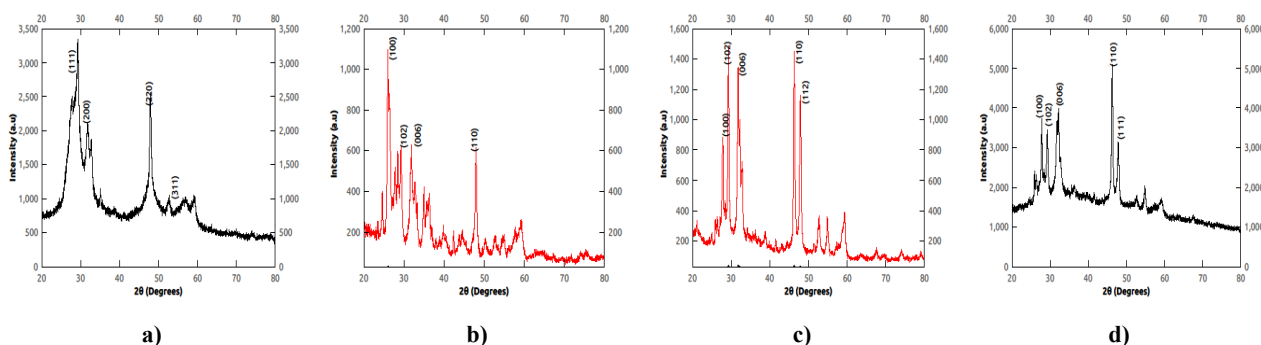
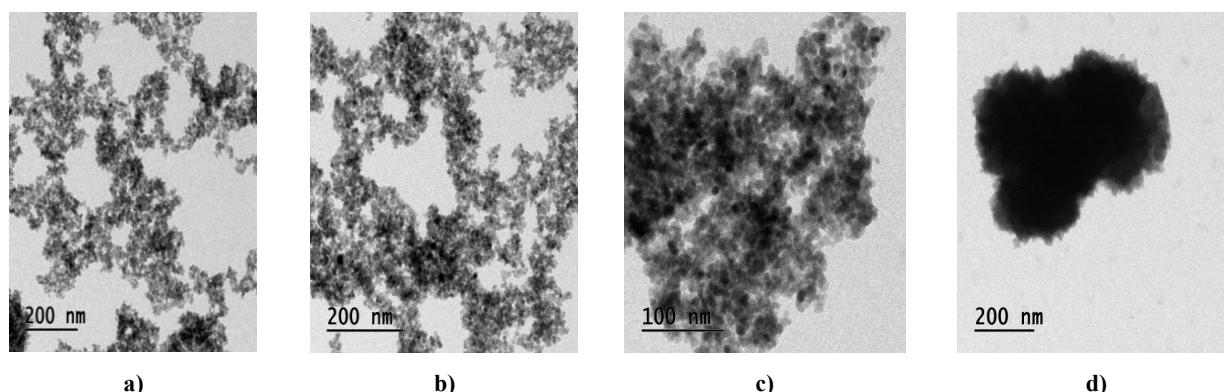


Figure 1. Indexed XRD patterns of nanoparticles

a) $Zn_{0.8}Cu_{0.2}S$ nanoparticles, b) $Zn_{0.6}Cu_{0.4}S$ nanoparticles, c) $Zn_{0.4}Cu_{0.6}S$ nanoparticles, d) $Zn_{0.2}Cu_{0.8}S$ nanoparticles



a)

b)

c)

d)

Figure 2. TEM image of nanoparticles

a) $Zn_{0.8}Cu_{0.2}S$ nanoparticles, b) $Zn_{0.6}Cu_{0.4}S$ nanoparticles, c) $Zn_{0.4}Cu_{0.6}S$ nanoparticles, d) $Zn_{0.2}Cu_{0.8}S$ nanoparticles

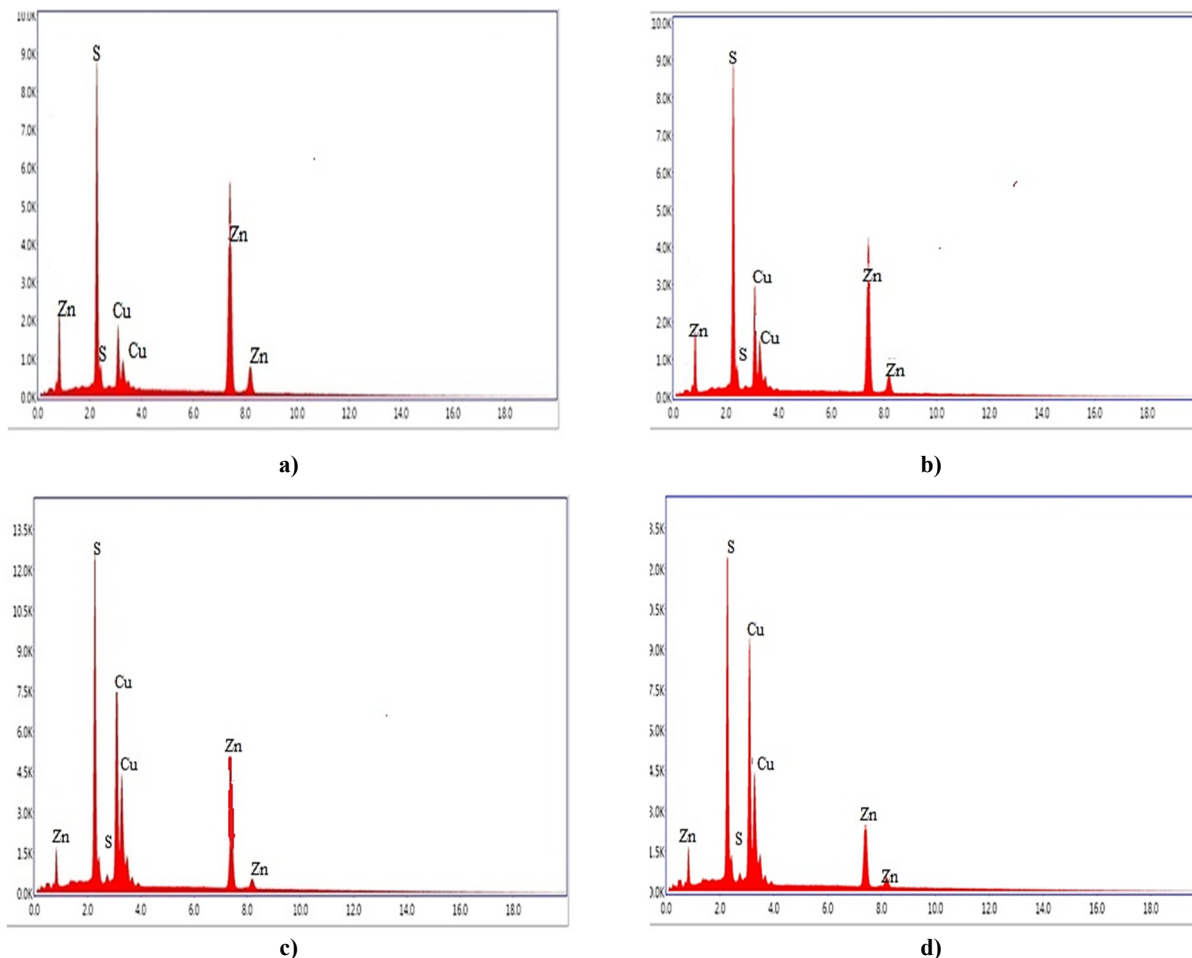


Figure 3. EDAX image of nanoparticles

a) $Zn_{0.8}Cu_{0.2}S$ nanoparticles, b) $Zn_{0.6}Cu_{0.4}S$ nanoparticles, c) $Zn_{0.4}Cu_{0.6}S$ nanoparticles, d) $Zn_{0.2}Cu_{0.8}S$ nanoparticles

Table 2. Samples, structure at room temperature, lattice parameters, particle size of synthesized $Zn_xCu_{1-x}S$ ($x = 0.8, 0.6, 0.4$ and 0.2) nanoparticles

Sl no	Samples	Structure at room temperature	Lattice parameters	Particle size
1	ZnS (reported)	Face centered cubic	$a=b=c=5.4 \text{ \AA}$	
2	$Zn_{0.8}Cu_{0.2}S$	Face centered cubic	$a=b=c=5.2 \text{ \AA}$	31nm
3	$Zn_{0.6}Cu_{0.4}S$	Hexagonal	$a=3.8 \text{ \AA}$ and $c=17 \text{ \AA}$	36nm
4	$Zn_{0.4}Cu_{0.6}S$	Hexagonal	$a=3.9 \text{ \AA}$ and $c=16.8 \text{ \AA}$	39nm
5	$Zn_{0.2}Cu_{0.8}S$	Hexagonal	$a=3.9 \text{ \AA}$ and $c=16.62 \text{ \AA}$	45nm
6	CuS (reported)	Hexagonal	$a=3.8 \text{ \AA}$ and $c=16.4 \text{ \AA}$	

3.2. Electrical Studies

The D.C. electrical resistance of pellet form of the $Zn_xCu_{1-x}S$ ($x=0.8, 0.6, 0.4$ and 0.2) nanoparticles synthesized were measured in the temperature range 300K-500K and is shown in Fig. 4a, 4b, 4c and 4d respectively. A discontinuity is observed in all the samples at a particular temperature due to phase transition [33]. The electrical properties of all the samples also change at this particular temperature. This change in electrical property is due to phase transition [41]. Behaviour of the sample at room temperature, order of resistance at room temperature, possible transition temperatures and behaviour of the sample after phase transition of $Zn_xCu_{1-x}S$ ($x=0.8, 0.6, 0.4, 0.2$) nanoparticles are tabulated in Table 3.

The temperature resistance curve of $Zn_{0.8}Cu_{0.2}S$ nanoparticles (Fig. 4a) remains constant up to 450 K. In this region, the resistance of the sample is of the order of 10^9 Ohms, and the sample behaves as an insulator. Hence it can be utilized for the purpose of withstanding high resistance up to 450 K. As the resistance decreases rapidly with temperature above 450 K it can be used as a temperature sensor.

Fig. 5 shows the order of resistance with variations in the composition of Cu in $Zn_xCu_{1-x}S$ ($x = 0.8, 0.6, 0.4$ and 0.2) nanoparticles. As the composition of Cu in $Zn_xCu_{1-x}S$ ($x = 0.8, 0.6, 0.4$ and 0.2) nanoparticles varies the order of resistance changes from 10^9 to 10^2 Ohms. R. Sheela Christy et al have already reported the rapid decrease in the resistance due to the incorporation of more Cu in CuS-Ag₂S nanoparticle system [42]. From the graph (Fig. 5), as the curve is linear, by varying the composition, the sample can be synthesised with the desired order of resistance for a particular purpose.

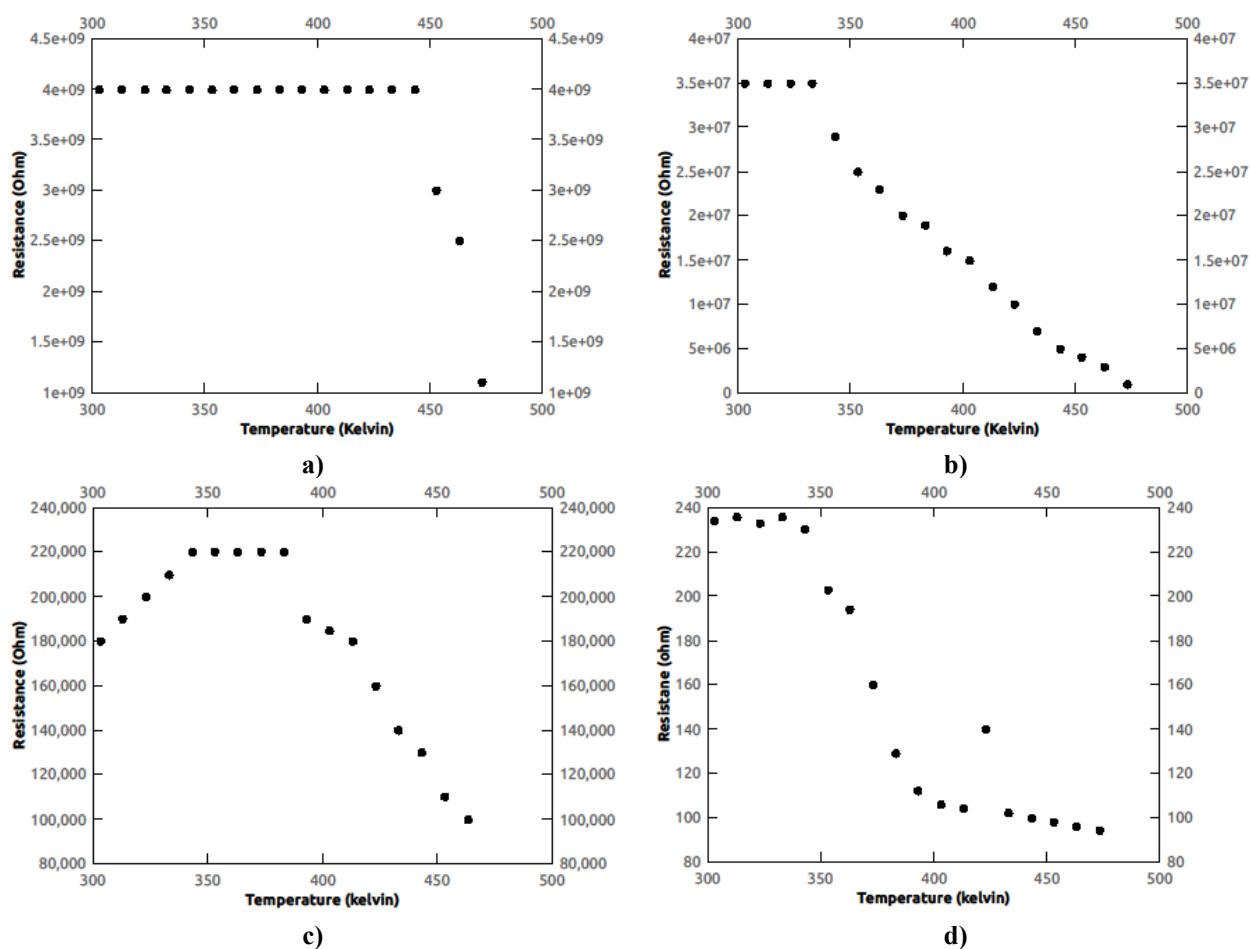


Figure 4. Temperature resistance curve of nanoparticles

a) $Zn_{0.8}Cu_{0.2}S$ nanoparticles, b) $Zn_{0.6}Cu_{0.4}S$ nanoparticles, c) $Zn_{0.4}Cu_{0.6}S$ nanoparticles, d) $Zn_{0.2}Cu_{0.8}S$ nanoparticles

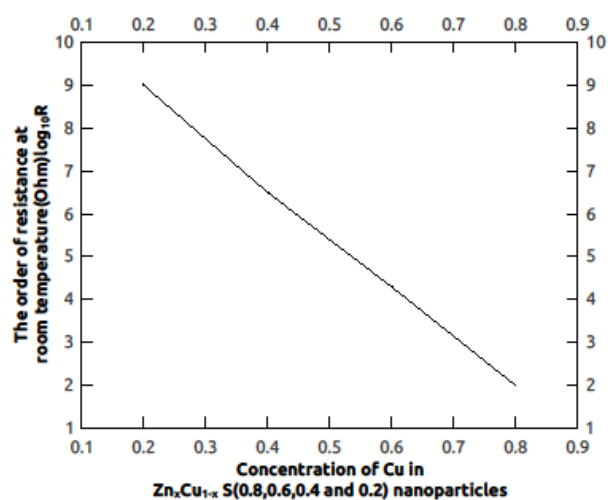


Figure 5. The variation of order of resistance with the composition of Cu in $Zn_xCu_{1-x}S$ ($x=0.8, 0.6, 0.4$ and 0.2) nanoparticles

Table 3. Behaviour of the sample at room temperature, order of resistance at room temperature, possible transition temperatures and behaviour of the sample after phase transition of $Zn_xCu_{1-x}S$ ($x = 0.8, 0.6, 0.4$ and 0.2) nanoparticles

Samples	Behaviour of the sample at room temperature	Order of resistance at room temperature	Possible transition temperatures	Behaviour of the sample after phase transition
$Zn_{0.8}Cu_{0.2}S$	Insulator	$10^9 \Omega$	440K	Semiconductor
$Zn_{0.6}Cu_{0.4}S$	Insulator	$10^7 \Omega$	340K	Semiconductor
$Zn_{0.4}Cu_{0.6}S$	Conductor	$10^5 \Omega$	340K	Semiconductor
$Zn_{0.2}Cu_{0.8}S$	Oscillation	$10^2 \Omega$	340K	Semiconductor

3.3. Optical studies

Fig. 6 shows the optical absorption spectra of $Zn_xCu_{1-x}S$ ($x = 0.8, 0.6, 0.4$ and 0.2) nanoparticles synthesised by microwave-assisted chemical precipitation method. From the absorption spectroscopy, it's clear that when more and more Cu is incorporated, the absorption edge gets shifted towards the lower wavelength region and the percentage of absorption also decreases. The samples can be synthesised with the desired absorption edge and percentage of absorption by varying the composition of Cu in the mixture for different applications.

Fig. 7 depicts the PL emission spectra of $Zn_xCu_{1-x}S$ ($x = 0.8, 0.6, 0.4$ and 0.2) nanoparticles synthesised by microwave-assisted chemical precipitation method. When more Cu is incorporated, the emission peaks shift from 390 nm to 370 nm. Fig. 8 depicts the variation of emission peak with composition of Cu in $Zn_xCu_{1-x}S$ ($x = 0.8, 0.6, 0.4$ and 0.2). Because this variation is linear, $Zn_xCu_{1-x}S$ ($x = 0.8, 0.6, 0.4$ and 0.2) nanoparticles can be tuned to emit different wavelengths in the range 390 nm – 370 nm by varying the composition of Cu, and the sample composition can also be identified from the graph by observing the emission peak.

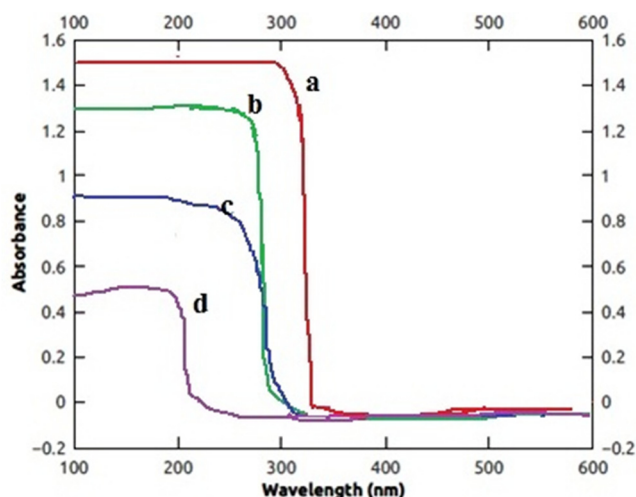


Figure 6. Optical absorption spectrum of nanoparticles
a) $Zn_{0.8}Cu_{0.2}S$ nanoparticles, b) $Zn_{0.6}Cu_{0.4}S$ nanoparticles,
c) $Zn_{0.4}Cu_{0.6}S$ nanoparticles, d) $Zn_{0.2}Cu_{0.8}S$ nanoparticles

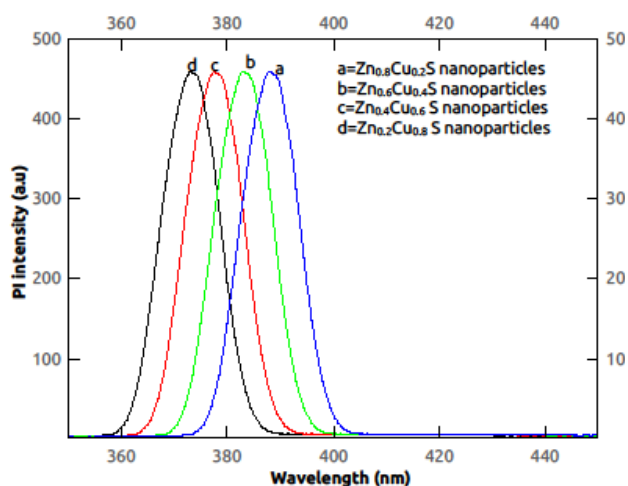


Figure 7. Emission spectra of $Zn_xCu_{1-x}S$ nanoparticles
($x = 0.8, 0.6, 0.4$ and 0.2)

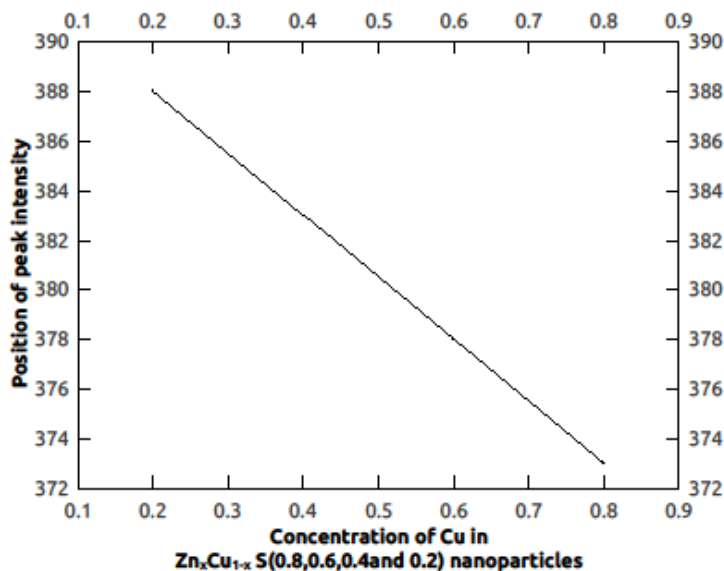


Figure 8. The plot for the variation of emission peak with the composition of Cu in $Zn_xCu_{1-x}S$ ($x = 0.8, 0.6, 0.4$ and 0.2) nanoparticles synthesized by microwave assisted chemical precipitation method

3.4. Raman studies

Figures 9 a-d show the Raman spectra of $Zn_xCu_{1-x}S$ ($x = 0.8, 0.6, 0.4$ and 0.2) nanoparticles synthesised via microwave-assisted chemical precipitation method. The peaks are centered around 340 cm^{-1} and 400 cm^{-1} . When more Cu is incorporated, the intensity of the peaks keeps decreasing. The peak around 290 cm^{-1} was attributed to Cu-S bond vibration [43], and the peak around 400 cm^{-1} was attributed to Zn-S bond vibration [44].

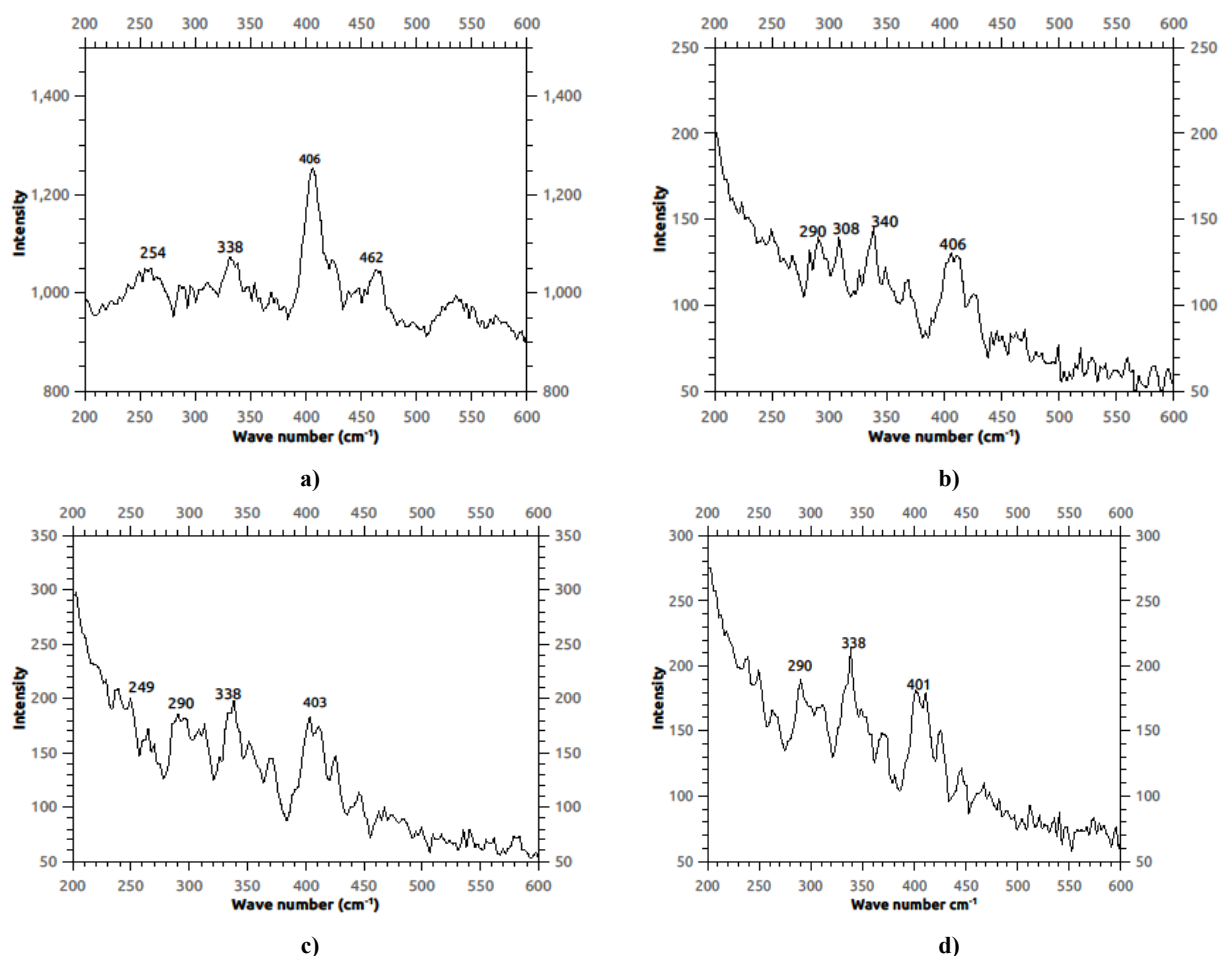


Figure 9. Raman spectrum of nanoparticles

a) $Zn_{0.8}Cu_{0.2}S$ nanoparticles, b) $Zn_{0.6}Cu_{0.4}S$ nanoparticles, c) $Zn_{0.4}Cu_{0.6}S$ nanoparticles, d) of $Zn_{0.2}Cu_{0.8}S$ nanoparticles

4. CONCLUSION

$Zn_xCu_{1-x}S$ ($x = 0.8, 0.6, 0.4$ and 0.2) nanoparticles were synthesised by the microwave-assisted chemical precipitation method. The XRD patterns of the mixtures show that the mixtures may have the structure of any one of their components (ZnS or CuS). The electrical studies show that all the samples undergo phase transition above a particular temperature. Starting with $Zn_{0.8}Cu_{0.2}S$ nanoparticles, the electrical resistance of the samples is rapidly reduced as more and more Cu is incorporated. From the absorption spectroscopy, it's clear that as more and more Cu is incorporated, the absorption edge gets blue-shifted. By varying the composition of Cu , the mixture can be tuned to emit different wavelengths in the range of 390 nm to 370 nm. The peaks of both ZnS and CuS are present in the Raman spectra of the $Zn_xCu_{1-x}S$ ($x = 0.8, 0.6, 0.4$ and 0.2) nanoparticles.

Acknowledgements

The authors gratefully acknowledge Nesamony Memorial Christian College, Marthandam, for providing the necessary laboratory facilities to carry out this work.

Funding. This study was done towards the Ph.D. work of Mrs. Moly M Rose and was not funded by any external agencies.

Competing Interests. We have not received any funding from any company or university, and hence, there is no conflict of interest.

Author Contributions. All authors discussed the results and contributed to the final manuscript.

Data availability statement. The data that support the findings of this study are available within the article

ORCID IDs

©Moly M. Rose, <https://orcid.org/0000-0003-4840-0567>

REFERENCES

- [1] X.D. Gao, X.M. Li, and W.D. Yu, "Morphology and optical properties of amorphous ZnS films deposited by ultrasonic-assisted successive ionic layer adsorption and reaction method", *Thin Solid Films*, **468**, 43 (2004). <https://doi.org/10.1016/j.tsf.2004.04.005>
- [2] I. Parvaneh, S. Samira, and N. Mohsen, "Characterization of ZnS nanoparticles synthesized by co-precipitation method", *Chinese Physics B*, **24**(4), 046104 (2015). <https://doi.org/10.1088/1674-1056/24/4/046104>

- [3] U.P. Onochie, S.C. Ikpeseni, A.E. Igweoko, H.I. Owamah, C.C. Aluma, and C. Augustine, "Optical Properties of Zinc Sulphide Thin Films Coated with Aqueous Organic Dye Extract for Solar and Optoelectronic Device Applications", *Journal of Electronic Materials*, **50**, 2576 (2021). <https://doi.org/10.1007/s11664-021-08792-0>
- [4] S.K. Mehta, Khushboo, and A. Umar, "Highly sensitive hydrazine chemical sensor based on mono-dispersed rapidly synthesized PEG-coated ZnS nanoparticles", *Talanta*, **85**(5), 2411 (2011). <https://doi.org/10.1016/j.talanta.2011.07.089>
- [5] M. Ragam, N. Sankar, and K. Ramachandran, "Investigation on Zinc Sulphide Nanoparticles in Dye Sensitized Solar Cell", *AIP Conference Proceedings*, **1349**, 411 (2011). <https://doi.org/10.1063/1.3605909>
- [6] H. Ali, S. Karim, M.A. Rafiq, K. Maaz, A.U. Rahman, A. Nisar, and M. Ahmad, "Electrical conduction mechanism in ZnS nanoparticles", *J. Alloys Compd.* **612**, 64 (2014). <https://doi.org/10.1016/j.jallcom.2014.05.163>
- [7] M. Jayalakshmi, and M.M. Rao, "Synthesis of zinc sulphide nanoparticles by thiourea hydrolysis and their characterization for electrochemical capacitor applications", *Journal of Power Sources*, **157**(1), 624 (2006). <https://doi.org/10.1016/j.jpowsour.2005.08.001>
- [8] S. Vijayan, G. Umadevi, R. Mariappan, M. Narayanan, B. Narayanamoorthy, and S. Kandasamy, "High luminescence efficiency of Copper doped Zinc Sulfide (Cu: ZnS) nanoparticles towards LED applications", *Materials Today: Proceedings*, (2020). <https://doi.org/10.1016/j.matpr.2020.11.214>
- [9] T.T.Q. Hoa, L.V. Vu, T.D. Canh, and N.N. Long, "Preparation of ZnS nanoparticles by hydrothermal method", *Journal of Physics: Conference Series*, **187**, 012081 (2009). <https://doi.org/10.1088/1742-6596/187/1/012081>
- [10] L. Kashinath, K. Namratha, S. Srikantaswamy, A. Vinu, and K. Byrappa, "Microwave treated sol-gel synthesis and characterization of hybrid ZnS-RGO composites for efficient photodegradation of dyes", *New J. Chem.* **41**, 1723 (2017). <https://doi.org/10.1039/C6NJ03716J>
- [11] J.-R. Li, J.-F. Huang, L.-Y. Cao, J.-P. Wu, and H.-Y. He, "Synthesis and kinetics research of ZnS nanoparticles prepared by sonochemical process", *Material science and Technology*, **26**, 1269 (2013). <https://doi.org/10.1179/026708309X12495548508428>
- [12] S. Thangavel, K. Krishnamoorthy, S.-J. Kim, and G. Venugopal, "Designing ZnS decorated reduced graphene-oxide nanohybrid via microwave route and their application in photocatalysis", *Journal of Alloys and Compounds*, **683**, 456 (2016). <https://doi.org/10.1016/j.jallcom.2016.05.089>
- [13] T. Charinpanitkul, A. Chanagul, J. Dutta, U. Rungsardthong, and W. Tanthapanichakoon, "Effects of cosurfactant on ZnS nanoparticle synthesis in microemulsion", *Science and Technology of Advanced Materials*, **6**, 266 (2005). <https://doi.org/10.1016/j.stam.2005.02.005>
- [14] F.A. La Porta, M.M. Ferrer, Y.V.B. Santana, C.W. Raubach, V.M. Longo, J.R. Sambrano, E. Longo, et al., "Synthesis of wurtzite ZnS nanoparticles using the microwave assisted solvothermal method", *Journal of Alloys and Compounds*, **556**, 153 (2013). <http://dx.doi.org/10.1016/j.jallcom.2012.12.081>
- [15] T.T.Q. Hoa, L.V. Vu, T.D. Canh, and N.N. Long, "Preparation of ZnS nanoparticles by hydrothermal method", *IOP Publishing Journal of Physics, Conference Series*, **187**, 012081 (2009). <https://doi.org/10.1088/1742-6596/187/1/012081>
- [16] I. Puspitasari, T.P. Gujar, K.-D. Jung, and, O.-S. Joo, "Simple chemical preparation of CuS nanowhiskers", *Materials Science and Engineering B*, **140**, 199 (2007). <https://doi.org/10.1016/j.mseb.2007.04.012>
- [17] F. Ghribi, A. Alyamani, Z.B. Ayadi, K. Djessas, L. ELMir, "Study of CuS Thin Films for Solar Cell Applications Sputtered from Nanoparticles Synthesised by Hydrothermal Route", *Energy Procedia*, **84**, 197203 (2015). <https://doi.org/10.1016/j.egypro.2015.12.314>
- [18] H. Wang, Y. Sun, W. Yue, Q. Kang, H. Li, and D. Shen, "A smartphone-based double-channel fluorescence setup for immunoassay of a carcinoembryonic antigen using CuS nanoparticles for signal amplification", *Analyst*, **143**, 1670 (2018). <https://doi.org/10.1039/C7AN01988B>
- [19] M.P. Ravele, O.A. Oyewo, and D.C. Onwudiwe, "Controlled Synthesis of CuS and Cu₉S₅ and Their Application in the Photocatalytic Mineralization of Tetracycline", *Catalysts*, **11**, 899 (2021). <https://doi.org/10.3390/catal11080899>
- [20] D. Ayodhya, and G. Veerabhadram, "Investigation of temperature and frequency dependence of electrical conductivity and dielectric behavior in CuS and rGO capped CuS nanocomposites", *Mater. Res. Express*, **6**, 045910 (2019). <https://doi.org/10.1088/2053-1591/aaf555>
- [21] Z. Zha, S. Zhang, Z. Deng, Y. Li, C. Lia, and Z. Dai, "Enzyme-Responsive Copper Sulphide Nanoparticles for Combined Photoacoustic Imaging", *Chem. Commun.* **49**, 3455 (2013). <https://doi.org/10.1039/C3CC40608C>
- [22] S. Goel, F. Chen, and W. Cai, "Synthesis and Biomedical Applications of Copper Sulfide Nanoparticles: From Sensors to Theranostics", *Nano Micro Small*, **10**(4), 631 (2014). <https://doi.org/10.1002/sml.201301174>
- [23] M. Nafees, S. Ali, S. Idrees, K. Rashid, M.A. Shafique, "A simple microwave assisted aqueous route to synthesis CuS nanoparticles and further aggregation to spherical shape", *Applied Nanoscience*, **3**, 119 (2013). <https://doi.org/10.1007/s13204-012-0113-9>
- [24] M. Saranya, C. Santhosh, R. Ramachandran, and A.N. Grace, "Growth of CuS Nanostructures by Hydrothermal Route and Its Optical Properties", *Journal of Nanotechnology*, **2014**, 321571 (2014). <https://doi.org/10.1155/2014/321571>
- [25] S. Riyaz, A. Parveen, and A. Azam, "Microstructural and optical properties of CuS nanoparticles prepared by sol-gel route", *Perspectives in Science*, **8**, 632 (2016). <https://doi.org/10.1016/j.pisc.2016.06.041>
- [26] J.N. Solanki, R. Sengupta, Z.V.P. Murthy, "Synthesis of copper sulphide and copper nanoparticles with microemulsion method", *Solid State Sciences*, **12**(9), 1560 (2010). <https://doi.org/10.1016/j.solidstatesciences.2010.06.021>
- [27] A.S.R. Manivannan, and S.N. Victoria, "Simple one-pot sonochemical synthesis of copper sulphide nanoparticles for solar cell applications", *Arabian Journal of Chemistry*, **12**(8), 2439 (2019). <https://doi.org/10.1016/j.arabjc.2015.03.013>
- [28] X.-H. Liao, N.-Y. Chen, S. Xu, S.-B. Yang, J.-J. Zhu, "A microwave assisted heating method for the preparation of copper sulfide nanorod", *Journal of Crystal Growth*, **252**(4), 593 (2003). [https://doi.org/10.1016/S0022-0248\(03\)01030-3](https://doi.org/10.1016/S0022-0248(03)01030-3)
- [29] A.K. Kole, and P. Kumbhakar, "Cubic-to-hexagonal phase transition and optical properties of chemically synthesized ZnS nanocrystals", *Results in Physics*, **2**, 150 (2012). <http://dx.doi.org/10.1016/j.rinp.2012.09>
- [30] J. Kennedy, P.P. Murmu, P.S. Gupta, D.A. Carder, S.V. Chong, J. Leveneur, and S. Rubanov, "Effects of annealing on the structural and optical properties of zinc sulfide thin films deposited by ion beam sputtering", *Materials Science in Semiconductor Processing* **26**, 561 (2014). <http://dx.doi.org/10.1016/j.mssp.2014.05.055>

- [31] Y. Li, W. Tan, and Y. Wu, "Phase Transition between Sphalerite and Wurtzite in ZnS", *Optical Ceramic Materials*, 40(5), 2130 (2020). <https://doi.org/10.1016/j.jeurceramsoc.2019.12.045>
- [32] C. Yang, Y. Liu, H. Sun, D. Guo, X. Li, W. Li, B. Liu, and X. Zhang, "Pressure-induced transition-temperature reduction in ZnS nanoparticles", *Nanotechnology*, 19, 095704 (2008). <https://doi.org/10.1088/0957-4484/19/9/095704>
- [33] M.M. Rose, R.S. Christy, T.A. Benitta, J.T.T. Kumaran, and M.R. Bindhu, "Phase transition in ZnS nanoparticles: electrical, thermal, structural, optical, morphological, antibacterial and photocatalytic properties", *Chalcogenide Letters*, 19(11), 855 (2022). <https://doi.org/10.15251/CL.2022.1911.855>
- [34] P.V. Quintana-Ramirez, Ma.C. Arenas-Arrocena, J.Santos-Cruz, M. Vega-González, O. Martínez-Alvarez, V.M. Castaño-Meneses, L.S. Acosta-Torres, and J. de la Fuente-Hernández, "Growth evolution and phase transition from chalcocite to digenite in nanocrystalline copper sulfide: Morphological, optical and electrical properties", *Beilstein J. Nanotechnol.* 5, 1542 (2014). <https://doi.org/10.3762/bjnano.5.166>
- [35] A. Narjis, A. Outzourhit, A. Aberkouks, M. El Hasnaoui, and L. Nkhaili, "Structural and thermoelectric properties of copper sulphide powders", *Journal of Semiconductors*, 39(12), (2018). <https://doi.org/10.1088/1674-4926/39/12/122001>
- [36] W.Q. Peng, G.W. Cong, S.C. Qu, and Z.G. Wang, "Synthesis and photoluminescence of ZnS:Cu nanoparticles", *Optical Materials* 29, 313 (2006). <https://doi.org/10.1016/j.optmat.2005.10.003>
- [37] J. Kaur, M. Sharma, and O.P. Pandey, "Structural and optical studies of undoped and copper doped zinc sulphide nanoparticles for photocatalytic application", *Superlattices and Microstructures*, 77, 35 (2015). <https://dx.doi.org/10.1016/j.spmi.2014.10.032>
- [38] C. Mondal, A. Singh, R. Sahoo, A.K. Sasmal, Y. Negishib, and T. Pal, "Preformed ZnS nanoflower prompted evolution of CuS/ZnS p-n heterojunctions for exceptional visible-light driven photocatalytic activity", *Royal society for chemistry, New J. Chem.* 39, 5628 (2015). <https://doi.org/10.1039/c5nj00128e>
- [39] S. Harish, J. Archana, M. Navaneethan, S.P.A. Singh, V. Gupta, D.K. Aswal, H. Ikeda, and Y. Hayakawa, "Synergetic effect of CuS@ZnS nanostructures on photocatalytic degradation of organic pollutant under visible light irradiation", *RSC Adv.* 7, 34366 (2017). <https://doi.org/10.1039/c7ra04250g>
- [40] S. Vijayan, G. Umadevi, R. Mariappan, M. Narayanan, B. Narayanamoorthy, and S. Kandasamy, "High luminescence efficiency of Copper doped Zinc Sulfide (Cu: ZnS) nanoparticles towards LED applications", *Materials Today: Proceedings*, (2020). <https://doi.org/10.1016/j.matpr.2020.11.214>
- [41] R.S. Christy, and J.T. Thankakumaran, "Phase transition in CuS nanoparticles", *Journal of Non-Oxide Glasses*, 6(1), 13 (2016). https://chalcogen.ro/13_Sheela.pdf
- [42] R.S. Christy, J.T. Thankakumaran, and C. Bansal, "Jump in Band Gap Energy of Ag₂S Nanoparticles Synthesised by Solvothermal Method", *Advanced science focus*, 2(2), 115 (2014). <https://doi.org/10.1166/asfo.2014.1087>
- [43] T. Hurma, and S. Kose, "XRD Raman analysis and optical properties of CuS nanostructured film", *Optik - International Journal for Light and Electron Optics*, 127(15), 6000 (2006). <https://doi.org/10.1016/j.ijleo.2016.04.019>
- [44] S.S. Kumar, M.A. Khadar, S.K. Dhara, T.R. Ravindran, and K.G.M. Nair, "Photoluminescence and Raman studies of ZnS nanoparticles implanted with Cu⁺ ions", *Nuclear Instruments and Methods in Physics Research B*, 251, 435 (2006). <https://doi.org/10.1016/j.nimb.2006.07.002>

СТРУКТУРНІ, ЕЛЕКТРИЧНІ ТА ОПТИЧНІ ДОСЛІДЖЕННЯ НАНОЧАСТИНОК $Zn_xCu_{1-x}S$ ($x = 0,8, 0,6, 0,4$ та $0,2$)

Моли М. Роуз^а, Р. Шила Крісті^а, Т. Асенат Бенітта^а, Дж. Тампі Танка Кумаран^б

^аДепартамент фізики та науково-дослідний центр (реєстр. № 18123112132030), Меморіальний християнський коледж Несамоні, Мартандам, філія університету Манонманіам Сундаранар

Абішекапатті, Тірунелвелі, Таміл Наду, Індія, 629165

^бДепартамент фізики та науково-дослідний центр, Католицький коледж Маланкара,

Маріагірі Каліяккавілай, Тамілнаду, Індія 629163

Наночастинки $Zn_xCu_{1-x}S$ ($x = 0,8, 0,6, 0,4$ і $0,2$) були синтезовані методом хімічного осадження за допомогою мікрохвиль. Синтезовані наночастинки були охарактеризовані за допомогою дифракції рентгенівських променів, SEM та TEM аналізу для вивчення кристалічної структури, розміру та морфології поверхні. Енергодисперсний рентгенівський аналіз підтверджує наявність цинку, міді та сірки в правильному співвідношенні. Електричний опір постійному струму вимірювали в діапазоні температур 300-500 К. Усі зразки демонструють фазовий перехід вище певної температури. УФ, ФЛ та спектри комбінаційного розсіювання всіх зразків були порівняні та досліджені.

Ключові слова: хімічне осадження; структурний; електричні; фазовий перехід

INTERACTIONS OF FIBRILLAR PROTEINS WITH LIPIDS: A MOLECULAR DOCKING INSIGHT[†]

Valeriya Trusova*, Uliana Tarabara, Olga Zhytniakivska,
Kateryna Vus, Galyna Gorbenko

Department of Medical Physics and Biomedical Nanotechnologies, V.N. Karazin Kharkiv National University
4 Svobody Sq., Kharkiv, 61022, Ukraine

*Corresponding Author: valeriya.trusova@karazin.ua

Received January 9, 2023, revised February 11, 2023; accepted February 13, 2023

The aggregation of misfolded proteins into specific ordered aggregates, amyloid fibrils, associated with more than forty human diseases, currently attracts great research attention in biomedical and nanotechnological aspects. These aggregates and their oligomeric intermediates are thought to exert their toxic action predominantly at the level of cell membranes. In addition, membrane lipids were found in many amyloid deposits *in vivo* suggesting that lipid molecules are able to incorporate into fibril structure affecting their morphology and mechanical properties. However, the biological implications and structural prerequisites of fibril-lipid interactions still remain unclear. In the present study the molecular docking techniques was employed to explore the interactions between the amyloid fibrils and lipids in the model systems containing the fibrillar forms of lysozyme, insulin, A β (1-42) peptide and N-terminal (1-83) fragment of apolipoprotein A-I, as a protein component and cholesterol, cardiolipin or phosphatidylcholine as a lipid component. Using the PatchDock web server and BIOVIA Discovery Studio software, the structural peculiarities of fibril-lipid associates were uncovered. The van der Waals and alkyl/ π -alkyl interactions were found to prevail in stabilization of all types of fibril-lipid complexes. The analysis of most energetically favorable docking positions revealed a preferable surface location of lipids and partial penetration of acyl chains of cardiolipin and phosphatidylcholine into fibril grooves.

Keywords: amyloid fibrils; lysozyme; insulin; A β (1-42) peptide; apolipoprotein A-I; fibril-lipid complex; molecular docking

PACS: 87.14.C++c, 87.16.Dg

Among a variety of conformational and aggregational states of polypeptide chain the states of amyloid fibrils and their oligomeric precursors are currently regarded as the most dangerous, since they are associated with more than forty of human diseases [1,2]. The amyloid-related cytotoxicity is thought to be primarily determined by the impairment of cell membrane integrity through either detergent-like mechanism of membrane damage (lipid extraction from the bilayer) [3-7] or membrane permeation for ions via the formation of pore-like structures [8-10]. Moreover, it is becoming increasingly apparent that lipids are an integral part of most fibrillar deposits formed *in vivo* or amyloid fibrils grown *in vitro* in the presence of lipids [11]. The analysis of lipids extracted from various deposits of amyloid fibrils by high-performance thin layer chromatography and mass spectrometry revealed that they may contain more than 10 % of lipid (by dry weight), with major lipid constituents such as cholesterol and sphingomyelin, and minor fraction of sulfatides, cholesterol esters and fatty acids [12]. In the paired helical filaments of tau protein formed in Alzheimer disease the bound lipids were represented by the galactocerebrosides and phosphatidylcholines [13]. It is hypothesized that the presence of lipids as an integral part of many amyloid deposits *in vivo*, is fundamental for biological activity of fibrillized proteins and is essential for the nucleation, morphology, and mechanical properties of fibrils [11]. In the onset of amyloid formation the protein-lipid interactions can favor fibril nucleation, but the lipid uptake is limited to the transfer of a fatty acyl group to serine or lysine residues [14], or transfer of a reactive aldehyde fragment produced by oxidative damage to a lipid [15]. Lipids are most likely to associate with amyloid assembly at the stages of protein oligomerization and protofilament formation [1]. Despite extensive studies of amyloid cytotoxicity, the mechanisms by which lipids may become incorporated into fibril structure still remain poorly understood. In view of this, the aim of the present study was to elucidate the molecular details of fibril-lipid interactions. The molecular docking technique was employed to explore the complex formation in the systems containing the model fibrils of lysozyme, insulin, A β (1-42) peptide and N-terminal (1-83) fragment of apolipoprotein A-I as a protein component and cholesterol, cardiolipin or phosphatidylcholine as a lipid one.

METHODS

To predict the most favorable modes of interactions between the amyloid fibrils and lipids, the molecular docking was performed using the PatchDock algorithm built upon a geometry-based shape complementarity principle. The implementation of this algorithm involves the segmentation of molecular shape into patches of different geometry; matching of these patches and evaluation of the docking positions by geometric shape complementarity fit and atomic desolvation energy scoring function [20]. The model amyloid fibrils of hen egg white lysozyme, A β and apolipoprotein A-I were constructed using the CreateFibril tool based on the translational and rotational affine transformations providing

[†] Cite as: V. Trusova, U. Tarabara, O. Zhytniakivska, K. Vus, and G. Gorbenko, East Eur. J. Phys. 1, 236 (2023), <https://doi.org/10.26565/2312-4334-2023-1-31>

© V. Trusova, U. Tarabara, O. Zhytniakivska, K. Vus, G. Gorbenko, 2023

several copies of a certain fragment of fibril core, whose subsequent stacking produces the elongated fibrillar aggregate [21]. To this end, the following amino acid sequences from fibril core were used: i) K-peptide of lysozyme, GILQINSRW, residues 54-62 of wild-type protein (LzF); ii) the 24-50 fragment from G26R-mutated apolipoprotein A-I, DSRDYVSQFEGSALGKQLNLKLLDNW (apoA); iii) the 1-42 fragment from A β protein, LVFFAEDVGSNKGAIIGLMVGGVVIA (A β). The input structures for CreateFibril were generated from the monomers in the β -strand conformation with PatchDock (LzF, apoA) or were obtained from the Protein Data Bank (A β tetramer, PDB code 2BEG). The twisting angle was taken as 15°, the value recovered previously for the most stable conformations of fibrillar LzF, A β and apoA. The selected docking poses were visualized with the UCSF Chimera software (version 1.14) and analyzed with BIOVIA Discovery Studio Visualizer, v21.1.0.20298, San Diego: Dassault Systemes; 2021. The prominent binding sites were also predicted through the DoGSiteScorer server (<https://proteins.plus/2ozr#dogsitesite>).

RESULTS AND DISCUSSION

While analyzing the predictions of PatchDock tool, the fibril-lipid binding modes were ranked according to the global binding energy (GBE), so that the complexes with the lowest binding energy were selected for deeper evaluation (Fig. 1). Further analysis of the docked structures was focused on the following characteristics: i) the location of lipid binding sites on/within amyloid fibril and interacting amino acid residues; ii) the types of interactions accounting for stabilization of the most energetically favorable amyloid-lipid complexes; iii) the atomic contact energy (ACE).

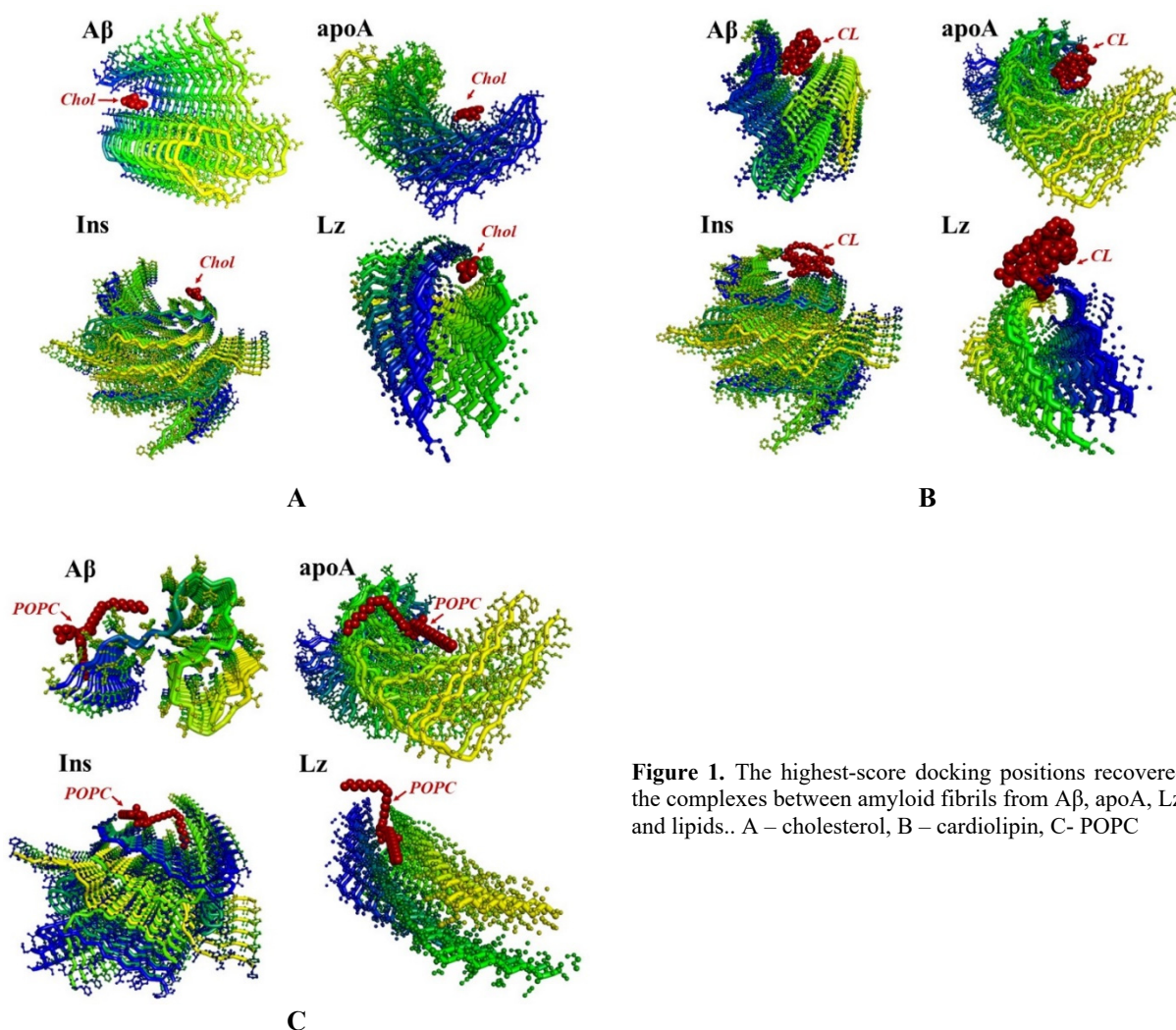


Figure 1. The highest-score docking positions recovered for the complexes between amyloid fibrils from A β , apoA, Lz, Ins and lipids.. A – cholesterol, B – cardiolipin, C- POPC

As seen in Table 1, the global energy of lipid-fibril binding falls in the range from -69.25 to -7.26 kcal/mol. It was found that for all examined systems the values of GBE decrease in the row Chol \rightarrow CL \rightarrow POPC, indicating that the neutral phospholipid POPC forms the most stable complexes with fibrillar proteins. Remarkably, analogous tendencies were revealed also for atomic contact energies, i.e., the lowest ACE values were observed for POPC, while the highest – for Chol.

For all fibrillar proteins under consideration cholesterol was found to display some penetration into the amyloid grooves with the shallowest location of sterol being observed for the lysozyme fibrils (Fig. 1, A). Furthermore, as follows from the Discovery Studio analysis, all amyloid-cholesterol complexes are stabilized by van der Waals and alkyl/ π -alkyl

interactions. Specifically, Chol participates in the strong alkyl/ π -alkyl interactions with His, Leu, Ile amino acid residues of A β amyloid fibrils, Tyr of Ins fibrils and Leu of fibrillar Lz. In turn, van der Waals protein-sterol contacts are ensured by Asn residues of apoA and Ins fibers, and predominantly by Gly and Leu residues of A β (1-42) and Lz. Additionally, π - σ contacts between His residues of A β (1-42) and Chol favor the intercalation of sterol into the amyloid fibril.

Table 1. Parameters of molecular docking of amyloid fibrils with lipid molecules

Protein	Lipid	GBE, kcal/mol	ACE, kcal/mol	Amino acid residues involved in complexation
A β	Chol	-33.19	-12.28	Gly, Leu, Ile, His
	CL	-44.39	-13.14	Gln, His, Leu, Ile, Gly, Val
	POPC	-63.18	-17.89	Lys, Gln, His
apoA-83	Chol	-7.26	-4.36	Asn, Lys, Gln
	CL	-13.84	-4.25	Gln, Asn, Ala, Lys
	POPC	-29.74	-4.32	Ser, Leu, Gly, Gln, Asn, Lys
Ins	Chol	-15.87	-1.89	Asn, Tyr
	CL	-28.24	-7.78	Asn, Glu, Tyr, Phe, Val
	POPC	-69.25	-10.34	Gln, Phe, Leu, Tyr, Glu, Asn
Lz	Chol	-29.11	-16.83	Gly, Trp, Leu
	CL	-32.12	-17.83	Trp, Gly
	POPC	-42.16	-22.38	Trp, Ser, Leu, Gly

As shown in Fig. 1, B cardiolipin are characterized mostly by superficial location in the complexes with amyloid fibrils which can be explained by the steric restrictions arising from the bulky structure of this phospholipid containing four acyl chains. No specific interactions were revealed for the association of A β (1-42) and Ins fibers with CL acyl tails, where amyloid-lipid assemblies were found to be stabilized predominantly by van der Waals and alkyl interactions (Fig. 1, B). Furthermore, hydrogen bonds were formed between His of A β (1-42) and CL headgroup. In turn, the binding of fibrillar apoA-83 and Lz to anionic cardiolipin exhibited more complex behavior. Specifically, apart from van der Waals, H-bond and alkyl contacts, Asn residues of apoA-83 are involved in the metal-acceptor and unfavorable positive-positive interactions with CL. The complexation of CL with Lz amyloid fibers is stabilized by a set of van der Waals, attractive charge, and unfavorable positive-positive contacts. Interestingly, Trp residues were found to be responsible for all these types of interactions.

Shown in Fig. 1, C are the docking poses of the fibril complexes with POPC which demonstrate the preferable surface location of POPC with some protrusion of its acyl chains into fibril grooves. Similar to Chol and CL, the association of POPC with all types of amyloid fibers studied here was found to be stabilized by van der Waals and alkyl/ π -alkyl interactions. Additionally, conventional and carbon hydrogen bonds were formed between Gln, Gly, Leu, Tyr amino acid residues and fibrillar A β (1-42), Ins and Lz. Furthermore, attractive charge and metal-acceptor contacts were revealed for apoA and Lz amyloid fibrils, while the covalent bond between Tyr residue of Ins and phosphate group of POPC was formed in the case of Ins fibers. Interestingly, unfavorable positive-positive interactions were found to contribute also into POPC complexation with fibrillar Lz. In the present context, it is noteworthy that unfavorable interactions may appear due to several limitations of molecular docking protocol: i) unaccounted flexibility of protein backbone, ii) insufficient conformational sampling of the protein because of repeated fibrillar structure, iii) steric restrictions.

Table 2. Structural characteristics of binding pockets for lipids within the amyloid fibrils predicted by DoGSiteScorer

Protein	Lipid	Volume, Å ³	Surface, Å ²	Amino acid residues participating in the binding
A β (1-42)	Chol	57.4	181.8	Ala, Asn, Asp, Gly, Ile, Leu, Phe, Ser
	CL	137.3	265.3	Gly, Ala, Leu, Ile, Val, Gln
	POPC	85.5	197.2	Asn, Leu, Ile, Lys, Phe, His
apoA-83	Chol	80.8	304.5	Gly, Ala, Asn, Ile, Lys, Gln
	CL	112.3	567.1	Ala, Gln, Lys, Ser, Asn
	POPC	99.3	434.6	Lys, Leu, Ser, Gly, Asn
Ins	Chol	75.1	115.2	Asn, Cys, Gln, Leu, Tyr, Val
	CL	104.6	347.9	Ile, Glu, Gln, Tyr, Val, Asn, Phe
	POPC	90.4	262.6	Phe, Val, Asn, Cys, Tyr, Glu, Leu
Lz	Chol	26.5	234.4	Ser, Trp, Arg, Gly, Leu, Ile, Asn
	CL	118.6	438.2	Arg, Gly, Ile, Trp, Ser
	POPC	97.2	311.1	Gly, Ile, Leu, Arg, Trp, Ser

Importantly, most of the interacting amino acid residues defined by the Discovery Studio based on the PatchDock analysis, were found to be within the binding pockets predicted by the DoGSiteScorer server. The DoGSiteScorer is a grid-based method that uses a difference of Gaussian filter to detect potential binding pockets based on three-dimensional structure of the protein and ligand molecules. Specifically, the calculations of the amyloid fibril structures via DoGSiteScorer with respect to every lipid allowed us to identify from 2 to 8 binding pockets. However, for every amyloid-lipid complex the binding pocket with the highest score, calculated through the DoGSiteScorer, almost coincided with the binding site, revealed by the molecular docking. The structural properties of the binding pockets are shown in Table 2.

CONCLUSIONS

In summary, the present study provides additional arguments in favor of the possibility of direct interaction of individual lipid molecules with amyloid fibrils. The model fibril-lipid systems whose protein component was represented by the fibrillar lysozyme, insulin, A β (1-42) peptide and N-terminal (1-83) fragment, while a lipid component involved cholesterol, cardiolipin or phosphatidylcholine were investigated using the molecular docking tool. The analysis of the results obtained with PatchDock showed that Asn, Gly, Glu, Leu and Trp are the most common amino acid residues in the formation of van der Waals amyloid-lipid contacts for all types of lipids and proteins studied in the present contribution. In turn, a predominant role of Leu, Tyr and Trp among other residues in providing the alkyl/ π -alkyl interactions was demonstrated. Further studies in this direction are important for uncovering the determinants of amyloid biological activity and the development of therapeutics for amyloid diseases.

Acknowledgements

This work was supported by the Ministry of Education and Science of Ukraine (the project “Development of novel means of medical diagnostics by biomedical nanotechnologies and modern ultrasonic and fluorescence methods”).

ORCID IDs

Valeriya Trusova, <https://orcid.org/0000-0002-7087-071X>; Uliana Tarabara, <https://orcid.org/0000-0002-7677-0779>
Olga Zhytniakivska, <https://orcid.org/0000-0002-2068-5823>; Kateryna Vus, <https://orcid.org/0000-0003-4738-4016>
Galyna Gorbenko, <https://orcid.org/0000-0002-0954-5053>

REFERENCES

- [1] M.G. Iadanza, M.P. Jackson, E.W. Hewitt, N.A. Ranson, and S.E. Radford, *Nat. Rev. Mol. Cell. Biol.* **19**, 755 (2018). <https://doi.org/10.1038/s41580-018-0060-8>
- [2] T. Knowles, M. Vendruscolo, and C. Dobson, *Nat. Rev. Mol. Cell. Biol.* **15**, 384 (2014). <https://doi.org/10.1038/nrm3810>
- [3] D.C. Bode, M. Freeley, J. Nield, M. Palma, and J.H. Viles, *J. Biol. Chem.* **294**, 7566 (2019). <https://doi.org/10.1074/jbc.AC118.007195>
- [4] K. Sasahara, K. Morigaki, and K. Shinya, *Phys. Chem. Chem. Phys.* **15**, 8929 (2013). <https://doi.org/10.1039/C3CP44517H>
- [5] N.P. Reynolds, A. Soragni, M. Rabe, D. Verdes, E. Liverani, S. Handschin, R. Riek, and S. Seeger, *J. Am. Chem. Soc.* **133**, 19366 (2011). <https://doi.org/10.1021/ja2029848>
- [6] M.F. Engel, L. Khemtémourian, C.C. Kleijer, H.J. Meeldijk, J. Jacobs, A.J. Verkleij, B. de Kruijff, A. Killian, and J.W. Höppener, *Proc. Natl. Acad. Sci. U.S.A.* **105**, 6033–6038 (2008). <https://doi.org/10.1073/pnas.0708354105>
- [7] E. Sparr, M.F. Engel, D.V. Sakharov, M. Sprong, J. Jacobs, B. de Kruijff, and J.W. Höppener, A. Killian, *J. FEBS Lett.* **577**, 117 (2004). <https://doi.org/10.1016/j.febslet.2004.09.075>
- [8] N. Arispe, E. Rojas, and H.B. Pollard, *Proc. Natl. Acad. Sci. U.S.A.* **90**, 567 (1993). <https://doi.org/10.1073/pnas.90.2.56>
- [9] N. Arispe, H.B. Pollard, E. Rojas, *Mol. Cell. Biochem.* **140**, 119 (1994). <https://doi.org/10.1007/BF00926750>
- [10] N. Arispe, H.B. Pollard, E. Rojas, *Proc. Natl. Acad. Sci. U.S.A.* **90**, 10573 (1993). <https://doi.org/10.1073/pnas.90.22.10573>
- [11] J.M. Sanderson, *J. Biol. Chem.* **298**, 102108 (2022). <https://doi.org/10.1016/j.jbc.2022.102108>
- [12] G.P. Gellermann, T.R. Appel, A. Tannert, A. Radestock, P. Hortschansky, V. Schroeckh et al. *Proc. Natl Acad. Sci. U.S.A.* **102**, 6297 (2005). <https://doi.org/10.1073/pnas.0407035102>
- [13] G.P. Gellermann, T.R. Appel, P. Davies, S. Diekmann, *Biol. Chem.* **387**, 1267 (2006). <https://doi.org/10.1515/BC.2006.157>
- [14] J. M. Sanderson, Far from inert: membrane lipids possess intrinsic reactivity that has consequences for cell biology. *BioEssays*, **42**, e1900147 (2020). <https://doi.org/10.1002/bies.201900147>
- [15] M. Babych, P.T. Nguyen, M. Côte-Cyr, N. Kihal, N. Quittot, and M. Golizeh et al. *Biochemistry*, **60**, 2285 (2021). <https://doi.org/10.1021/acs.biochem.1c00308>
- [16] A.E. Saghir, G. Farrugia, N. Vassailo, *Chem. Phys. Lipids* **234**, 105010 (2021). <https://doi.org/10.1016/j.chemphyslip.2020.105010>
- [17] J.R. Brender, U.H. Durr, D. Heyl, M.B. Budarapu, and A. Ramamoorthy, *Biochim. Biophys. Acta*, **1768**, 2026 (2007). <https://doi.org/10.1016/j.bbamem.2007.07.001>
- [18] M. Grey, S. Linse, H. Nilsson, P. Brundin, E. Sparr, *J. Parkinson's Dis.* **1**, 359 (2011). <https://doi.org/10.3233/JPD-2011-11067>
- [19] E. Hellstrand, A. Nowacka, D. Topgaard, S. Linse, and E. Sparr, *PLoS One* **8**, e77235 (2013). <https://doi.org/10.1371/journal.pone.0077235>
- [20] C. Zhang, G. Vasmatazis, J.L. Cornette, and C. De Lisi, *J. Mol. Biol.* **267**, 707 (1997). <https://doi.org/10.1006/jmbi.1996.0859>
- [21] D. Schneidman-Duhovny, Y. Inbar, R. Nussimov, and H. Wolfson, *Nucl. Acid Res.* **33**, W363 (2005). <https://doi.org/10.1093/nar/gki481>

ВЗАЄМОДІЯ ФІБРИЛЯРНИХ БІЛКІВ З ЛІПІДАМИ: ДОСЛІДЖЕННЯ МЕТОДОМ МОЛЕКУЛЯРНОГО ДОКІНГУ

Валерія Трусова, Уляна Тарабара, Ольга Житняківська, Катерина Вус, Галина Горбенко

*Кафедра медичної фізики та біомедичних нанотехнологій, Харківський національний університет імені В.Н. Каразіна
м. Свободи 4, Харків, 61022, Україна*

Агрегація неправильно згорнутих білків з утворенням специфічних впорядкованих агрегатів, амілоїдних фібрил, пов'язаних з більш ніж 40 захворювань людини, наразі привертає велику увагу дослідників у біомедичному та нанотехнологічному аспектах. Згідно з сучасними уявленнями, ці агрегати та їх олігомерні інтермедіати здійснюють їх токсичний вплив переважно на рівні клітинних мембран. Окрім цього, мембранні ліпіди були виявлені в багатьох амілоїдних депозитах *in vivo*, що є свідченням здатності ліпідних молекул вбудовуватись в структуру фібрил та впливати на їх морфологію і механічні властивості. Однак, біологічна роль та структурні передумови фібрил-ліпідних взаємодій залишаються нез'ясованими. У даній роботі методом молекулярного докінгу було проведено дослідження взаємодії між амілоїдними фібрилами та ліпідами в модельних системах, що містили фібрилярні форми лізоциму, інсуліну, A β (1-42) пептиду та N-термінального (1-83) фрагменту аполіпопротеїну A-I у якості білкового компоненту, та холестерин, кардіоліпін і фосфатидилхолін у якості ліпідного компоненту. З використанням web-серверу PatchDock та програмного пакету BIOVIA Discovery Studio були охарактеризовані структурні особливості фібрил-ліпідних асоціатів. Показано, що ван-дер-ваальсові та алкіл/ π -алкіл взаємодії домінують у стабілізації всіх типів фібрил-ліпідних комплексів. Аналіз найбільш енергетично вигідних структур, отриманих методом докінгу, свідчить про переважно поверхневу локалізацію ліпідів та часткове проникнення ацильних ланцюгів кардіоліпіну та фосфатидилхоліну у фібрилярні ґруви.

Ключові слова: амілоїдні фібрили; лізоцим; інсулін; A β (1-42) пептид; аполіпопротеїн A-I; комплекс фібрила-ліпід; молекулярний докінг

EVALUATION OF THE INFLUENCE OF BODY MASS INDEX AND SIGNAL-TO-NOISE RATIO ON THE PET/CT IMAGE QUALITY IN IRAQI PATIENTS WITH LIVER CANCER[†]

 Aya B. Hade,  Samar I. Essa*

Department of Physics, College of Science, University of Baghdad, Baghdad, Iraq

**Corresponding author: samar.o@sc.uobaghdad.edu.iq*

Received February 1, 2023; revised February 5, 2023; accepted February 7, 2023

Image quality has been estimated and predicted using the signal to noise ratio (SNR). The purpose of this study is to investigate the relationships between body mass index (BMI) and SNR measurements in PET imaging using patient studies with liver cancer. Three groups of 59 patients (24 males and 35 females) were divided according to BMI. After intravenous injection of 0.1 mCi of ¹⁸F-FDG per kilogram of body weight, PET emission scans were acquired for (1, 1.5, and 3) min/bed position according to the weight of patient. Because liver is an organ of homogenous metabolism, five regions of interest (ROI) were made at the same location, five successive slices of the PET/CT scans to determine the mean uptake (signal) values and its standard deviation. We obtained the liver's Signal-to-Noise Ratio from the ratio of both. Weight, height, SNR, and Body Mass Index were determined using a spreadsheet, and graphs were created to show the relationship between these variables. The graphs demonstrated that SNR decreases when BMI increases and that, despite an increase in injection dose, SNR also decreases. This is because heavier individuals take higher doses and, according to reports, have lower SNR. These results show that, despite receiving larger FDG doses, heavier patients' images, as measured by SNR, are of lower quality than thinner patients' images.

Keywords: *Body mass index, Signal-to-noise ratio, Image quality; ¹⁸F- FDG, PET/CT*

PACS: 87.57.-s, 87.57.-C, 87.57.U-, 87.57.uk

1. INTRODUCTION

Worldwide, cancer ranks as the second largest cause of mortality among humans, caused by unhealthy lifestyles and lack of physical activity. Late disease identification is one of the causes contributing to such a high mortality rate [1,2]. Therefore, early identification is critical because it is the single most important factor in increasing a patient's chances of survival [3]. Cancers typically exhibit morphological, physiological, and molecular characteristics that can be imaged using a variety of clinical imaging techniques that visualize internal organs in an effort to diagnose the disease. As a result of advancements in computer and imaging technology, multiple clinical imaging modalities are now available, making it possible to diagnose the problem, track its evolution, and plan the appropriate follow-up treatments, some of these methods—such as X-ray radiography, computed tomography (CT), magnetic resonance imaging (MRI), and ultrasonography—are classified as anatomical imaging techniques. Functional imaging techniques include Single Photon Emission Computed Tomography (SPECT) and Positron Emission Tomography (PET) [4].

In oncology, PET has been widely used with ¹⁸F-FDG as a significant imaging technique for cancer, which allows for the monitoring of glucose consumption in vivo, with a focus on tumor glucose metabolism. As a result, a PET image depicts the distribution of an injected tracer throughout the body of a patient based on the metabolic rate of each region. ¹⁸F-FDG is distinguished by its relatively short half-life (109.8 minutes) that emits gamma rays at 1020 keV. The energy is sufficiently high to exit with minimal interactions with other tissues in the body [5].

PET imaging has been characterized by a relatively low image quality due to its low sensitivity as well as the acquisition of random and scattered coincidences during the imaging process. In an effort to evaluate PET image quality, the image noise is one of the different metrics that have historically been relied upon. It is directly determined from the image and calculated as the standard deviation of the counts in a region of interest. For ¹⁸F-FDG PET/CT, images must be of adequate quality to accomplish many functions, such as disease identification, staging, and therapy response monitoring, with the recent increase in the number of PET/CT operations, it is becoming increasingly necessary to limit patient exposure to radiation without compromising image quality [6].

Recent improvements in PET/CT technology have led to better image quality than standard PET. This is because CT-based attenuation correction is less noisy, and scintillator crystals and detector electronics work better. Image noise has been used as an indicator of image quality since the higher the image noise at a fixed signal level, the lower the signal-to-noise ratio of the object of interest and hence the ability to detect the object. Even PET/CT images of obese patients, however, are frequently of poor quality. Several studies have suggested that optimizing radiopharmaceutical acquisition durations or administered doses is required to improve image quality in obese patients [7]. The purpose of our study was to assess the effects of injected dose and body mass index on ¹⁸F-FDG PET/CT image quality.

2. MATERIALS AND METHODS

Participants in the study ranged in age from 15 to 85 years old and were referred to the Al-Andalus Specialist Hospital between November 2022 and January 2023. There were 24 male participants and 35 female participants in the

[†] Cite as: A.B. Hade, and S.I. Essa, East Eur. J. Phys. 1, 241 (2023), <https://doi.org/10.26565/2312-4334-2023-1-32>

© A.B. Hade, S.I. Essa, 2023

study. The mean age of the participants was 58.01± 13.18. Before proceeding with the PET/CT scans, we made sure to get the patients' informed consent first. The hospital's ethics committee had previously given its blessing to our study.

In the course of our investigation, we made use of a Discovery IQ PET/CT scanner (GE Healthcare, Milwaukee, WI, USA). This scanner's detector was made up of Bi4Ge3O12 (BGO) crystals, each of which measured 6.3 by 6.3 by 30 millimeters. At the one-bed position, the transaxial field of vision (FOV) measured 700 millimeters, the axial field of view measured 260 millimeters, and 79 axial slices were acquired. The window width for the energy range was 435-650 keV, and the window width for the coincidence time range was 9.5 ns. We obtained a matrix with a dimension of 192 by 192, and the thickness of each slice was 3.27 millimeters. The amount of slice overlap that occurred between beds was 19 slices.

Patients who had had a blood sugar concentration in their fasting blood that was more than 200 mg/dL at the time of the examination were not permitted to take part in any aspect of the study.

Before receiving an injection of ¹⁸F-FDG, all of the patients went without food for at least four to six hours. Before giving the patient ¹⁸F-FDG, an intravenous cannula was inserted in either the patient's arm or the palm of their hand, and a blood sample was taken to determine the patient's glycaemia. Images were taken 45–90 minutes following injection of the contrast agent. Patients were placed in a supine position with both of their arms elevated.

The time required to acquire an emission was (1-3) minutes for each bed position. In order to evaluate the connection between these factors and the ¹⁸F-FDG PET image quality, the patient-dependent parameters for each patient were gathered or calculated. This was done in order to conduct the study. The patient files were searched for information regarding body weight (BW) and body height. The body mass index, sometimes known as BMI, was determined.

$$BMI = \frac{\text{Weight in kg}}{(\text{height in m})^2} \tag{1}$$

Body mass index (BMI), was categorized according to the World Health Organization classification, namely underweight (BMI <18.5 kg/m²), normal (18.5 – 24.99 kg/m²), overweight (25 – 30 kg/m²) and obese (≥ 30 kg/m²) [8]. The evaluation of image quality with regard to contrast and noise is a key parameter that is frequently applied to tumor identification. SNR, which is correlated with the number of events found, was determined to measure the PET scanner's effectiveness in terms of the object's visibility. The liver's SNR was employed as an indicator of image quality since it is the only human organ with a somewhat uniform absorption of FDG. The SNR is defined as the difference between the measured region's mean pixel value (mean) and standard deviation (SD) [9]:

$$SNR = \frac{\text{mean}}{SD} \tag{2}$$

2.1. Statistical Analysis

To express all results, the mean and standard deviation (SD) were utilized. All statistical analysis was performed using Microsoft Office Excel 2013. The definition of statistical significance was a p-value less than 0.05.

3. RESULTS AND DISCUSSION

Table 1 shows that when the BMI increased, the dose/weight and SNR decreased. The mean injection dose for the normal group was 7.12 mci, 9.66 mci for obese, and the injection mean dose for the overweight group was 8.78mci.

Table 1. Results for Administered ¹⁸F-FDG.

Groups	Weight (kg)	Height (m)	BMI kg/(m) ²	Mean ± SD			SNR
				Injection dose (mci)	Dose/weight (mci/kg)		
Normal weight	58.47±6.10	1.61±0.08	22.66 ± 2.24	7.12 ± 0.5	0.12 ± 0.008	6.23 ± 2.95	
Overweight	76.71±8.46	1.68±0.08	27.06 ±1.45	8.78 ± 0.73	0.11 ± 0.007	4.33 ± 2.26	
Obese	92.22±12.55	1.62±0.06	36.04 ± 6.82	9.66 ± 0.55	0.1 ± 0.01	3.83 ± 1.68	

* p-value < 0.05 between BMI vs SNR.

After filling in all the values in the Table 1 about mean, deviation, SNR, weight (in kg), height (in m), and BMI, several graphs related to SNR and BMI were made to see which were the results. All the graphs were made with the values of the PET to see if there were any significant differences between them. BMI (kg/m²) and SNR for normal weight group was (mean BMI 22.66 ± 2.24, and SNR 6.23 ± 2.95, p value < 0.05).

The value of BMI and SNR for overweight group is (27.06 ±1.45) and (4.33 ± 2.26), respectively with also significant. For obese group the mean values for both BMI and SNR were (mean BMI 36.04 ± 6.82, and SNR 3.83 ± 1.68, with p value < 0.05). The relationships between the SNR and BMI for (normal, overweight, and obese) groups are shown in Figures 1(a), (b), and (c) respectively. The figures clearly show that SNR decreases with a BMI increase.

For clinical whole-body FDG-PET scans for oncology, full 3D data acquisition is now the standard protocol. But noise components like random and scatter have a big effect on the quality of the image. Before a doctor makes a diagnosis, the quality of the PET image should be looked at to see if it is good enough for a diagnosis or not, but there is no standard way to do this yet [10].

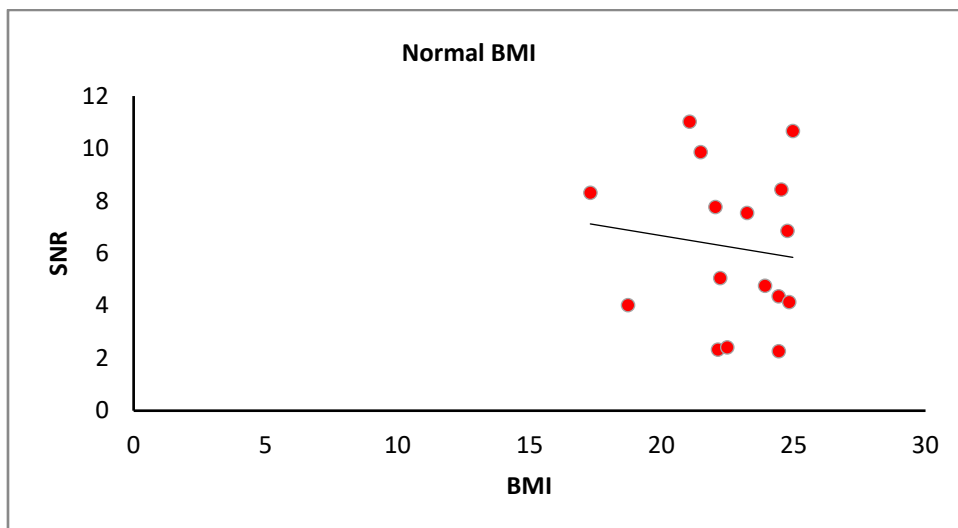


Figure (1a): Relation between BMI (normal) and SNR on the PET.

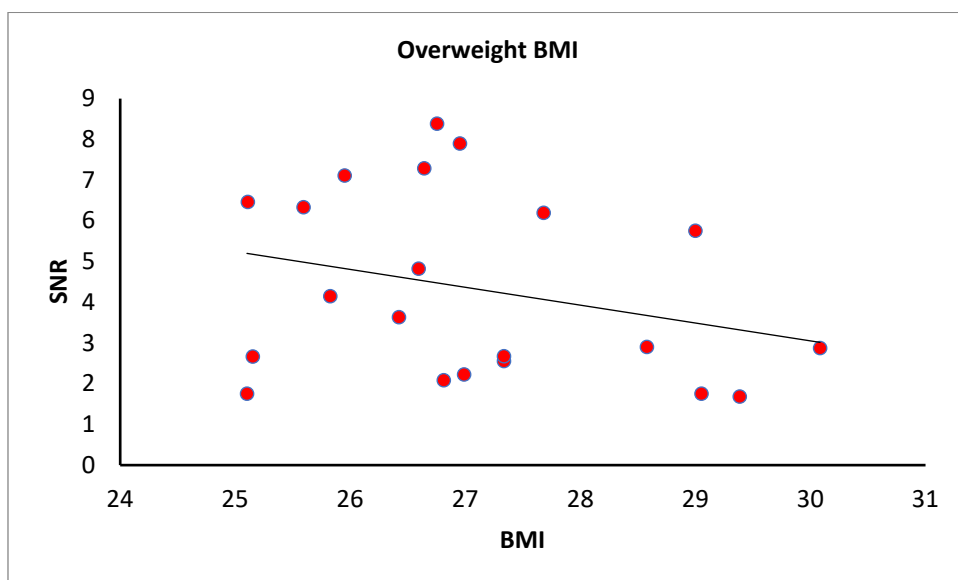


Figure (1b): Relation between BMI (overweight) and SNR on the PET.

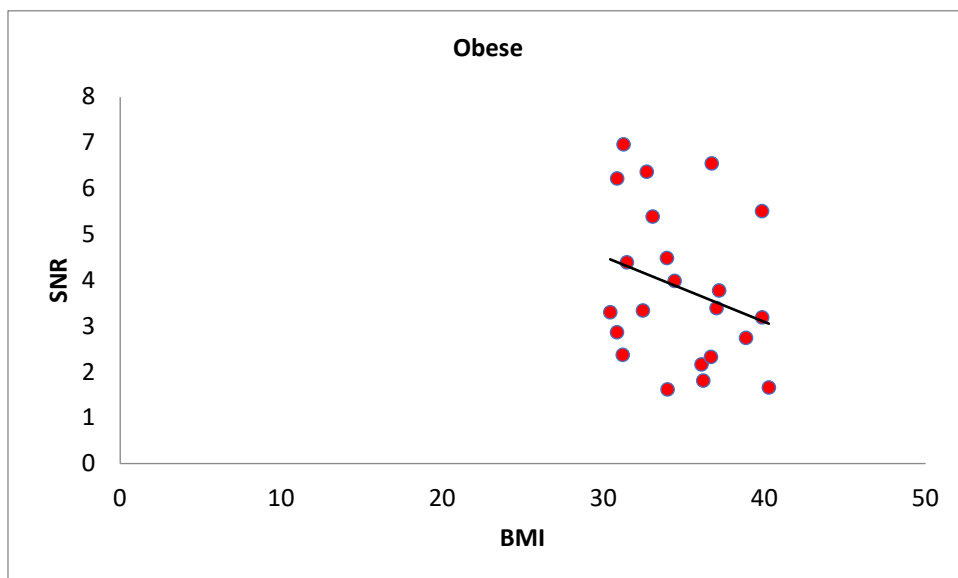


Figure (1c): Relation between BMI (obese) and SNR on the PET.

Investigating the impact of body mass index on image noise measures in PET scans was the purpose of this effort. Our evaluation of SNR was carried out on bed frames covering the livers of all of the patients. Because the liver is the largest organ in the body and has a radiotracer uptake that is relatively consistent and uniform, we decided to use this bed position. As a measure of image noise, we used the SD of the pixel values inside the area of interest (ROI). Despite being often utilized in clinical imaging research, the SD of ROI has limitations as a noise indicator. The term "noise" refers to the degree of radioactive fluctuation (SD) in image of uniform uptake. Image noise is a result of numerous variables. The quantity of photons detected determines stochastic noise. The reconstruction process produces structured noise, which is impacted by visual field heterogeneity [11].

Numerous patient-related problems could affect the signal-to-noise ratio. The administration of FDG is the first. The second factor is body size, specifically the total volume of the body where FDG is dispersed and diluted. Thirdly, the mean path length of photons from the liver to the detector depends on the size of the subject. As a result, larger people will exhibit increased photon attenuation. The "half distance"—analogous to the half-life—over which 511 keV photons in water attenuate 50% of their counts is 7.3 cm. Consequently, the count density may be significantly impacted by increased abdominal girth. Fourthly, although it wouldn't be anticipated that patient movement would correlate with body size indices, it would also reduce the signal-to-noise ratio [12].

After filling in all the values in the Table (1) about mean, standard deviation, SNR, injection dose (in mci), weight (in kg), height (in m) and BMI, several figures related to BMI and SNR were made to see which the results were. All the figures were made with the values of the PET to see if there are any significant differences between them. Our findings indicate that the signal-to-noise ratio (SNR) and image noise worsen dramatically with rising BMI. This is due to the loss of real coincidence events, most likely as a result of greater attenuation in larger patients. However, the quality appears to be optimal when the patient's weight is regarded as normal (between the BMI values of 18 and 24, approximately).

Figure (1a, b, and c) shows a scatter plot of the SNR versus BMI for both scanners. Here each dot in the figure represents a single patient. The figures indicate that SNR decreases more quickly at lower BMI values than at higher values, indicating that image quality deteriorates more quickly as BMI increases from low values. More dosage cannot, however, be injected to compensate for poorer image quality in larger individuals. These findings confirm earlier research that was extrapolated from phantom data and published. By extending the scan time, it may be possible to improve image quality in this patient population [13,14].

Individual variability in liver metabolism, attenuating tissue thicknesses, image reconstruction parameters, and aberrations such as respiratory motion blur impair the ability of hepatic SNR to distinguish between image quality [15]

4. CONCLUSION

Based on the outcomes of this investigation, it is safe to conclude that weight plays a significant effect in the quality of the PET/CT image. It affects the liver's SNR. The more heavy the patient is, the less SNR the image. This was also true for the BMI, which considers height. Changing specific settings, such as attenuation correction or others, to reduce random and scatter noise may be good for fat people, but it is not a cure. Adjusting these parameters may result in an image with a greater SNR and a smoother appearance, but it may reduce the ability to identify lesions. Furthermore, each nuclear medicine department has its own protocols and logistics; hence, changing methods, such as scanning every patient for extended periods of time, may not be appropriate.

ORCID IDs

©Aya B. Hade, <https://orcid.org/0000-0002-1246-3024>; ©Samar I. Essa, <https://orcid.org/0000-0001-9821-2279>

REFERENCES

- [1] N. Waeleh, M.I. Saripan, M. Musarudin, S. Mashohor, and F.F.A. Saad, "Correlation between 18F-FDG dosage and SNR on various BMI patient groups tested in NEMA IEC PET phantom", *Applied Radiation and Isotopes* **176**, 109885 (2021). <https://doi.org/10.1016/j.apradiso.2021.109885>
- [2] A.K. Yadav, and N.S. Desai, "Cancer stem cells: acquisition, characteristics, therapeutic implications, targeting strategies and future prospects", *Stem Cell Rev. Reports*, **15**, 331 (2019). <https://doi.org/10.1007/s12015-019-09887-2>
- [3] M.C. Liu, G.R. Oxnard, E.A. Klein, C. Swanton, M.V. Seiden, CCGA Consortium, "Sensitive and specific multi-cancer detection and localization using methylation signatures in cell-free DNA", *Ann. Oncol.* **31**, 745 (2020). <https://doi.org/10.1016/j.annonc.2020.02.011>
- [4] E. Hubbell, C.A. Clarke, A.M. Aravanis, and C.D. Berg, "Modeled reductions in late-stage cancer with a multi-cancer early detection test", *Canc. Epidemiol. Biomarkers Prev.* **30**, 460 (2020). <https://doi.org/10.1158/1055-9965.EPI-20-1134>
- [5] M.R. Hasan, S.M. Kadam, and S.I. Essa, "Diffuse Thyroid Uptake in FDG PET/ CT Scan can Predict Subclinical Thyroid Disorders", *Iraqi Journal of Science*, **63**(5), 2000 (2022). <https://doi.org/10.24996/ij.s.2022.63.5.15>
- [6] S. Kalman, and T. Turkington, "Introduction to PET instrumentation (multiple letters)", *J. Nucl. Med. Technol.* **30**, 63 (2002). PMID: 12055279
- [7] N. Shimada, H. Daisaki, T. Murano, T. Terauchi, H. Shinohara, and N. Moriyama, "Optimization of the scan time is based on the physical index in FDG-PET/CT (in Japanese with English abstract)", *Nihon Hoshasen Gijutsu Gakkai Zasshi*, **67**(10), 1259 (2011). <https://doi.org/10.6009/jjrt.67.1259>
- [8] World Health Organization, *Building foundations for health, progress of member states: report of the WHO Global observatory for health*, (World Health Organization, 2006).

- [9] E.H. de Groot, N. Post, R. Boellaard, N.R.L. Wagenaar, A.T.M. Willemsen, and J.A. van Dalen, "Optimized dose regimen for whole-body FDG-PET imaging", *EJNMMI Research*, **3**, 63 (2013). <https://doi.org/10.1186/2191-219x-3-63>
- [10] R.D. Badawi, P.K. Marsden, B.F. Cronin, J.L. Sutcliffe, and M.N. Maisey, "Optimization of noise-equivalent count rates in 3D PET", *Phys. Med. Biol.* **41**, 1755 (1996). <https://doi.org/10.1088/0031-9155/41/9/014>
- [11] Y. Masuda, C. Kondo, Y. Matsuo, M. Uetani, and K. Kusakabe, "Comparison of imaging protocols for ^{18}F -FDG PET/CT in overweight patients: optimizing scan duration versus administered dose", *J. Nucl. Med.* **50**, 844 (2009). <https://doi.org/10.2967/jnumed.108.060590>
- [12] Y. Sugawara, K.R. Zasadny, A.W. Neuhoﬀ, and R.L. Wahl, "Reevaluation of the standardized uptake value for FDG: variations with body weight and methods for correction", *Radiology*, **213**, 521 (1999). <https://doi.org/10.1148/radiology.213.2.r99nv37521>
- [13] M. Danna, M. Lecchi, V. Bettinardi, M. Gilardi, C. Stearns, G. Lucignani, and F. Fazio, "Generation of the acquisition specific NEC (AS-NEC) curves to optimize the injected dose in 3D ^{18}F -FDG whole body PET studies", *IEEE Trans. Nucl. Sci.* **53**, 86 (2006). <https://doi.org/10.1109/TNS.2005.862966>
- [14] C.C. Watson, M.E. Casey, B. Bendriem, J.P. Carney, D.W. Townsend, S. Eberl, S. Meikle, and F.P. DiFilippo, "Optimizing injected dose in clinical PET by accurately modeling the counting-rate response functions specific to individual patient scans", *J. Nucl. Med.* **46**, 1825 (2005). PMID: 16269596
- [15] Z.S. Mohammad, and J.M. Abda, "Positron Interactions with Some Human Body Organs Using the Monte Carlo Probability Method", *Iraqi Journal of Physics*, **20**(3), 50 (2022). <https://doi.org/10.30723/ijp.v20i3.1026>

ОЦІНКА ВПЛИВУ ІНДЕКСУ МАСИ ТІЛА ТА СПІВВІДНОШЕННЯ СИГНАЛ-ШУМ НА ЯКІСТЬ PET/CT-ЗОБРАЖЕНЬ У ПАЦІЄНТІВ ІРАКУ З РАКОМ ПЕЧІНКИ



Ая Б. Хаде, Самар І. Есса

Факультет фізики, Науковий коледж, Багдадський університет, Багдад, Ірак

Якість зображення було оцінено та передбачено за допомогою співвідношення сигнал/шум (SNR). Метою цього дослідження є дослідження зв'язків між вимірюваннями індексу маси тіла (BMI) і SNR при PET-зображенні з використанням досліджень пацієнтів із раком печінки. Три групи з 59 пацієнтів (24 чоловіки та 35 жінок) були розділені відповідно до BMI. Після внутрішньовенної ін'єкції $0,1 \text{ mCi } ^{18}\text{F}$ -FDG на кілограм маси тіла проводили PET-сканування випромінювання протягом (1, 1,5 і 3) хв/положення ліжка відповідно до ваги пацієнта. Оскільки печінка є органом однорідного метаболізму, п'ять областей інтересу (ROI) були зроблені в одному місці, п'ять послідовних зрізів сканування PET/CT, щоб визначити середні значення поглинання (сигналу) та його стандартне відхилення. Ми отримали співвідношення сигнал-шум печінки із співвідношення обох. Вага, зріст, SNR та індекс маси тіла були визначені за допомогою електронної таблиці, а графіки були створені, щоб показати зв'язок між цими змінними. Графіки продемонстрували, що SNR зменшується, коли BMI збільшується, і що, незважаючи на збільшення дози ін'єкції, SNR також зменшується. Це пояснюється тим, що люди з більшою вагою приймають вищі дози і, згідно з повідомленнями, мають нижчий SNR. Ці результати показують, що, незважаючи на отримання більших доз FDG, зображення важких пацієнтів, виміряні SNR, нижчої якості, ніж зображення тонших пацієнтів.

Ключові слова: *індекс маси тіла; співвідношення сигнал/шум; якість зображення; ^{18}F -FDG, PET/CT*

ENHANCEMENT OF THE TPD/AGO NPS HYBRIDE PHOTODETECTOR BY ADDING PEDOT PSS[†]

 **Shahlaa Majid J.***,  **Omar Adnan**

Department of Physics, College of Science, University of Baghdad, Baghdad, Iraq

**Corresponding Author e-mail: shahlaa.maged1204a@sc.uobaghdad.edu.iq*

Received January 13, 2023; revised February 1, 2023; accepted February 2, 2023

A photodetector was prepared by fusing AgO nanoparticles with a Alkyl-TPD (N'-diphenylbenzidine) polymer and depositing a TPD:AgO mixture on PS substrates using a spin coating technique. The response time of the synthesized (PSi/TPD:AgO) detector (by using a tungsten lamp with a 250 W/cm²) and its value (0.35 s) were measured in seconds. The detection, specificity, and photoresponse were (6.23×10⁸ W⁻¹, 3.611×10⁸ W⁻¹Hz^{1/2}cm, and 19.072×10⁻³ A/W). Hall measurements show that n-type nanoparticles have a carrier concentration of about (-1.15×10¹⁷ cm⁻³). With the addition of Poly(3,4-ethylenedioxythiophene):poly(styrene sulfonate) (PEDOT:PSS) polymer, the detection, specificity, optical response, and detector response time were improved to (80.06×10⁸ W⁻¹, 46.4×10⁸ W⁻¹Hz^{1/2} cm, 2019.48×10⁻³ A/W, and 5.3 ms), respectively.

Keywords: *Characteristics; Photocurrent Gain; Hall Effect; Specific Detectivity; Response Time*

PACS: 73.61.Ph, 78.20.-e, 78.66.-w, 78.66.Qn

1. INTRODUCTION

In the modern science landscape, AgO NPs are a well-known metal oxide whose popularity is on the rise due to its prevalence in a wide various possible application, Biomedical, zinc/silver oxide batteries, photovoltaic devices, optical switching, optical devices, magneto optical storage systems, sensors, the manufacture of nanoscale electronics, and oxidation analysis are all examples of applications for nanoscale electronics [1–4]. Silver being various forms and numerous phases the same as Ag₂O, Ag₃O₄, AgO, and Ag₂O₃, which are examples of inorganic materials, belong to this category [5–8]. Silver nanoparticles (AgNPs) have piqued the interest of many researchers and scientists due to their unique properties in physical, chemical, and biological fields when compared to their macroscale counterparts [2,13].

Experimentally, the researchers discovered that Ag₂O and AgO are more prevalent in visible phases than multivalent silver oxide (Ag₃O₄, Ag₂O₃) and have a high capacity specified [6, 7]. Several authors [9, 10] have investigated the fabrication and characteristics of silver and silver oxide thin films utilizing diverse approaches, radio frequency magnetron sputtering, the vapor solid liquid technique, etc. (The optical band gap of Ag₂O is highly dependent on its fabrication procedure). The use of nanoparticles of silver oxide containing a lattice parameter of 0.472 nm and a simple cubic structure as effective detergents catalysts for the activation of alkanes and olefin epoxidation, preservatives, colorants, and electrode materials is widespread in many industrial applications [11]. Due to its substantial optical band gap (2.5–3.1 eV), silver oxide is infrared transparent and can be seen. Silver nanoparticles (AgNPs) have piqued the interest of many researchers and scientists due to their unique properties in physical, chemical, and biological fields when compared to their macroscale counterparts [12,13]. Enabling the creation of a glass electrode and an antireflective coating for applications in the opto electrical field. In addition, silver oxide can be used to store data in both optical and magneto-optical ways. Silver oxide can reflect more than 70% of light over a wide range of wavelengths. This is useful because the material can be used to store short-wavelength optical data; an inorganic storage substance is used instead of the organic storage substance that was used before. Tominaga et al. [14]. In contrast to copper, which can be quickly oxidized at high temperatures and from which single crystals of Cu₂O may be produced, the brittleness of the silver-oxygen link limits the use of this method to produce Ag₂O unless extremely high oxygen pressures are used [15]. Once formed, Ag₂O is stable at ambient temperature but begins to disintegrate at over 60°C in a vacuum. In an HF-rich electrolyte; silicon is etched electrochemically to produce porous silicon (PS). Its structure is complicated, with nanometer-sized pores dispersed throughout a random network. The interesting features of the nanostructured silicon that constitutes the material's backbone result primarily from the electron-hole couples are quantum-confined. In recent years, visible light emission in response to optical and electrical pumping at room temperature has been recorded [16, 17]. PS has been shown to be useful in other ways as a passive material [18, 19, 20, 21]. For example, changing the electrochemical current over time while the material is growing makes it easy to make structures with multiple layers that can function as distributed Bragg reflectors (DBRs) [22, 23], microcavities [24], waveguides [25], etc. Alkyl-TPD (N'-diphenylbenzidine) is a typical substance with a 5.5 eV ionization potential and excellent transport hole mobility of 10³ cm²/Vs [26, 27]. TPD is often used in phosphorescence-organic light-emitting diodes as a blue-violet light-emitting material or host material due to its approximately 3.2 eV energy band wide, having the most molecular orbitals occupied (HOMO) and the lowest unoccupied molecular orbital (LUMO) of -5.5eV and -2.3 eV, respectively [28].

One of the most promising conductive polymers is poly(3,4-ethylenedioxythiophene):poly(styrene sulfonate) (PEDOT:PSS) [29-31]. During the last two decades, research on PEDOT:PSS has increased dramatically [32]. Polymer

[†] Cite as: M.J. Shahlaa, and O. Adnan, East Eur. J. Phys. 1, 246 (2023), <https://doi.org/10.26565/2312-4334-2023-1-33>

© M.J. Shahlaa, O. Adnan, 2023

photodetectors have drawn tremendous attention due to their inherent advantages of solution-based and low-cost fabrication, mechanical flexibility, and light weight over their inorganic counterparts [33–36]. In this study, more than one detector was manufactured to study the effect of adding PEDOTPSS. PSI (Poros silicon) was used as the substrate in all photodetectors manufactured.

2. EXPERIMENTAL WORK

Silver oxide was prepared by pulsed laser ablation method. The Nd:YAG laser utilized in the deformation process operates at a frequency of 6 Hz with a pulse width of 7 ns and a wavelength of 1064 nm. The laser pulses were concentrated on a 20 cm positive lens on a 2 mm dry AgO bulk specimen that had been moistened in chloroform with a laser power of 1000 mJ and 2000 shots. As a substrate, a monocrystalline a wafer of n-type silicon with an electrical resistivity of (0.008-0.02) $\Omega \cdot \text{cm}$ and (111) orientation was utilized. In order to get rid of the native oxygen, the wafer was immersed in 40% HF. Electrochemical etching (anodization) in a solution of ethanoic hydrofluoric acid at a current density of 20 mA/cm² for 20 minutes in the dark at 300K was used to make the porous layer. So that an oxide layer wouldn't form on top of the porous silicon film, ethanol was often added. The samples were then cleaned and air dried. A [TPD Polymer -chloroform] solution was prepared by dissolving 0.075 g of TPD in 3 ml of chloroform and stirring the mixture until completely dissolved.

- The fabrication of photodetector device is manufactured as follows:
 - p-TPD is used to form the photodetector's active layer by mixing a solution of AgO nanoparticles and p-TPD-chloroform in a mole ratio of 2:1.
 - The detector was then created by spin coating a TPD:AgO mixture on PSi. The mixture of AgO:TPD is deposited on PSi at 3000rpm for 15 seconds. After PSi/AgO:TPD has been precipitated. After that, it is put in an oven at a temperature of 50 degrees Celsius for 30 minutes.
- The fabrication of improved detector was started by add deposition of PEDOTPSS on PSi substrate .Then, it is deposited at a speed of 1,500 revolutions per minute for a duration of 30 seconds. After the precipitation process is done, the PSi/PEDOTPSS is put in an oven at 120°C for 20 minutes to matching with the substrate .The mixture of AgO:TPD is deposited on PSi/PEDOTPSS at 3000rpm for 15 seconds. After PSi/PEDOTPSS/AgO:TPD has been precipitated. After that, it is put in an oven at a temperature of 50 degrees Celsius for 30 minutes.

3. RESULTS AND DISCUSSION

3.1. MORPHOLOGICAL PROPERTIES

SEM images display clusters of spherical, bright spots (circles and inset picture) that correspond to silver oxide nanoparticles, with an average particle size of about (22-26) nm as shown in Fig.1.

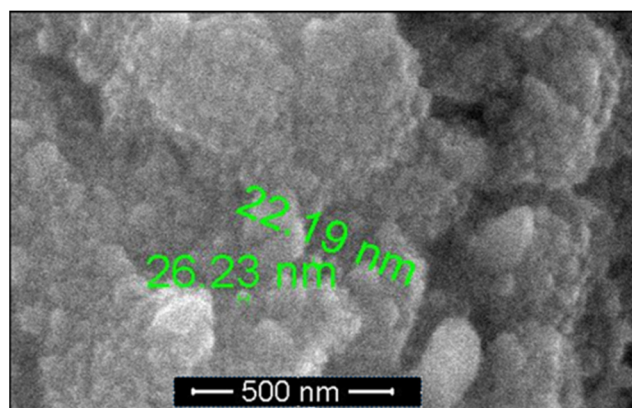


Figure 1. SEM image of AgO NPs.

3.2. OPTICAL PROPERTIES OF AGO NANOPARTICLES

UV–Vis spectroscopy, photoluminescence (PL) spectra, and FTIR spectroscopy were utilized to determine the optical characteristics of the AgO nanostructure. As seen in Fig. 2, the absorption spectra have a peak at 300 nm. Quantum-size impact is indicated by a blue shift in the absorption spectrum compared to the peak absorbance of AgO in bulk. Using the Tauc relation, calculate the optical bandgap energy (E_g) of the semiconductor [37]. A plot of $(h\nu)^2$ versus $h\nu$ shows a linear region of intermediate extrapolation of the linear portion can be used to determine E_g from the intersection with the $(h\nu)$ axis, as depicted in Fig.3. The calculated values of E_g for AgO are about 3.06 eV. PL spectra spectrum was shown in Fig.5. A 300 nm source is used to excite the specimen. Fitting Gaussian-shaped peaks to the PL spectrum and are centered at about 402 nm. The PL spectra of the NPs implies that there exist more defect energy levels (trap states or surface states) at 467 nm and 601 nm.

The FTIR spectra of AgO NPs were recorded at 3429.2 cm^{-1} for the alcohol stretching vibration (OH group), 2925.8 cm^{-1} for the vibrational stretching of the C-H methyl and methylene bonds, 1639.38 cm^{-1} for the stretching

vibration of the C=O bonds in pectin ester and carboxylic acid, etc. [38]. The weak band at 588.25 cm^{-1} attributable to the Ag-O vibration consists of those for crystal (lattice) and coordinated water in addition to Ag_2O . The obtained characteristic absorption band at 889.12 cm^{-1} is explained by the stretching and bending vibrations of Ag-O [39].

3.3. ELECTRICAL CHARACTERISTICS OF NANOPARTICLES AGO

1) Hall Effect

To analyze the electrical properties of AgO, the Hall Effect setup type (HMS3000) is utilized. The 600-nanometer-thick sheet exhibits n-type conductivity, characteristic of semiconductors. The mobility was $1.13 \times 10^3 (\text{cm}^2/\text{V}\cdot\text{sec})$, the conductivity and resistivity were $2.07 \times 10^1 (\Omega\cdot\text{cm})^{-1}$ and $4.83 \times 10^{-2} (\Omega\cdot\text{cm})$. The carrier concentration is $-1.15 \times 10^{17}\text{ cm}^{-3}$. The Hall coefficient $-5.45 \times 10^1 (1/\text{Cm}^3\cdot\text{C})$.

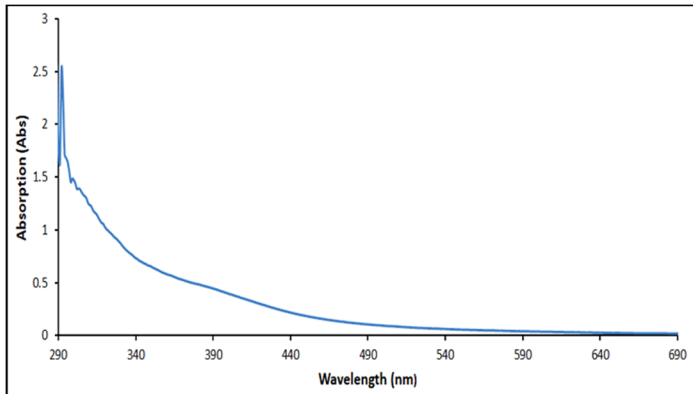


Figure 2. The absorption spectrum AgO nanoparticles

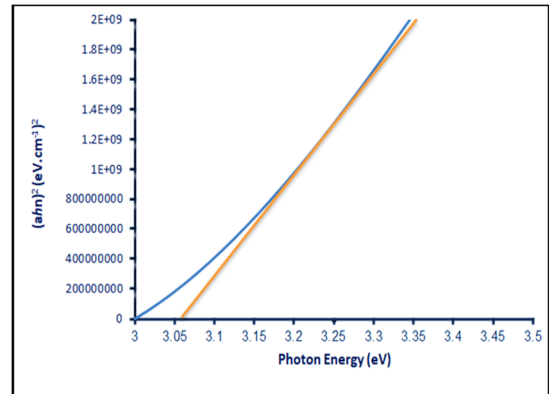


Figure 3. $(\alpha h\nu)^2$ vs. photon energy for AgO nanoparticles

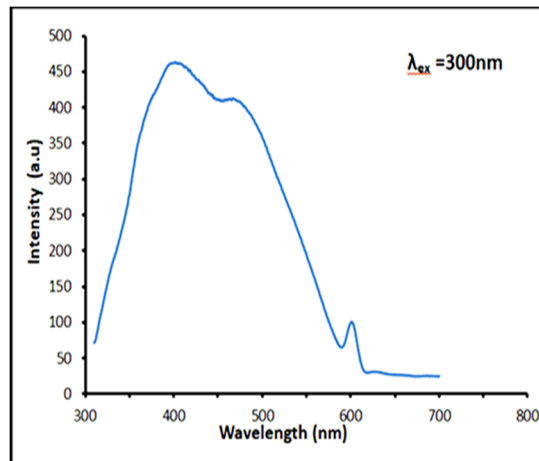


Figure 4. Photoluminescence spectrum of AgO nanoparticle.

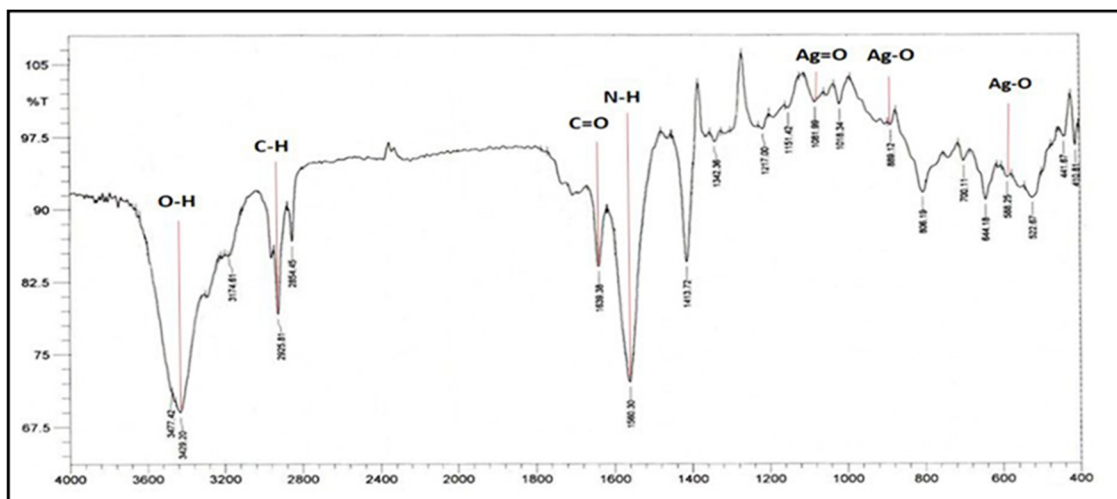


Figure 5. FTIR spectra for pure AgO NPs thin film.

2) Current–voltage measurements

The current-voltage (I–V) properties of the photodetector are examined as a function of the bias voltage in the absence and presence of a 250-W tungsten halogen lamp. At room temperature, a rise in current was noticed. Figure 6 displays I–V characteristics of PSi/TPD:AgO photodetector and PSi/PEDOTPSS/TPD:AgO photodetector. Curves of current–voltage are the most often employed device characterization technique. The current densities of the detectors were 4.768 A/cm² and 504.87 A/cm², respectively.

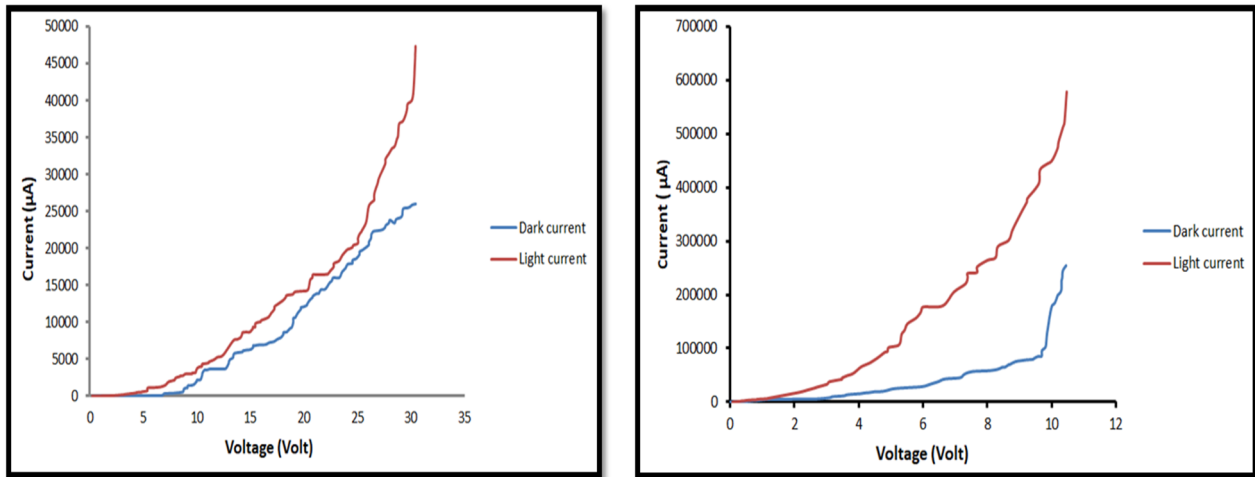


Figure 6. I–V characteristics of (a) PSi/TPD:AgO photodetector (b) PSi/PEDOTPSS/TPD:AgO photodetector

Calculated by dividing the photocurrent by the dark current at the same bias voltage, the photoconductive gain (G) is given by $G = \tau/T$, where T is the transient time between the detector electrodes and $\tau =$ is the charge carrier life time. The photocurrent gain of the PSi/ TPD:AgO detector was 1.447 while that of the PSi/TPD:AgO detector was 2.25. Using the value of gain G and the transit time for detectors The carries life time was found to be about 1.447 sec, 0.045 sec for PSi/TPD:AgO detector and PSi/PEDOTPSS/TPD:AgO detector respectively. There is a correlation between electrode separation and carrier mobility, which in turn has an effect on the transient time; $T=L^2/\mu V$, where L is the distance between the electrodes, μ is the carrier mobility, and V is the bias voltage. Using the value of transient time, electrode spacing and the bias voltage. The mobility of the carrier was found to be about 145.4×10^{-6} (cm²/V·sec) and 7272.7×10^{-6} (cm²/V·sec) for each detector respectively.

The prepared samples' Johnson noise is calculated using the equation:

$$I_n = (4K_B T \Delta f / R)^{1/2}, \tag{1}$$

where K_B is Boltzmann constant, R is resistance of photodetector, and T is temperature.

The Johnson noise of the PSi/TPD:AgO detector was 2.6808×10^{-9} A while that of the PSi/PEDOTPSS/TPD:AgO detector was 27.075×10^{-9} A.

Responsivity of the prepared samples is determined using equation:

$$R_\lambda = J / P_{opt}, \tag{2}$$

where J is the current density of the photodetector in (A/cm²), P_{opt} is the incident radiation power and its value (250 Watt/cm²).

The greatest values of the responsivity calculated by the PSi/PEDOTPSS/AgO:TPD photodetector. PSi/ TPD:AgO responsivity was 19.072×10^{-3} A/Watt, and PSi/TPD: AgO responsivity was 2019.48×10^{-3} A/Watt.

The specific detectivity D^* , referred to also as the normalized detectivity, which is the inverse of normalized noise equivalent power (NEP). To the detector area of 0.336 cm² and a noise electrical band width of 1 Hz. This reciprocal can be expressed as follows:

$$D^* = R_\lambda (A \Delta f)^{1/2} / I_n \tag{3}$$

Where R_λ is the optical response of the photodetector in (A/Watt), A is the sensitive area of the detector and I_n is the noise current is calculated from the dark current using the following formula:

$$I_n = (2 e I_d \Delta f)^{1/2}. \tag{4}$$

Where I_d represents the dark current, e represents the electron charge, and Δf represents the noise bandwidth, which results in a noise current for the PSi/TPD: AgO detector of about (3.057×10^{-11} A) and for the PSi/PEDOTPSS/AgO:TPD detector of about (25.226×10^{-11} A), at $\Delta f = 1$ Hz.

Utilizing the photosensitivity value, $A = 0.336 \text{ cm}^2$, the specific detectivity of PSi/TPD:AgO detector ($3.611 \times 10^8 \text{ Watt}^{-1} \text{ Hz}^{1/2} \text{ cm}$) and of PSi/PEDOTPSS/AgO:TPD detector ($46.4 \times 10^8 \text{ Watt}^{-1} \text{ Hz}^{1/2} \text{ cm}$).

The quantum efficiency is associated with the responsivity of the detector and calculated using the equation:

$$\eta = \frac{1240}{\lambda} R_{\lambda} \quad (5)$$

The quantum efficiency of PSi/TPD:AgO detector (36.383×10^{-3}), and of PSi/PEDOTPSS/TPD:AgO detector (3852.5×10^{-3}).

The addition of PEDOTPSS material increased the response time and the quantum efficiency. This means that this addition is useful for device optimization.

4. CONCLUSION

The PSi/TPD:AgO detector was prepared using silicon electrochemical etching, mixing silver oxide with TPD polymer, and depositing the TPD:AgO mixture by spin-coating method. PEDOTPSS was then deposited by spin-coating to prepare the PSi/PEDOTPSS/TPD:AgO detector. The addition of PEDOTPSS significantly improved the optical conductivity gain from 1.447 to 2.25. The luminous response has been increased from $19.072 \times 10^{-3} \text{ (A/Watt)}$ to $2019.48 \times 10^{-3} \text{ (A/Watt)}$, as has the response time range from 0.35 seconds to 0.0053 seconds.

ORCID IDs

Shahlaa Majid J., <https://orcid.org/0000-0002-0595-6293>; Omar Adnan, <https://orcid.org/0000-0003-3709-5245>

REFERENCE

- [1] S. Ravichandran, V. Paluria, G. Kumar, K. Loganathan, and B.R.K. Venkata, "A novel approach for the biosynthesis of silver oxide nanoparticles using aqueous leaf extract of *Callistemon lanceolatus* (Myrtaceae) and their therapeutic potential", *J. Exp. Nanosci.* **11**, 445458 (2016). <https://doi.org/10.1080/17458080.2015.1077534>
- [2] M. Limbitot, S. Kalyane, N. Sharanappa, S. Manjula, and B. Evale, "Electrical and dielectric studies of silver oxide doped polyaniline [AgO/PANI] nanocomposite", *Int. J. Adv. Sci. Res.* **3**, 87–93 (2018).
- [3] Z.H. Dhoondia, and H. Chakraborty, "Lactobacillus mediated synthesis of silver oxide nanoparticles", *Nanopart. Nanomater. Nanotechnol.* **2**, 1–7 (2012). <https://doi.org/10.5772/55741>
- [4] S. Sagadevan, "Synthesis, Structural, surface morphology, optical and electrical properties of silver oxide nanoparticles", *Int. J. Nanoelectron. Mater.* **9**, 37 (2016).
- [5] M.A. Hassan, I.R. Agool, and LM. Raoof, "Silver Oxide Nanostructured Prepared on Porous Silicon for Optoelectronic Application", *Appl. Nanosci.* **4**(4), 429 (2014). <https://doi.org/10.1007/s13204-013-0215-z>
- [6] G. Saroja, V. Vasu, and N. Nagarani, "Optical Studies of Ag₂O Thin Film Prepared by Electron Beam Evaporation Method", *O J. Metal.* **3**, 57 (2013). <http://dx.doi.org/10.4236/ojmetal.2013.34009>
- [7] P. Kavitha, S. Suseela, and M. Mary, "Synthesis and Characterization of Cadmium Sulfide Nanoparticles", *Int. J. Eng. Sci.* **2**(3), 108-110 (2013). <https://theijes.com/papers/v2-i3/Q02301080110.pdf>
- [8] B. Reidy, A. Haase, A. Luch, K.A. Dawson, and I. Lynch, "Mechanisms of Silver Nanoparticle Release, Transformation and Toxicity: A Critical Review of Current Knowledge and Recommendations for Future Studies and Applications", *Materials*, **6**(6), 2295 (2013). <https://doi.org/10.3390/ma6062295>
- [9] F.X. Bock, T.M. Christensen, S.B. Rivers, L.D. Doucette, R.J. Lad, "Growth and Structure of Silver and Silver Oxide Thin Films On Sapphire", *Thin Solid Films*, **468**(2-1), 57–64 (2004). <https://doi.org/10.1016/j.tsf.2004.04.009>
- [10] Q. Tian, D. Shi, and Y. Sha, "CuO and Ag₂O/CuO Catalyzed Oxidation of Aldehydes to The Corresponding Carboxylic Acids by Molecular Oxygen", *Molecules*, **13**(4), 948-957 (2008). <https://doi.org/10.3390/molecules13040948>
- [11] S. Wang, H. Li, H. Yu, J. Yu, and S. Liu, "Ag₂O as a new visible light photocatalyst: self-stability and high photocatalytic activity," *Chemistry A European Journal*, **17**(28), 7777 (2011). <https://doi.org/10.1002/chem.201101032>
- [12] S. Agrawal, M. Bhatt, S. Rai, A. Bhatt, P. Dangwal, and P. Agrawal, "Silver nanoparticles and its potential applications: a review", *J. Pharmacogn. Phytochem.* **7**, 930e937 (2018). <https://www.phytojournal.com/archives?year=2018&vol=7&issue=2&ArticleId=3470>.
- [13] M. Alhamid, B. Hadi, and A. Khumaeni, "Synthesis of silver nanoparticles using laser ablation method utilizing Nd:YAG laser", *AIP Conf. Proc.* **2202**, 020013 (2019). <https://doi.org/10.1063/1.5141626>
- [14] J. Tominaga, T. Nakano, and N. Atoda, *Extended Abstracts of the 39th Spring Meeting of the Japan Society of Applied Physics and Related Societies*, (Nippon Univ. Narashino, 30 aL-3, 1993).
- [15] Von E. Menzel, and C. Menzel-Kopp, *Z. Naturf.* **13a**, 986 (1958). https://zfn.mpg.de/data/Reihe_A/13/ZNA-1958-13a-0985.pdf
- [16] L.T. Canham, *Appl. Phys. Lett.* **57** (10), 1046 (1990). <https://doi.org/10.1063/1.103561>
- [17] A. Halimaoui, C. Oules, G. Bomchil, A. Bsiesy, F. Gaspard, R. Herino, M. Ligeon and F. Muller, *Appl. Phys. Lett.* **59** 304 (1991). <https://doi.org/10.1063/1.105578>
- [18] M.J. Sailor, in *Properties of Porous Silicon*, edited by L.T. Canham, (IEE Inspec., London, 1997), pp. 364.
- [19] W. TheiB, *Surf. Sci. Rep.* **29**(3/4), 91 (1997). [https://doi.org/10.1016/S0167-5729\(96\)00012-X](https://doi.org/10.1016/S0167-5729(96)00012-X)
- [20] M.V. Wolkin, S. Chan, and P.M. Fauchet, *Phys. Stat. Sol. (a)*, **182**, 573 (2000). [https://doi.org/10.1002/1521-396X\(200011\)182:1%3C573::AID-PSSA573%3E3.0.CO;2-G](https://doi.org/10.1002/1521-396X(200011)182:1%3C573::AID-PSSA573%3E3.0.CO;2-G)
- [21] W. Liu, et al., *J. Vac. Sci. & Techn. B*, **21**, 168 (2003). <https://doi.org/10.1116/1.1537714>
- [22] M.G. Berger, R. Arens-Fischer, M. Kruger, S. Billat, H. Luth, S. Hilbrich, W. TheiB, and P. Grosse, *Thin Solid Films*, **297**, 237 (1997). [https://doi.org/10.1016/S0040-6090\(96\)09361-3](https://doi.org/10.1016/S0040-6090(96)09361-3)
- [23] V. Agarwal, and J.A. del Rio, *Appl. Phys. Lett.* **82**, 1512 (2003). <https://doi.org/10.1063/1.1559420>
- [24] L. Pavesi, *Riv. Nuovo Cim.* **20**, 1 (1997). <https://doi.org/10.1007/BF02877374>

- [25] S. Nagata, C. Domoto, T. Nishimura, and K. Iwameji, *Appl. Phys. Lett.* **72**, 2945 (1998). <https://doi.org/10.1063/1.121502>
- [26] J.A. Chilton, and M.T. Goosey, editors, *Special polymer for electronics and optoelectronics*, (Chapman and Hall, London, 1995), pp. 351, ISBN 0-412-58400-X
- [27] Csavinszky, P. (1978). Quantum Mechanical Treatment of Transport Properties of Semiconductors: Possible Application to Polymers, in: *Quantum Theory of Polymers, NATO Advanced Study Institutes Series*, edited by J.M. André, J. Delhalle, and J. Ladik, vol 39, (Springer, Dordrecht, 1978). https://doi.org/10.1007/978-94-009-9812-4_15
- [28] F. Wang, Z. Chen, L. Xiao, B. Qu, and Q. Gong, “Enhancement of the power conversion efficiency by expanding the absorption spectrum with fluorescence layer”, *Optics Express*, **19**, A361–A368 (2011). <https://doi.org/10.1364/OE.19.00A361>
- [29] X. Yang, and M. Zhang, “Review of flexible microelectromechanical system sensors and devices”, *Nanotechnol. Precis. Eng.* **4**(2), 025001 (2021). <https://doi.org/10.1063/10.0004301>
- [30] Y. Chang, J. Zuo, H. Zhang, et al., « State-of-the-art and recent developments in micro/nanoscale pressure sensors for smart wearable devices and health monitoring systems”, *Nanotechnol. Precis. Eng.* **3**(1), 43 (2020). <https://doi.org/10.1016/j.npe.2019.12.006>
- [31] M. Sun, and X. Duan, “Recent advances in micro/nanoscale intracellular delivery”, *Nanotechnol. Precis. Eng.* **3**(1), 18 (2020). <https://doi.org/10.1016/j.npe.2019.12.003>
- [32] H. Shi, C. Liu, Q. Jiang, and J. Xu, “Effective approaches to improve the electrical conductivity of PEDOT:PSS review”, *Adv. Electron. Mater.* **1**(4), 1500017 (2015). <https://doi.org/10.1002/aelm.201500017>
- [33] C. Fuentes-Hernandez, W.-F. Chou, T.M. Khan, L. Diniz, J. Lukens, F.A. Larrain, V.A. Rodriguez-Toro, and B. Kippelen, *Science*, **370**, 698-701 (2020). <https://doi.org/10.1126/science.aba2624>
- [34] C. Li, H. Wang, F. Wang, T. Li, M. Xu, H. Wang, Z. Wang, et al., *Light Sci. Appl.* **9**, 31 (2020). <https://doi.org/10.1038/s41377-020-0264-5>
- [35] X. Ma, A. Zeng, J. Gao, Z. Hu, C. Xu, J.H. Son, S.Y. Jeong, et al., *Natl. Sci. Rev.* **8**, nwa305 (2021). <https://doi.org/10.1093/nsr/nwaa305>
- [36] Z. Hu, Z. Wang, Q. An, and F. Zhang, *Sci. Bull.* **65**, 131 (2020). <https://doi.org/10.1016/j.scib.2019.09.016>
- [37] J.I. Pankov, *Optical Processes in Semiconductors*, (Prentice-Hall, Englewood Cliffs, 1971).
- [38] V. Manikandan, P. Velmurugan, J.-H. Park, W.-S. Chang, Y.-J. Park, P. Jayanthi, M. Cho, and B.-T. Oh, “Green synthesis of silver oxide nanoparticles and its antibacterial activity against dental pathogens,” *3 Biotech*, **7**(1), 72 (2017). <https://doi.org/10.1007/s13205-017-0670-4>
- [39] A. Rita, A. Sivakumar, S.S.J. Dhas, and S.A. Martin Britto Dhas, “Structural, optical and magnetic properties of silver oxide (AgO) nanoparticles at shocked conditions”, *J. Nanostruct. Chem.* **10**, 309 (2020). <https://doi.org/10.1007/s40097-020-00351-z>

ПОКРАЩЕННЯ ГІБРИДНОГО ФОТОДЕТЕКТОРА TPD/AGO NPS ШЛЯХОМ ДОДАВАННЯ PEDOT PSS

Шахла Маджид Дж., Омар Аднан

Факультет фізики, Науковий коледж, Багдадський університет, Багдад, Ірак

Фотодетектор був виготовлений шляхом сплавлення наночастинок AgO з полімером алкіл-TPD (N'-дифенілбензидину) та нанесення суміші TPD:AgO на підкладки з полістиролу за допомогою технології спінування. Час відгуку синтезованого (PSi/TPD:AgO) детектора (за допомогою вольфрамової лампи з потужністю 250 Вт/см²) та його значення (0,35 с) вимірювали в секундах. Виявлення, специфічність і фотовідгук становили (6,23×10⁸ Вт, 1, 3,611×10⁸ Вт⁻¹Гц^{1/2}·см і 19,072×10⁻³ А/Вт). Вимірювання Холла показують, що наночастинки n-типу мають концентрацію носія приблизно (1,15×10¹⁷ см⁻³). З додаванням полімеру полі(3,4-етилендіокситіофен):полі(стиролсульфонат) (PEDOT:PSS) виявлення, специфічність, оптична відповідь і час реакції детектора були покращені до (80,06×10⁸ Вт⁻¹, 46,4×10⁸ Вт⁻¹Гц^{1/2}·см, 2019,48×10⁻³ А/Вт і 5,3 мс) відповідно.

Ключові слова: характеристики; посилення фотоструму; ефект Холла; питома чутливість; час відгуку

SYNTHESIS OF GRAPHENE VIA ARC DISCHARGE AND ITS CHARACTERIZATION: A COMPARATIVE APPROACH[†]

Michael O. Awoji^{a,*}, Audu D. Onoja^b, Mathias I. Echi^b

^aDepartment of Physics, Kwararafa University Wukari, Taraba State, Nigeria

^bDepartment of Physics, Federal University of Agriculture Makurdi, Benue State, Nigeria

*Corresponding Author e-mail: moawoji@kuw.edu.ng

Received February 4, 2023; revised February 21, 2023; accepted February 23, 2023

Herein, few layer graphene was synthesized using two arc discharge chambers of different volumes to ascertain the influence of chamber size on the quality and yield of graphene. In both arc discharge chambers (A and B), graphite rods were ignited at arc current of 200 A and pressure of 500 Torr to produce vaporized carbon atoms which were deposited on the chamber wall. The synthesized graphene was characterized using the combined effect of UV spectroscopy, X-ray diffraction, Raman spectroscopy, scanning electron microscopy and transmission electron microscopy. It was observed that, an increase in the chamber size led to an increase in the number of graphene layers (4 – 6 layers) and an increase in the crystalline size D (9.6 – 17.4 nm) as revealed by XRD results. Raman analysis shows lower value of I_D/I_G of 0.62 indicating the presence of lower defect in chamber A as compared to the I_D/I_G value of 0.93 observed in chamber B. A graphene yield of 0.96 g was obtained from chamber A while 0.67 g of the same product was obtained from chamber B. The fabricated arc discharge systems suggest that a larger chamber size could promote a better yield of graphene on an industrial scale. Hence, the research is relevant to the development of larger amounts of quality FLG for industrial device applications.

Keywords: Few-layer graphene; Arc discharge; Plasma; Chamber size; Spectroscopy

PACS: 68.65.Ac, 81.05.U-, 81.05.Uw, 81.05.ue, 81.05.uf, 81.07.Wx

INTRODUCTION

Graphene is the basic structural component of carbon allotropes counting charcoal, graphite, carbon nanotubes and fullerenes [1] and has attracted a considerable attention due to its unique electronic and optoelectronic properties [2]. In many respects, graphene is considered to be an alternative to silicon device applications owing to its exceptional band structure (relatively zero bandgap) characteristics, outlining its improved optical properties and electrical competences. Besides, graphene is becoming increasingly used in the manufacture of lightweight and strong body parts for vehicles [3]. However, reproducible and stable techniques to yield larger amount and high-quality crystallite graphene at an industrial scale to compete the already commercialized silicon-based devices hold out to be the most worrisome impediment to producing graphene. Graphene is currently being studied for several applications such as transparent electrodes, graphene field-effect transistors, paper-based ultra-capacitors, composites, sensors, and integration with modern tools in neuroscience [4].

Graphene was first discovered and recognized through mechanical exfoliation process [5]. Though the exfoliation practice yielded high quality of graphene for research drives, it is not a sustainable technique for the industrialization of graphene based devices [1]. Towards such goal, it is believed that chemical processes such as Chemical Vapor Deposition (CVD) is more suitable as reported by researchers [6, 7], other techniques for graphene synthesis include; plasma-enhanced chemical vapor deposition (PECVD) [8], micromechanical cleavage [9], reduction of graphene oxide [10], epitaxial growth on silicon carbide [11], and arc discharge method [12].

Among all these methods, the arc discharge technique seems to be relatively cheaper and easy to operate. The arc discharge method of graphene synthesis requires some process conditions such as; high temperature, the influx of vaporized carbon, buffer gas, and in some cases a catalyst could be used [13]. These process conditions are allowed to interact in a confined volume of an arc discharge chamber, resulting in the growth of nanomaterial. Several studies on these parameters have been carried out with much emphasis on the features of the synthesized products [7]. Li et al. [14] proved a technique in which petroleum asphalt is utilized as a precursor in a water arc discharge system. To date, many authors have studied the effect of gas pressure, gas temperature, arc current and thermal gradient of growth zone on the characteristic of graphene synthesized via the arc discharge approach [15, 16]. However, the influence of the arc discharge chamber size on the products obtained has been far less studied, mainly when considering experimental works.

In view of the success of the arc discharge method in the production of graphene, further study of this technique for large-scale synthesis of few layer graphene (FLG) on an industrial scale is a subject of concern [17]. Herein, we report on the effect of chamber size on the quality and yield of FLG produced via the arc discharge method. It was observed that by exploring larger chamber size, optimal temperature gradient could be achieved due to the larger surface area of the chamber as it cools gradually, resulting in better yield as compared to the smaller chamber [18]. Though graphene is known as an excellent electronic material, synthesizing single layer of it has been less explored. However, the majority of these methods of graphene synthesis categorized with low output and large-scale production are yet to be achieved [19].

[†] Cite as: M.O. Awoji, A.D. Onoja, and M.I. Echi, East Eur. J. Phys. 1, 252 (2023), <https://doi.org/10.26565/2312-4334-2023-1-34>

© M.O. Awoji, A.D. Onoja, M.I. Echi, 2023

This paper therefore, presents how increase in arc chamber size could facilitate graphene synthesis to an industrial scale. Hence, the arc discharge approach still remains one of the most viable techniques for synthesizing FLG in bulk amounts for industrial use.

EXPERIMENTAL PROCEDURE

The two-arc discharge systems A (450 mm×100 mm) and B (300 mm×60 mm) were set up as shown in Figure 1. The two electrodes in the arc discharge chamber were set up such that they are about 1 to 2 mm apart. The mechanical feed-through enables movement of the movable electrode controlled from outside the stainless chamber. The chamber was evacuated to a pressure of 10^{-2} Torr. Argon gas was then introduced into the chamber from the argon gas cylinder to a pressure of 500 Torr. Both electrodes were connected to a high current of 200 A using a high current source. The mechanical drive was used to create an initial contact and immediate separation of the electrodes to initiate the arc discharge leading to evaporation of the graphite electrodes. The inlet and outlet were used to circulate water through the wall of the chamber. Arc discharge of the electrodes leads to an influx of vaporizes carbon deposited on the chamber wall. The deposited carbon soot sample was carefully collected for analysis.

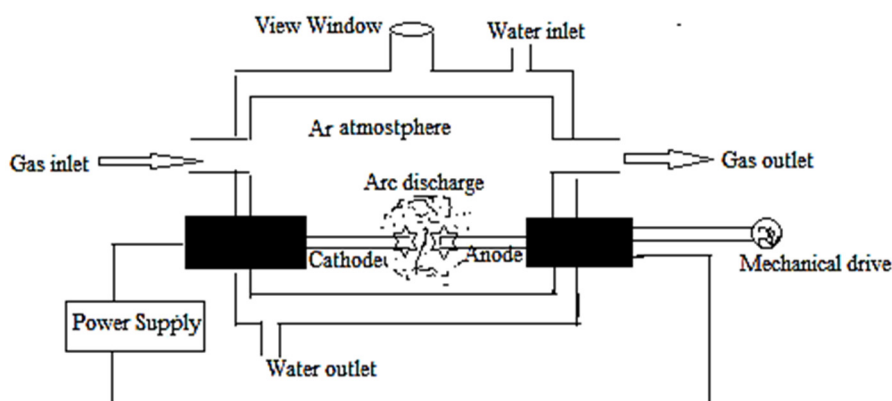


Figure 1. Schematic diagram of arc discharge system

To analyze the synthesized graphene nanoparticles, the following measuring instruments were used; UV-visible (UV-vis) spectroscope (Infinite F200 M; TECAN, Ltd., Männedorf, Switzerland), Rint Ultima X-ray diffraction (XRD) (Rigaku Co., Tokyo, Japan). Raman spectroscope (NRS-7100, JASCO, Tokyo, Japan), Scanning electron microscope (SEM) (JSM-6510LV, JEOL, Ltd, Japan) and Transmission electron microscope (TEM) (JEM-2100F, JEOL, Ltd., Tokyo, Japan).

RESULTS AND DISCUSSION

Figure 2 shows the UV-vis absorbance spectra of the synthesized graphene nanoparticles for Arc chambers A and B. Samples collected from arc chambers A and B respectively, revealed maximum absorption peaks at 251 nm and 258 nm with a continuous fall that stretches beyond 600 nm.

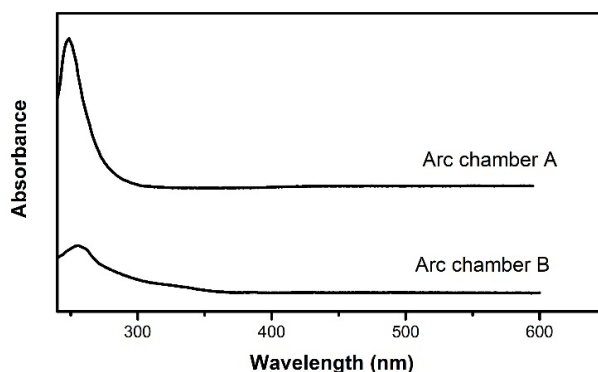


Figure 2. UV-vis spectra of graphene synthesized using chamber A and B

This characteristic is typical of graphene and is consistent with the optical property of graphene and other graphene nanoparticle composites [20]. It can be seen that the absorption peak of synthesized graphene in Arc chamber B shifted to a higher wavelength with a decrease in absorbance. This low absorbance is due to the increase in crystallite size (D) of the synthesized graphene using the smaller Arc chamber [2]. In the case with the Arc Chamber A, the larger chamber, a higher absorption (Gaussian) peak at the wavelength of $\lambda = 251$ nm was observed. The high absorption is due to the increased in Chamber size which causes a decreased in D , thus producing fewer layers of graphene as compared to

chamber B. Interestingly, graphene has another origin called graphene quantum dots (GQDs). Thus far, the high quality synthesized graphene nanoparticles in Arc Chamber A is of $D < 10$ nm, making it a good candidate for applications in GQDs and graphene-based photoelectric devices [2, 21]. Similarly, this graphene material will enhance electroluminescence due to its smaller D and high optical absorption in the UV region in agreement with previous works [2, 20]. Details of the number of layers and D of graphene synthesized using arc chamber A and B are presented in Table 1.

Table 1. Crystalline size (D), interlayer spacing (d) and number of layers of graphene synthesized using arc chamber A and B

Arc Chambers	FWHM (β)	2θ ($^\circ$)	D (nm)	d -spacing (\AA)	No of layers
A	0.8858	26.7	9.623	3.37206	4
B	0.4904	26.6	17.379	3.36081	6

Figure 3 shows XRD patterns of the samples synthesized with the different Arc discharge chamber sizes (A and B). The XRD spectra show an intense peak of (002) plane of diffraction at $2\theta = 26.7^\circ$ and 26.6° for arc chambers A and B respectively.

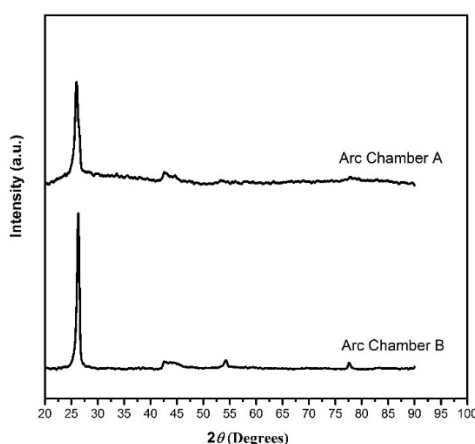


Figure 3. XRD patterns of graphene synthesized using chamber A and B

This signifies the characteristic of a well-ordered crystal structure of carbon materials [22]. The interlayer spacing (d) ~ 3.37 \AA and 3.36 \AA as obtained for arc chamber A and chamber B are slightly higher than that of graphite (3.34 \AA). The diffraction peak of pure graphite originates around 26.3° , matching to the highly ordered d of 0.34 nm sideways the (002) direction [23]. The significant difference in diffraction pattern at 2θ recorded by XRD in both Chambers could be ascribed to the loose nature of FLG [24]. The much defect in Arc Chamber B implies that decrease in chamber size increases D and d , hence much defects could be recorded whereas increase in chamber size produced FLG with less defect thereby yielding higher quality graphene. The D and d of the synthesized FLG were calculated using the Debye-Scherrer equation (1) [22]:

$$D = \frac{0.94\lambda}{B\cos\theta} \quad (1)$$

where λ is the X-ray wavelength in nanometer (nm), β is the peak width of the diffraction peak profile at half maximum height in radians, θ is the scattering angle in radians. It was observed that the peak intensity was higher for the smaller arc chamber, implying an increase in D . The number of layers of the FLG synthesized at various arc chamber sizes was calculated using the Scherrer equation (2) [25]:

$$N = \frac{D}{d} + 1 \quad (2)$$

where all symbols have their usual meaning. This clearly shows that graphene synthesized in a larger arc chamber is of fewer layers and more crystalline compared to that synthesized using a smaller arc chamber as shown in Table 1.

The Raman spectroscopy primarily provides evidence concerning the uniformity of graphene carbon skeleton [26]. Presented in Figure 4 is the Raman spectrograms of the synthesized graphene using arc chambers A and B. The spectroscopy revealed three major bands, the D band ~ 1348 /cm, band G ~ 1576 /cm and band 2D ~ 2690 /cm indicating the presence of graphene signature with the absence of graphite shoulder [13]. This result is similar to previous work of other researchers [8, 27]. The D band is related to the level of defects present in graphene [26]. D and 2D bands are both characteristics of sp^2 hybridized carbons. In pure form, graphene has well-ordered structure screening intense graphitic bands G at 1600 /cm which arise from the scattering of the E_{1g} phonon sp^2 hybridized carbon [28]. The intensity of D peak in Arc chamber B increases gradually together with the number of holes in the structure or sp^2 new centers created by covalent bonds activated by defects band 2D ~ 2690 /cm which informs about the value of cumulative load of defects

and number of layers of the synthesized graphene plane [23, 26]. In the incidence of <1% of the structural defects, the breakdown of the D band can be employed to confirm the quality of the synthesized graphene [26].

The number of defects of the graphene-based nanomaterial can be revealed by the ratio of intensity of D band and the G band (I_D/I_G), while the I_{2D}/I_G ratio could be used to distinguish the number of synthesized graphene layers of the FLG. Therefore, when the ratio I_D/I_G is greater than 1, it depicts the protuberant defective state of the synthesized graphene nanomaterial [20, 29]. Comparatively, as presented in Table 2, the increase in I_D/I_G and I_{2D}/I_G in Arc Chamber B are caused by increased number of defects on the surface of graphene [8, 20, 27, 29].

Thus from Table 2, the I_D/I_G ratio is in values of 0.62 and 0.93 corresponding to the Arc chamber A and B respectively. Since Arc chamber B produces the highest value of 0.93 of I_D/I_G ratio, indicating that there are more defects in the smaller chamber B unlike the fabricated Arc chamber A with the larger volume. However, in both chambers the quality of graphene nanoparticles produced are high since both have I_D/I_G values that are relatively less than 1 [20, 29]. Nevertheless, it has been reported that the number of synthesized graphene layers could increase from 3 – 7 when the I_{2D}/I_G is ~ 0.5 . Previous report also estimated a FWHM of 68 cm^{-1} and I_{2D}/I_G of ~ 0.6 for 3 – 5 layers [30]. These values are closely related to the ones obtained in Table 2. This is also in agreement with the number of layers obtained from the XRD result presented in Table 1.

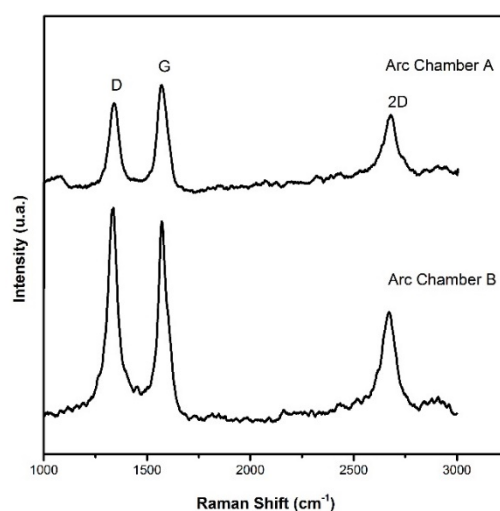


Figure 4. Raman spectrograms of graphene synthesized using chamber A and B

Table 2. Intensity ratios and full width at half maximum (FWHM) of graphene synthesized using arc chamber A and B

Arc Chamber	I_D/I_G	I_{2D}/I_G	FWHM(2D)
A	0.62	0.68	78.46
B	0.93	0.76	77.408

The SEM images provided the surface morphology of the synthesized graphene nanoparticles as shown in Figure 5a and b. The SEM images of the synthesized FLG in both Arc chambers are similar, revealing the presence of a large number of FLG flakes in agreement with previous studies [25]. Nucleation of graphene domain with an average size of $5\ \mu\text{m}$ was observed in the SEM micrograph.

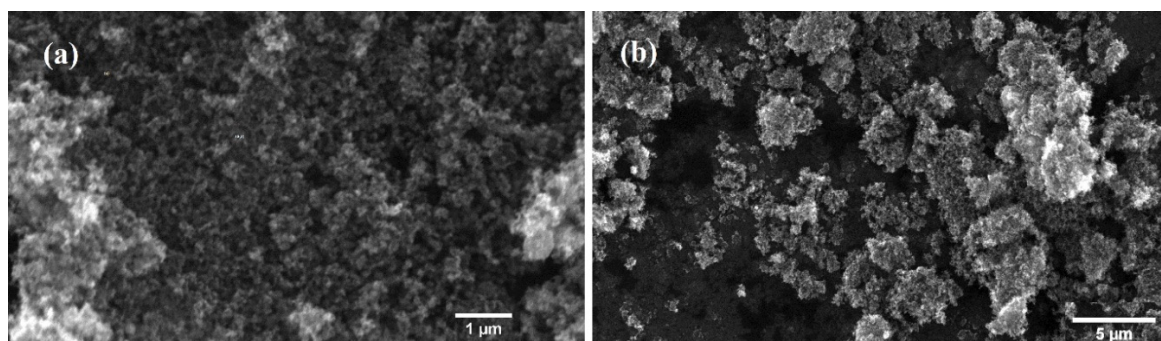


Figure 5. SEM micrographs of synthesized graphene via (a) Arc chamber A and (b) Arc chamber B

The structure of the synthesized graphene in Arc discharge chambers A and B was examined by the TEM images as shown in Figure 6a and b. The micrographs show a large area of FLG graphene sheet with a size of 100 – 200 nm. It was observed that the surfaces of the FLG sheets in both chambers displayed are quite uniformly distributed and with

wrinkles [22]. This is due to the defects caused by each chamber during synthesis and the variation in the number of graphene layers for each chamber as shown in Table 1. However, the graphene obtained from chamber A, in Figure 6a, reveals high level of transparency than the synthesized graphene in chamber B (see Figure 6b). The variation in transparency could be ascribed to changes in the lattice parameters and the number of layers of graphene in both arc discharge chamber [30].

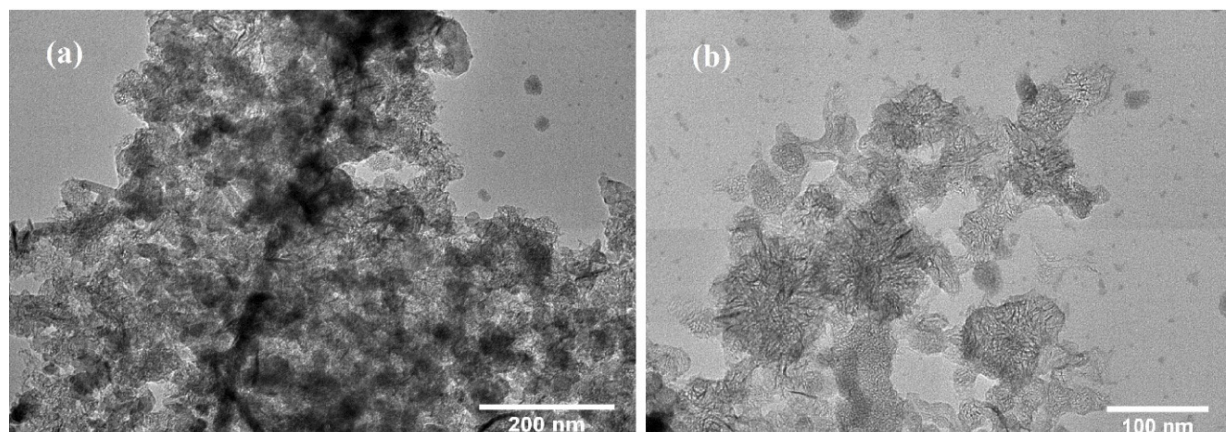


Figure 6. TEM micrographs of synthesized graphene via (a) Arc chamber A and (b) Arc chamber B

CONCLUSION

The research work here presented has comparatively investigated the amount and the quality of graphene synthesized in two arc discharge chambers of different sizes (volume). The graphene was synthesized from the graphite electrodes via arc discharge chamber technique. The fabricated larger arc discharge chamber of dimension 450 mm×100 mm hereafter tag Arc chamber A gave a better amount of graphene yield of 0.96 g when compared to the 0.67 g yield obtained from an arc discharge chamber B of smaller dimension 300 mm×60 mm diameter. The UV spectroscopy result revealed that the absorption peak of synthesized graphene in Arc chamber B shifted to a higher wavelength with a decrease in absorbance. The UV-vis spectrum of both chambers shows Gaussian absorption peaks around the wavelength of 251 – 258 nm. From the XRD results, the synthesized graphene samples on average, showed a $2\theta = 26.65^\circ$ peak with (002) orientation that is characteristic of graphene. The synthesized graphene sample in Arc chamber A is of 4 layers with thickness of 9.62 nm compared to the synthesized nanoparticles in Arc chamber B having 6-layer graphene flake of greater thickness. These results are supported with the layer numbers obtained from the Raman spectroscopy results. The ratio ID/IG confirmed the FLG with the UV-vis spectrum revealing the graphene signature. The average size of flakes observed in the SEM micrographs was 5 μm . The TEM micrographs show graphene nanostructure with thickness variation. Our results show the viability of large-scale production of quality graphene using the arc discharge approach, which may open up more opportunities in the wide range of applications of FLG, comprising anti-corrosion coatings, composites, super-capacitors, energy storage, and transparent conductive films.

ORCID IDs

Michael O. Awoji, <https://orcid.org/0000-0003-1467-2484>; Audu D. Onoja, <https://orcid.org/0000-0003-2024-876X>
Mathias I. Echi, <https://orcid.org/0000-0002-0908-5878>

REFERENCES

- [1] V.B. Mbayachi, E. Ndayiragije, T. Sammani, S. Taj, E. R. Mbuta, and A. U. Khan, "Graphene synthesis, characterization and its applications: A review", *Results Chem.* **3**, 100163 (2021). <https://doi.org/10.1016/j.rechem.2021.100163>
- [2] T. M. Magne, T. O. Vieira, L. M. R. Alencar, F. M. Junior, S.G. Piperni, S. V. Carneiro, L. M. U. D. Fechine, R. M. Freire, K. Golokhvast, P. Metrangolo, P. B. A. Fechine, and R. S. Oliveira, "Graphene and its derivatives: understanding the main chemical and medicinal chemistry roles for biomedical applications", *J. Nanostructure Chem.* **12**, 693 (2022). <https://doi.org/10.1007/s40097-021-00444-3>
- [3] J. Jayaseelan, A. Pazhani, A. X. Michael, J. Paulchamy, A. Batako, and P. K. H. Guruswamy, "Characterization Studies on graphene-aluminium nano composites for aerospace launch vehicle external fuel tank structural application", *Materials*, **15**, 5907 (2022). <https://doi.org/10.3390/ma15175907>
- [4] H. Tan, D. Wang, and Y. Guo, "A strategy to synthesize multilayer graphene in arc-discharge plasma in a semi-opened environment", *Materials*, **12**, 2279 (2019). <https://doi.org/10.3390/ma12142279>
- [5] F. Zhang, K. Yang, G. Liu, Y. Chen, M. Wang, S. Li, and R. Li, "Recent advances on graphene: Synthesis, properties and applications", *Compos. Part A Appl. Sci.* **160**, 107051 (2022). <https://doi.org/10.1016/j.compositesa.2022.107051>
- [6] M. Sierra, R. Thomann, I. Krossing, R. Hanselmann, R. Mülhaupt, and Y. Thomann, "Laser ablation on isostatic graphite: A new way to create exfoliated graphite", *Materials*, **16**, 5474 (2022). <https://doi.org/10.3390/ma15165474>
- [7] D. Vernardou, "Advances in chemical vapor deposition", *Materials*, **13**, 4167 (2020). <https://doi.org/10.3390/ma13184167>
- [8] M. Chen, Y. Hugo, and Y. Kehan, "Plasma-enhanced chemical vapor deposition of graphene optimized by pressure". *Mater. Res. Express*, **6**, (10) 105605 (2019). <https://doi.org/10.1088/2053-1591/ab38d7>

- [9] R. C. Sinclair, J. L. Suter, and P. V. Coveney, "Micromechanical exfoliation of graphene on the atomistic scale", *Phys. Chem.* **21**, 5716 (2019). <https://doi.org/10.1039/c8cp07796g>
- [10] K. Kanishka, H. De Silva, H. Huang, and M. Yoshimura, "Progress of reduction of graphene oxide by ascorbic acid", *Appl. Surf. Sci.* **447**, 3380 (2018). <https://doi.org/10.1016/j.apsusc.2018.03.243>
- [11] S. Ramazanov, "Recent advances in graphene epitaxial growth: aspects of substrate surface modification using coatings", *Coatings*, **12**, 1828 (2022). <https://doi.org/10.3390/coatings12121828>
- [12] I. Levchenko, K. Ostrikov, J. Zheng, X. Li, M. Keidar, and K. B. K. Teo, "Scalable graphene production: perspectives and challenges of plasma applications", *Nanoscale*, **8**, 10511 (2016). <https://doi.org/10.1039/C5NR06537B>
- [13] Y. Wu, X. Liu, and Z. Shi, "Large-scale synthesis of high-quality graphene sheets by improved alternating current arc-discharge method" *RSC Adv.* **6**, 93119 (2016). <https://doi.org/10.1039/C6RA22273K>
- [14] Y. Li, Q. Chen, K. Xu, T. Kaneko, and R. Hatakeyama, "Synthesis of graphene nanosheets from petroleum asphalt by pulsed arc discharge in water", *Chem. Eng. J.* **216**, 45 (2013). <https://doi.org/10.1016/j.cej.2012.09.123>
- [15] B. Qin, T. Zhang, H. Chen, Y. Ma, "The growth mechanism of few-layer graphene in the arc discharge process", *Carbon*, **102** 494 (2016). <https://doi.org/10.1016/j.carbon.2016.02.074>
- [16] R. Kumar, R. K. Singh, P. K. Dubey, P. Kumar, R. S. Tiwari, and I. Oh, "Pressure-dependent synthesis of high-quality few-layer graphene by plasma-enhanced arc discharge and their thermal stability", *J Nanopart Res.* **15**, 1847 (2013). <https://doi.org/10.1007/s11051-013-1847-3>
- [17] K. A. Madurani, S. Suprpto, N. I. Machrita, and S. L. Bahar, "Progress in graphene synthesis and its application: History, challenge and the future outlook for research and industry", *ECS J. Solid State Sci. Technol.* **9**, 093013 (2020). <https://doi.org/10.1149/2162-8777/abbb6f>
- [18] K. E. Kitko, and Q. Zhang, "Graphene-based nanomaterials: From production to integration with modern tools in neuroscience", *Front. Syst. Neurosci.* **26**, 1 (2019). <https://doi.org/10.3389/fnsys.2019.00026>
- [19] I. Levchenko, U. Cvelbar, and M. Keidar, "Graphene flakes in arc plasma : Conditions for the fast single-layer growth", *Graphene*, **5**, 81 (2016). <https://doi.org/10.4236/graphene.2016.52009>
- [20] A. Mondal, and N. R. Jana, "Graphene nanoparticle composites and their applications in energy, environmental and biomedical science", *Rev. Nanosci. Nanotechnol.* **3**, 177 (2014). <https://doi.org/10.1166/rmn.2014.1051>
- [21] B. Liu, W. Yu, Z. Yan, P. Cai, F. Gao, C. Tang, P. Gu, and Z. Liu, "The light absorption enhancement in graphene monolayer resulting from the diffraction coupling of surface plasmon polariton resonance", *J. Chen: Nanomaterials*, **12**, 216 (2022). <https://doi.org/10.3390/nano12020216>
- [22] J. Amaro-gahete, A. Ben, and D. Esquivel, "A comparative study of particle Size distribution of graphene nanosheets synthesized by an ultrasound-assisted method", *Nanomaterials*, **9**, 152 (2019). <https://doi.org/10.3390/nano9020152>
- [23] D. V Smovzh, I. A. Kostogrud, S. Z. Sakhapov, A. V Zaikovskii, and S. A. Novopashin, "The synthesis of few-layered graphene by the arc discharge sputtering of a Si-C electrode", *Carbon N. Y.* **112**, 97 (2017). <https://doi.org/10.1016/j.carbon.2016.10.094>
- [24] A. Jiříčková, O. Jankovský, Z. Sofer, and D. Sedmíubský, "Synthesis and applications of graphene oxide", *Materials*, **15**, 920 (2022). <https://doi.org/10.3390/ma15030920>
- [25] G. Borand, N. Akçamlı, and D. Uzunsoy, "Structural characterization of graphene nanostructures produced via arc discharge method", *Ceram. Int.* **47**, 8044 (2020). <https://doi.org/10.1016/J.CERAMINT.2020.11.158>
- [26] A. C. Ferrari, J. C. Meyer, V. Scardaci, C. Casiraghi, M. Lazzeri, F. Mauri, S. Piscanec, D. Jiang, K. S. Novoselov, S. Roth, and A. K. Geim, "Raman spectrum of graphene and graphene layers", *Phys. Rev. Lett.* **97**, 187401 (2006). <https://doi.org/10.1103/PhysRevLett.97.187401>
- [27] A. Gupta, G. Chen, P. Joshi, S. Tadigadapa, P. C. Eklund, "Raman scattering from high-frequency phonons in supported n-graphene layer films", *Nano Lett.* **6**, 2667 (2006). <https://doi.org/10.1021/nl061420a>
- [28] A. Merlen, J. G. Buijnsters, and C. Pardanaud, "A guide to and review of the use of multiwavelength raman spectroscopy for characterizing defective aromatic carbon Solids: from graphene to amorphous carbons", *Coatings*, **7**, 153 (2017). <https://doi.org/10.3390/COATINGS7100153>
- [29] V. Kumar, A. Kumar, D. J. Lee, and S. S. Park, "Estimation of number of graphene layers using different methods: A focused review", *Materials (Basel)*, **14**, 4590 (2021). <https://doi.org/10.3390/ma14164590>
- [30] Y. Çelik, E. Flahaut, and E. Suvacı, "A comparative study on few-layer graphene production by exfoliation of different starting materials in a low boiling point solvent", *FlatChem.* **1**, 74 (2017). <https://doi.org/10.1016/j.flatc.2016.12.002>

СИНТЕЗ ГРАФЕНУ ДУГОВИМ РОЗРЯДОМ ТА ЙОГО ХАРАКТЕРИСТИКА: ПОРІВНЯЛЬНИЙ ПІДХІД

Міхаел О. Аводжі^a, Ауду Д. Оноджа^b, Матіас І. Ечі^b

^aФакультет фізики, Університет Кварарафа Вукарі, штат Тараба, Нігерія

^bФакультет фізики, Федеральний університет сільського господарства Макурді, штат Бенуе, Нігерія

Синтезовано кілька шарів графену з використанням двох дугових розрядних камер різного об'єму, щоб з'ясувати вплив розміру камери на якість і вихід графену. В обох камерах дугового розряду (А і В) графітові стрижні запалювали при струмі дуги 200 А і тиску 500 торр, щоб отримати випаровані атоми вуглецю, які осідали на стінці камери. Синтезований графен був охарактеризований за допомогою комбінованого ефекту УФ-спектроскопії, дифракції рентгенівських променів, спектроскопії раманівського розсіювання, скануючої електронної спектроскопії та електронної спектроскопії на просвічування. Було помічено, що збільшення розміру камери призвело до збільшення кількості графенових шарів (4-6 шарів) і збільшення кристалічного розміру D (9,6-17,4 нм), як показали результати XRD. Раманівський аналіз показує нижче значення ID/IG 0,62, що вказує на наявність меншого дефекту в камері А порівняно зі значенням ID/IG 0,93, що спостерігається в камері В. Вихід графену 0,96 г було отримано з камери А, тоді як 0,67 г той самий продукт було отримано з камери В. Виготовлені системи дугового розряду припускають, що більший розмір камери може сприяти кращому виходу графену в промислових масштабах. Отже, дослідження актуальне для розробки більшої кількості якісного FLG для застосування в промислових пристроях.

Ключові слова: кількшаровий графен; дуговий розряд; плазма; розмір камери; спектроскопія

INSTRUCTIONS FOR PREPARING MANUSCRIPT IN THE EAST EUROPEAN JOURNAL OF PHYSICS

Name A. Author^{a*}, Name B. Co-Author(s)^{b†}

^aAffiliation of first author

^bAffiliation of second author (if different from the first Author)

*Corresponding Author: corresponding_authors@mail.com, ^aORCID ID

[†]E-mail: co_authors@mail.com, ^bORCID ID

Received May 25, 2022; revised June 25, 2022 accepted July 5, 2022

Each paper must begin with an abstract. The abstract should be typed in the same manner as the body text (see below). Please note that these Instructions are typed just like the manuscripts should be. The abstract must have at least **250-300 words**, supplying general information about the achievements, and objectives of the paper, experimental technique, methods applied, significant results and conclusions. Page layout: the text should be printed on the paper A4 format, at least **5 pages**, with margins of: **Top - 3, Bottom, Left and Right - 2 cm**. The abstract, keywords should be presented in **English** (only for foreign authors), and **Ukrainian**. The text should be prepared in “**doc**” or “**docx**” format.

Keywords: there, must, be, 5-10 keywords

PACS: specify PACS code(s) here

Instructions

The text should be typed as follows:

- **title:** Times New Roman, 11 pt, ALL CAPS, bold, 1 spacing, centred;
- **authors:** name, initials and family names; Times New Roman, 11 pt, bold, 1 spacing, centred;
- **affiliation(s):** Times New Roman, 9 pt, italic, 1 spacing, centred;
- **abstract:** Times New Roman, 9 pt, 1 spacing, justified;
- **body text:** Times New Roman, 10 pt, 1 spacing, justified; paragraphs in sections should be indented right (tabulated) for 0.75 cm;
- **section titles:** Times New Roman, 10 pt, bold, 1 spacing, centred, without numbering, one line should be left, blank above section title;
- **subsection titles:** Times New Roman, 10 pt, bold, 1 spacing, centred, without numbering in accordance to the section (see below), one line should be left blank above subsection title;
- **figure captions:** width of the figure should be 85 or 170 mm, Figures should be numbered (**Figure 1.**) and titled below Figures using sentence format, Times New Roman, 9 pt, 1 spacing, centred (if one line) or justified (if more than one line); one line should be left blank below figure captions;
- **table captions:** width of the table should be 85 or 170 mm, Tables should be numbered (**Table 1.**) and titled above tables using sentence format, Times New Roman, 10 pt, 1 spacing, left, Tables should be formatted with a single-line box around the outside border and single ruling lines between rows and columns; one line should be left blank below tables;
- **equations:** place equations centred, numbered in Arabic: (1), flush right, equations should be specially prepared in **MathType** or “**Microsoft Equation**”, Times New Roman, 10 pt.

Additional Instructions

Numerated figures and tables should be embedded in your text and placed after they are cited. Only sharp photographs and drawings are acceptable. Letters in the figures should be 3 mm high. The figures should be presented in one of the following graphic formats: jpg, gif, pex, bmp, tif.

References

List of References must contain **at least 30% of articles published over the past 5 years** and **no more than 30% of links to their own work**. Cite References by number in AIP style (<https://aip.scitation.org/php/authors/manuscript>). Numbering in the order of referring in the text, e.g. [1], [2-5], etc. References should be listed in numerical order of citation in the text at the end of the paper (justified), Times New Roman, 9 pt, 1 spacing.

Journal Articles

- [1] T. Mikolajick, C. Dehm, W. Hartner, I. Kasko, M.J. Kastner, N. Nagel, M. Moert, and C. Mazure, *Microelectron. Reliab.* **41**, 947 (2001), [https://doi.org/10.1016/S0026-2714\(01\)00049-X](https://doi.org/10.1016/S0026-2714(01)00049-X).
- [2] S. Bushkova, B.K. Ostafiychuk, and O.V. Copenaev, *Physics and Chemistry of Solid State.* **15**(1), 182 (2014), <http://page.if.ua/uploads/pcss/vol15/1501-27.pdf>. (in Ukrainian)
- [3] M. Yoshimura, E. Nakai, K. Tomioka, and T. Fukui, *Appl. Phys. Lett.* **103**, 243111 (2013), <http://dx.doi.org/10.7567/APEX.6.052301>

E-print Resources with Collaboration Research or Preprint

- [4] M. Aaboud et al. (ATLAS Collaboration), *Eur. Phys. J. C*, **77**, 531 (2017), <http://dx.doi.org/10.1140/epjc/s10052-017-5061-9>
- [5] Sjöstrand et al., *Comput. Phys. Commun.* **191**, 159 (2015), <https://doi.org/10.1016/j.cpc.2015.01.024>
- [6] Boudreau, C. Escobar, J. Mueller, K. Sapp, and J. Su, (2013), <http://arxiv.org/abs/1304.5639>

Books

- [7] S. Inoue, and K.R. Spring, *Video Microscopy: The fundamentals*, 2nd ed. (Plenum, New York, 1997), pp. 19-24.
- [8] I. Gonsky, T.P. Maksymchuk, and M.I. Kalinsky, *Біохімія Людини [Biochemistry of Man]*, (Ukrmedknyga, Ternopil, 2002), pp. 16. (in Ukrainian)

Edited Books

- [9] Z.C. Feng, editor, *Handbook of Zinc Oxide and Related Materials: Devices and Nano Engineering*, vol. 2, (CRC Press/Taylor & Francis, Boca Raton, FL, 2012)

Book Chapters

- [10] P. Blaha, K. Schwarz, G.K.H. Madsen, D. Kvasnicka, and J. Luitz, in: *WIEN2K, An Augmented Plane Wave Plus Local Orbitals Program for Calculating Crystal Properties*, edited by K. Schwarz (Techn. Universität Wien, Austria, 2001).
- [11] M. Gonzalez-Leal, P. Krecmer, J. Prokop, and S.R. Elliot, in: *Photo-Induced Metastability in Amorphous Semiconductors*, edited by A.V. Kolobov (Wiley-VCH, Weinheim, 2003), pp. 338-340.
- [12] A. Kochelap, and S.I. Pekar, in: *Теорія Спонтанної і Стимульованої Хемілюмінесценції Газів [Theory of Spontaneous and Stimulated Gas Chemiluminescence]* (Naukova dumka, Kyiv, 1986), pp. 16-29. (in Russian)

Conference or Symposium Proceedings

- [13] C. Yaakov, and R. Huque, in: *Second International Telecommunications Energy Symposium Proceedings*, edited by E. Yow (IEEE, New York, 1996), pp. 17-27.
- [14] V. Nikolsky, A.K. Sandler, and M.S. Stetsenko, in: *Автоматика-2004: Матеріали 11 Міжнародної Конференції по Автоматичному Управлінню [Automation-2004: Materials of the 11th International Conference on Automated Management]* (NUHT, Kyiv, 2004), pp. 46-48. (in Ukrainian)

Patent

- [15] I.M. Vikulin, V.I. Irha, and M.I. Panfilov, Patent Ukraine No. 26020 (27 August 2007). (in Ukrainian)

Thesis / Dissertation

- [16] R.E. Teodorescu, Ph.D. dissertation, The George Washington University, 2009.

Special Notes

1. Use International System of Units (SI system). 2. It is undesirable to use acronyms in the titles. Please define the acronym on its first use in the paper. 3. Refer to isotopes as ¹⁴C, ³H, ⁶⁰Co, etc.

Наукове видання

СХІДНО-ЄВРОПЕЙСЬКИЙ ФІЗИЧНИЙ ЖУРНАЛ

Номер 1, 2023

EAST EUROPEAN JOURNAL OF PHYSICS

No 1, 2023

Збірник наукових праць
англійською та українською мовами

Коректор – Коваленко Т.О.
Технічний редактор – Гірник С.А.
Комп'ютерне верстання – Гірник С.А.

Підписано до друку 27.02.2023. Формат 60×84/8. Папір офсетний.

Друк цифровий.

Ум. друк. арк. 27. Обл.-вид. арк. 33,8
Тираж 50 пр. Зам. 1/2023. Ціна договірна

Видавець і виготовлювач
Харківський національний університет імені В.Н. Каразіна
61022, Харків, майдан Свободи, 4
Свідоцтво суб'єкта видавничої справи ДК № 3367 від 13.01.09

Видавництво Харківський національний університет імені В.Н. Каразіна
тел. +380-057-705-24-32